Theses and Dissertations | 1. Thesis and Dissertation Collection, all items

2012-12

Development, integration, and testing of a nano-satellite coupling mechanism using shape memory alloy for an interference joint

Perez, Alberto Oscar

Monterey, California. Naval Postgraduate School

http://hdl.handle.net/10945/27887

NAVAL POSTGRADUATE SCHOOL

MONTEREY, CALIFORNIA

THESIS

DEVELOPMENT, INTEGRATION, AND TESTING OF A NANO-SATELLITE COUPLING MECHANISM USING SHAPE MEMORY ALLOY FOR AN INTERFERENCE JOINT

by

Alberto Oscar Perez

December 2012

Thesis Co-Advisors: Marcello Romano
James Hansen Newman

Approved for public release; distribution is unlimited

THIS PAGE INTENTIONALLY LEFT BLANK

REPORT DOCUMENTATION PAGE		*Form Approved OMB No. 0704–0188*

1. AGENCY USE ONLY *(Leave blank)*	2. REPORT DATE December 2012	3. REPORT TYPE AND DATES COVERED Master's Thesis

4. TITLE AND SUBTITLE
DEVELOPMENT, INTEGRATION, AND TESTING OF A NANO-SATELLITE COUPLING MECHANISM USING SHAPE MEMORY ALLOY FOR AN INTERFERENCE JOINT

5. FUNDING NUMBERS

6. AUTHOR(S) Alberto Oscar Perez

7. PERFORMING ORGANIZATION NAME(S) AND ADDRESS(ES)
Naval Postgraduate School
Monterey, CA 93943–5000

8. PERFORMING ORGANIZATION REPORT NUMBER

9. SPONSORING /MONITORING AGENCY NAME(S) AND ADDRESS(ES)
N/A

10. SPONSORING/MONITORING AGENCY REPORT NUMBER

11. SUPPLEMENTARY NOTES The views expressed in this thesis are those of the author and do not reflect the official policy or position of the Department of Defense or the U.S. Government. IRB Protocol number ____N/A____.

12a. DISTRIBUTION / AVAILABILITY STATEMENT
Approved for public release; distribution is unlimited

12b. DISTRIBUTION CODE

13. ABSTRACT (maximum 200 words)

This thesis contains the results of a complete redesign effort, including development, integration, and experimental testing of a very small mechanical coupling mechanism. This mechanism is suitable for nano-satellites and uses a shape memory alloy (SMA) ring, press-fit into a metallic bushing to create a releasable interference joint. A detailed explanation of the techniques used to press-fit the SMA ring into the metallic bushing is included along with a description of why the SMA ring shrinks to its austenite phase upon heat activation and how it decouples from the metallic bushing. The coupling—engineered to be as small as one tenth of a cubic centimeter—is capable of achieving holding strengths in excess of 135 N (30 lbf).

SMA characteristics and current release mechanisms are explained and tests are conducted to validate the holding strength achieved by the interference joint between the SMA and the metallic bushing. The design and part selection for each component of the Engineering Design Unit (EDU) is documented and launch conditions simulated to test the EDU's performance, releasability, and to validate the static holding force. Finally, this thesis describes the simulated integration of the EDU into a 3U CubeSat structure.

14. SUBJECT TERMS Shape Memory Alloy, SMA, Nickel Titanium, NiTi, Nichrome wire, press-fit, interference joint, austenite, twinned martensite, detwinned martensite, CubeSat, non-explosive actuation, AL 7075-T6, polycarbonate.

15. NUMBER OF PAGES
146

16. PRICE CODE

17. SECURITY CLASSIFICATION OF REPORT Unclassified	18. SECURITY CLASSIFICATION OF THIS PAGE Unclassified	19. SECURITY CLASSIFICATION OF ABSTRACT Unclassified	20. LIMITATION OF ABSTRACT UU

Standard Form 298 (Rev. 2–89)
Prescribed by ANSI Std. 239–18

i

THIS PAGE INTENTIONALLY LEFT BLANK

DEVELOPMENT, INTEGRATION, AND TESTING OF A NANO-SATELLITE COUPLING MECHANISM USING SHAPE MEMORY ALLOY FOR AN INTERFERENCE JOINT

Alberto Oscar Perez
Lieutenant Commander, United States Navy
B.S., University of Florida, 2001

Submitted in partial fulfillment of the
requirements for the degree of

MASTER OF SCIENCE IN ASTRONAUTICAL ENGINEERING

from the

NAVAL POSTGRADUATE SCHOOL
December 2012

Author: Alberto Oscar Perez

Approved by: Dr. Marcello Romano
                     Thesis Co-Advisor

                     Dr. James H. Newman
                     Thesis Co-Advisor

                     Dr. Knox T. Millsaps
                     Chair, Department of Mechanical and Aerospace
                     Engineering

THIS PAGE INTENTIONALLY LEFT BLANK

ABSTRACT

This thesis contains the results of a complete redesign effort, including development, integration, and experimental testing of a very small mechanical coupling mechanism. This mechanism is suitable for nano-satellites and uses a shape memory alloy (SMA) ring, press-fit into a metallic bushing to create a releasable interference joint. A detailed explanation of the techniques used to press-fit the SMA ring into the metallic bushing is included along with a description of why the SMA ring shrinks to its austenite phase upon heat activation and how it decouples from the metallic bushing. The coupling—engineered to be as small as one tenth of a cubic centimeter—is capable of achieving holding strengths in excess of 135 N (30 lbf).

SMA characteristics and current release mechanisms are explained and tests are conducted to validate the holding strength achieved by the interference joint between the SMA and the metallic bushing. The design and part selection for each component of the Engineering Design Unit (EDU) is documented and launch conditions simulated to test the EDU's performance, releasability, and to validate the static holding force. Finally, this thesis describes the simulated integration of the EDU into a 3U CubeSat structure.

THIS PAGE INTENTIONALLY LEFT BLANK

TABLE OF CONTENTS

LIST OF FIGURES

LIST OF TABLES

THIS PAGE INTENTIONALLY LEFT BLANK

LIST OF ACRONYMS AND ABBREVIATIONS

AL	Aluminum
AL 7075-T6	Aluminum 7075 with T6 Tempered
CTE	Coefficient of Thermal Expansion
CubeSat	Cube Satellite
EDU	Engineering Design Unit
MPE	Max Predicted Environment
NiTi	Nickel Titanium
NPS	Naval Postgraduate School
NPSCuL	Naval Postgraduate School CubeSat Launcher
PC	Polycarbonate
SMAs	Shape Memory Alloys
SMA^{2}C	Single Motion Actuated Shape Memory Alloy Coupling "SMACK"
TINYSCOPE	Tactical Imaging Nano-satellite Yielding Small-Cost Operations and Persistent Earth-coverage

.

THIS PAGE INTENTIONALLY LEFT BLANK

ACKNOWLEDGMENTS

The author would like to recognize:

Dr. Marcello Romano, Department of Mechanical and Aerospace Engineering and
Dr. James Newman, Space Systems Academic Group, Naval Postgraduate School

> Your support and education in this thesis is greatly treasured. Your total willingness to guide me through the engineering process enhanced this thesis and my learning experience at the Naval Postgraduate School. You allowed me to use hands-on tactics in the continual development of a release mechanism for CubeSats, a goal of mine since coming to NPS.

Mr. Levi Owen and Mr. John Mobley, NPS Machine Shop

> Your contribution, skill, and willingness to work with me in designing and manufacturing all my testing hardware and engineering design unit was greatly appreciated. The level of commitment and workmanship directly correlates to the success of this thesis.

Dr. Chanman Park, Department of Mechanical and Aerospace Engineering

> Your knowledge and expertise in the tensile strength machine, and your support with setting up and testing of all my samples' holding force capability made this thesis simpler.

Dr. Luke N. Brewer, Department of Mechanical and Aerospace Engineering

> Your initial consultation in selecting different bushing materials led to achieving this thesis' goal of reducing size and power requirements, while maintaining overall effectiveness.

Mr. Daniel Sakoda of the Small Satellite Laboratory, Mr. Vidur Kaushish, and Mrs. Wenschel Lan, My graduate Student Colleagues

> Your commitment to educating me about the vibration testing process and your contribution to vibration analysis were invaluable to this thesis.

LCDR Peter Firenze, My Colleague

> For your support during the design of the engineering design unit. For keeping me motivated to produce a quality product within the short time span of this thesis.

My wife, Morgan, and sons, Oscar, Milo, and Eli

> Your support and dedication to my education and work while at the Naval Postgraduate School directly impacted my success. Without you and the boys this tour would not have had the positive impact that it did. You taught me perseverance in my work and the importance of family time. I love you all.

I. INTRODUCTION

A. PURPOSE

This thesis documents the work done to redesign and retest the shape-memory-alloy release mechanism previously designed by the Spacecraft Robotics Lab (SRL) at the Naval Postgraduate School (NPS). Current options for release mechanisms for very small satellites, called CubeSats, are limited, allowing opportunities for new concepts to be developed. The mechanism must be strong enough to withstand any static and vibrational loads, preventing unintentional release due to the vigorous launch environment. The mechanism must be small enough to integrate in the CubeSat's 1000 cm^3 form factor. The amount of power required for activation must be low and compatible with both the limited electrical bus system and available power from the onboard batteries. The mechanism must be free from any explosive actuation to reduce shock and debris during deployment. Lastly, the mechanism should involve a minimum number of mechanical parts to reduce any failure modes, therefore increasing reliability.

B. BACKGROUND

1. Shape Memory Alloy

Metals and alloys play a vital role in all forms of engineering. Their uses range from structural support to mechanical devices. Most metals share common characteristics such as responses to temperature, strain, stress, and deformations. Most metals expand when heated and contract when cooled. Depending on the direction of stress (force) applied, they may expand or contract. Strain is the term used to measure the percentage of change in either contraction (negative strain) or expansion (positive strain). However, there are certain alloys that do not share these characteristics.

Shape Memory Alloy (SMA) refers to a type of metallic alloy that does not share the normal characteristics of typical metals. SMAs fall into different

1

subclasses. Three basic classes of SMA include Iron, Copper, and Nickel. The Iron-based alloys ($FeNi_{31}Co_{10}Ti_3$ and FeMnSi) have a thermal operating temperature of about 150°C (the temperature in which the SMA is in the austenite phase). Both the Copper-based alloys, such as Copper Zinc (CuZn) and Copper Aluminum (CuAl) SMAs, and the Nickel-based alloys, such as Nickel-Titanium (NiTi) SMAs, have varying operating temperatures. These operating temperature differences are the result of varying the composition of each element during manufacturing of the SMAs. For example, varying the composition of aluminum between 5 wt.% (weight percent) and 10wt.% in CuAl can shift the operating temperatures from -180°C to 100°C.

The Nickel Titanium (NiTi) based alloys are well studied and are the alloys most commonly used. Their popularity in commercial applications is due to the alloy's one-way and two-way shape memory effects. As with the copper-based alloys, increasing or decreasing the amount of a certain element affects the operating temperature range as well as the alloy's capacity for resisting corrosion. One such corrosion resistant NiTi alloy is the 55at% (atomic percentage) of Nickel. Table 1 lists different NiTi compositions and their hysteresis characterizations. Explanations of M_f, M_s, A_s, and A_f are detailed in the section below.

NiTi Based SMAs	M_f	M_s	A_s	A_f
$Ti_{50}Ni_{50}$	15	55	80	89
$Ti_{49.5}Ni_{50.5}$	−78	−19	9	53
$Ti_{49}Ni_{51}$	−153	−114	−89	−40
$Ti_{49}Ni_{51}Cu_{10}$	8	30	35	50
$Ti_{50}Ni_{40}Cu_{10}$	21	41	53	67
$Ti_{44}Ni_{47}Nb_9$	−175	−90	−85	−35
$Ti_{42.2}Ni_{49.8}Hf_8$	50	69	111	142
$Ti_{40.7}Ni_{49.8}Hf_{9.5}$	61	90	118	159
$Ti_{40.2}Ni_{49.8}Hf_{10}$	103	128	182	198
$Ti_{35.2}Ni_{49.8}Hf_{15}$	95	136	140	210
$Ti_{30.2}Ni_{49.8}Hf_{20}$	127	174	200	276
$Ti_{48}Ni_{47}Zr_5$	20	65	75	138
$Ti_{43}Ni_{47}Zr_{10}$	45	100	113	165
$Ti_{38}Ni_{47}Zr_{15}$	100	175	175	230
$Ti_{33}Ni_{47}Zr_{20}$	205	275	265	330
$Ti_{50}Pd_{50}$	550	563	580	591
$Ti_{50}Ni_{20}Pd_{30}$	208	241	230	241
$Ti_{50}Ni_{10}Pd_{40}$	387	403	419	427
$Ti_{50}Ni_5Pd_{45}$	467	486	503	509
$Ti_{50}Ni_{45}Pt_5$	10	29	36	49
$Ti_{50}Ni_{40}Pt_{10}$	−8	18	−27	36
$Ti_{50}Ni_{30}Pt_{20}$	241	300	263	300
$Ti_{50}Ni_{20}Pt_{30}$	537	619	626	702

Table 1.   NiTi Hysteresis. From [1]

Various industries are making use of the mechanical work produced by the SMA cycles. The aerospace industry uses SMAs for actuators and wire tendons. The development of a variable geometric airfoil using SMA allows the airfoil to change its shape from symmetric to cambered. The medical field uses SMA for stents, filters, orthodontic wires, and for minimally invasive surgery. The oil industry uses SMA for actuation capabilities in release devises in down hole drilling equipment. This is just a small sample of the manifold ways that SMA technology is being applied.

a.   SMA Phases

SMAs can "remember" a shape even after severe deformations. When SMAs undergo some type of strain due to an external stress at low temperatures, they assume a deformed state. The SMAs remain in the deformed state and only return to their original state once heat is applied. These phases are called austenite (original state) and martensite (deformed state).

3

During production of a SMA, the material is formed at high temperatures in its austenite phase. In this phase, the crystal structure of the material is uniformly cubic. The twinned martensite phase is caused by a reduction in temperature. The internal crystal lattice structure changes from cubic to tetragonal, orthorhombic, or monoclinic. Although the internal structure is transformed, little to no external changes—such as strain—occur. The other extreme phase is the detwinned (deformed) martensite phase in which the material undergoes a crystal lattice transformation and an external material property change. The external property change can be a change of length for a wire, change in diameter for a cylinder or a ring, or any other measurable strain of the material. The ability to move between the austenite and detwinned martensite phases allows the SMA to be useful in its mechanical form. Complete SMA cycle can be seen in Figure 1.
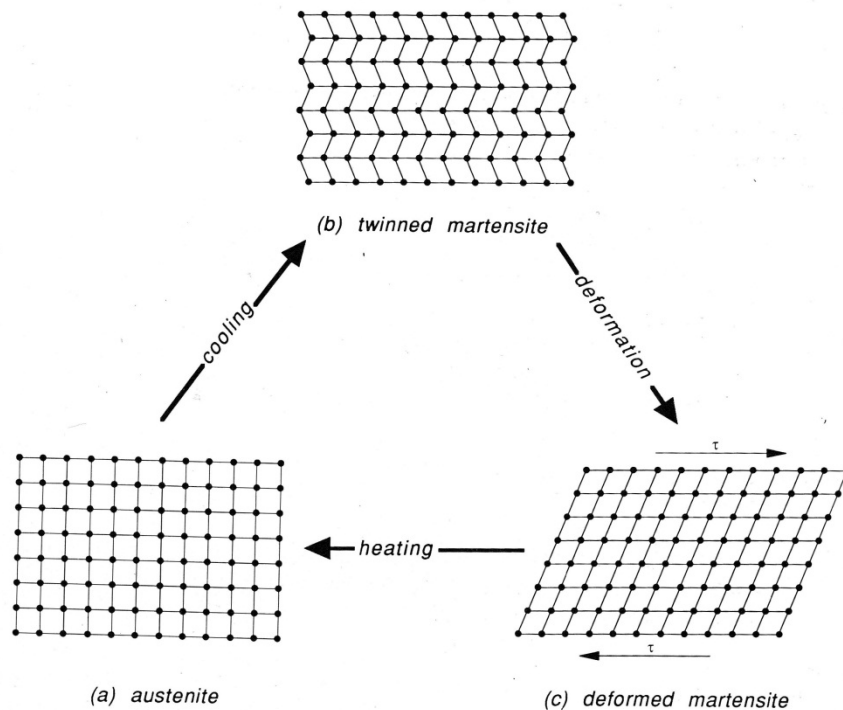
Figure 1.   SMA Phases. From [2]

b. SMA Complete Work Cycle

(1) Step One-Temperature Effects. SMAs undergo four transitional phases during their mechanical work cycle. Beginning with the austenite phase, there is the martensitic start temperature (M_s), the martensitic finish temperature (M_f), the austenitic start temperature (A_s), and the austenitic finish temperature (A_f). These are the transitional phase temperatures referenced in Table 1. As mentioned above, each SMA has different transitional temperatures depending on its composition, but each one follows the same process. The changes in the internal crystal lattice structure between the austenite and twinned martensite phases can be seen in Figure 2. Starting at the austenite phase, the internal crystal lattice of the material remains constant during cooling until it reaches the M_s temperature at which the structure begins to change. Final twinned martensitic phase is complete once the SMA is cooled to its M_f temperature. If the SMA is brought to the M_f temperature and full twinned martensite phase is achieved, heating the SMA up will result in a similar reverse step. SMAs' internal twinned martensite crystal lattice structure remain intact until heated to the A_s temperature. Changes in the internal structure continue to unfold until the A_f temperature is reached.
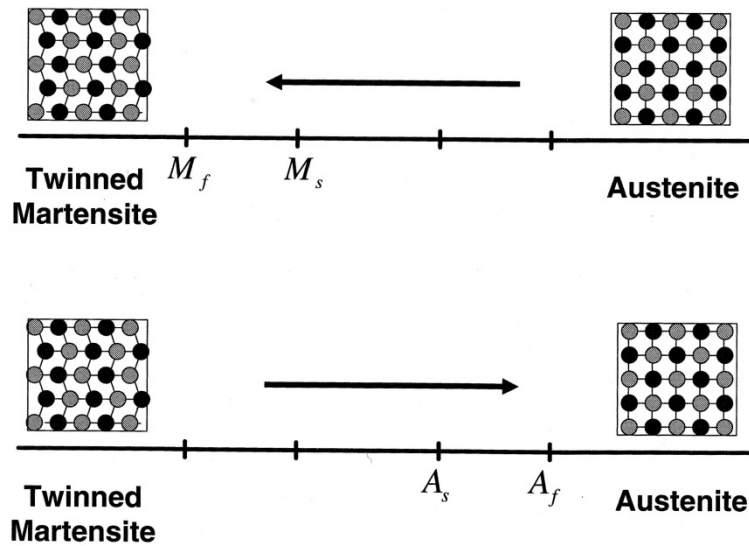
Figure 2.   SMA Temperature Change Effect. From [1]

This transition between austenite and twinned martensite results in internal crystal lattice changes only. No external changes have occurred; therefore, no mechanical work may be affected. To have any mechanical work provided by the SMA, the SMA must undergo a change in its external property such as strain.

(2)   Step Two-Strain. Beginning at the twinned martensite phase, applying stress at a constant temperature to the SMA causes a strain (volume or length change) as well as an internal structure change. These changes result in the detwinned martensite phase. At the detwinned martensite phase, the SMA will hold its shape even after the removal of the stress that caused it to transform. Temperature remains constant in this phase. The crystal lattice transformation between the twinned martensite to detwinned martensite phase can be seen in Figure 3.
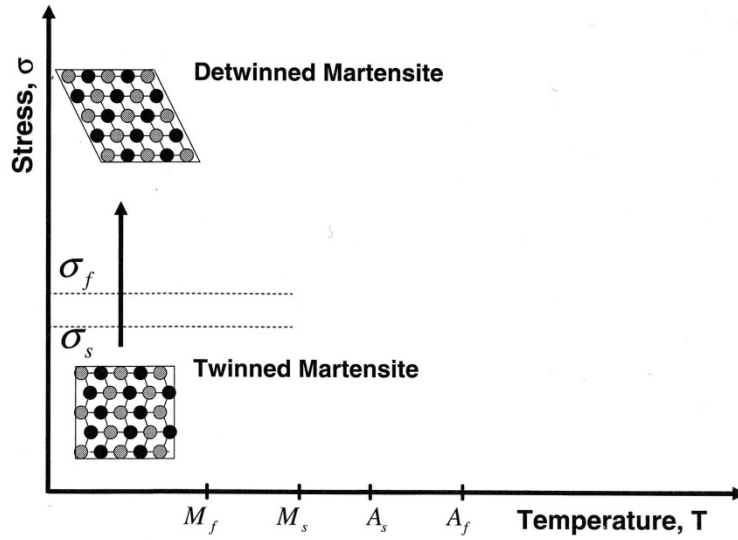
Figure 3.   SMA Stress Effect. From [1]

(3)   Step Three-Return to Original. To get back to the austenite phase, heat must be applied. The reverse process is different from the original process of transition between the austenite and detwinned martensite phases. As the SMA is heated above the A_s temperature, the internal structure shifts towards the austenite phase. Final austenite structure is achieved when the A_f temperature is reached. In this third step, the addition or removal of stress is not a factor in the SMA's path to its original austenite phase; it is only a factor of temperature. The SMA's crystal lattice structure return to the austenite phase can be seen in Figure 4.
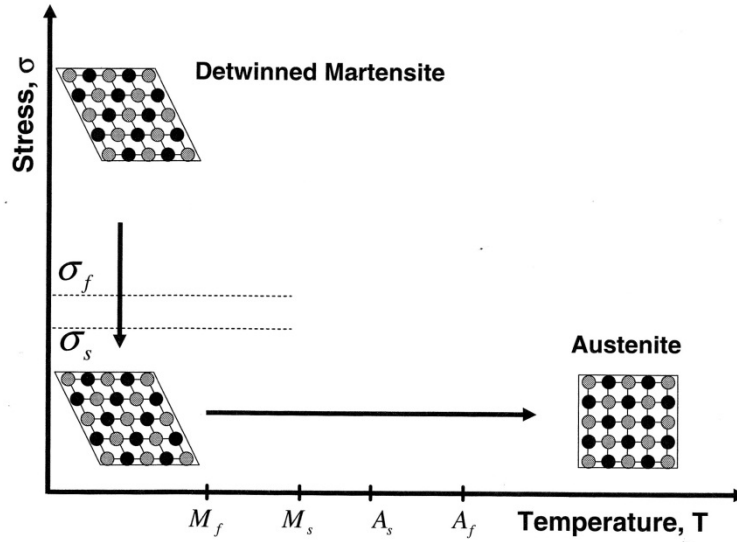
Figure 4.   SMA Unloading. From [1]

(4)   Overview. SMAs are manufactured in the austenite phase, but are usually delivered to the customer in the detwinned martensite phase. Because varying temperature alone changes the internal structure of the SMA without affecting its external shape, mechanical work cannot be done by the product in the austenite phase. However, when it is delivered at the detwinned martensite phase, the addition of heat causes a macroscopic shape change, allowing effective mechanical work to be done.

Figure 5 is an overview of a SMA cycle beginning at point A (austenite). Cooling the SMA brings it to point B (twinned martensite). Adding stress at constant temperature brings the SMA to point C (detwinned martensite). Lastly, heating the SMA brings it back to point A (austenite).
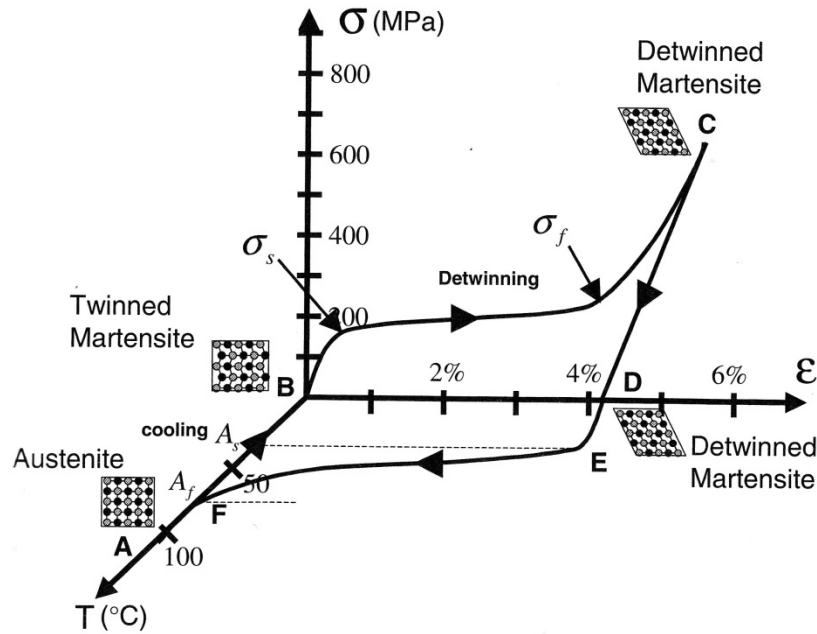
Figure 5.   SMA Complete Cycle. From [1]

(5)   Example of Work. SMAs are used for tube and pipe coupling. The coupling is machined in its austenite phase. It is then cooled and stretched to reach the detwinned martensite phase. The coupling now has the ability to perform work. To join two separate tubes or pipes, the coupling is placed between them and heated to its A_f temperature. This causes the coupling to shrink back to its original size while clamping on the two ends of the pipe. The SMA stages from machined to clamping on a tube can be seen in Figure 6.
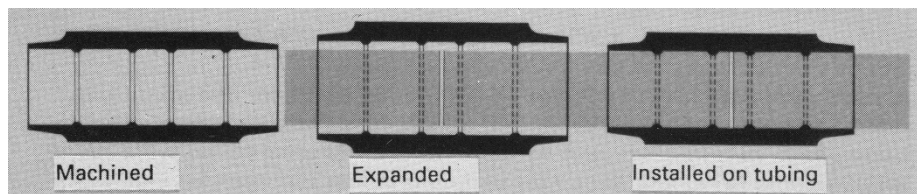
Figure 6.   SMA Tube Clamping. From [2]

In this example, the M_f of the SMA clamp is very cold (stored in liquid nitrogen), and the A_f is room temperature.

2. Press-Fitting and Equations

a. *Overview*

Press-fit fastening, also known as friction-fit and interference-fit, is a form of bringing two metals pieces, usually a shaft and hub, together. Industry uses press-fitting techniques when mechanical or adhesive bonding is not an option. Such examples include interconnects, bearing construction, automotive joints, and transmission gearing. Once fastened, frictional forces created by the circumferential hoop stresses translate to radial normal forces. The radial force, along with the materials' coefficient of friction, produces the axial and torsional holding strength. The pressure between the two parts is dependent on the materials' moduli of elasticity, Poisson's ratio, and amount of interference.

Interference is the measurement between the outer diameter of a shaft and the inner diameter of a hub (Figure 7). Increasing the interference typically increases the holding force, but too much of an interference can lead to hub fracture. This failure reduces the overall holding force. One way of maximizing the holding force involves reaching 80% of the hub's material yield stress [3].
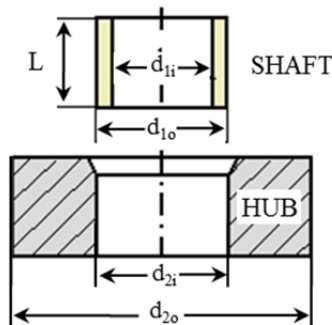
Figure 7.   Interference. From [4]

Using σ=radial stress, P=contact pressure / interference fit pressure, and c=inner hub diameter (d) divided by outer hub diameter (D) we get Equation 1.1

$$\sigma = \frac{P\sqrt{3+c^4}}{1-c^2} \, lb/in^2 \qquad\qquad (1.1)$$

Studies show that coupling hubs at c values below 0.4 operate well even if the full yield stress value is reached by the maximum combined stress at coupling (Figure 8)[3]..
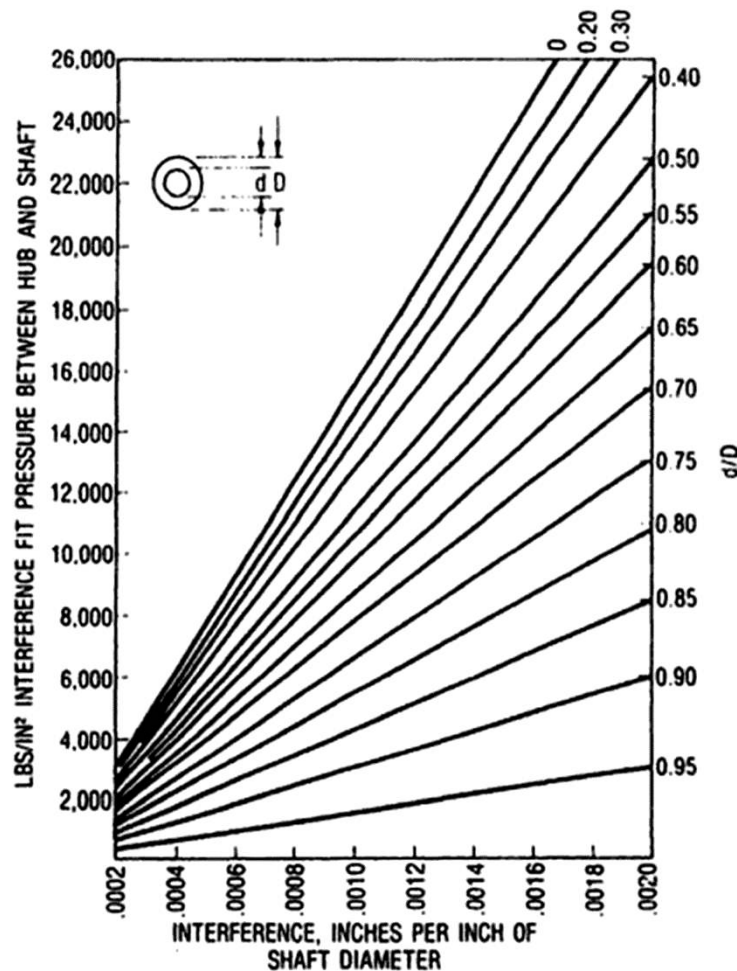
Figure 8.   Interference Fit Pressure For Varying C Values. From [3]

b.   *Method of Press-Fitting*

Press-fitting is achieved by one of two methods: force or applied heat. Forcing the shaft into the hub at constant temperature is possible for

11

interferences of about one mil (one-thousandth of an inch) or so for typical metals. Any interference above one mil requires thermal treatment.

To press-fit using heat, the hub is warmed to expand the inner diameter. The cooler shaft is then placed inside the heated hub. With the shaft in place, the hub is cooled and contracts against the shaft, creating a higher interference compared to simply using force. Using heat to expand the hub takes advantage of each material's coefficient of thermal expansion.

Calculations for press-fit follow below [5]

p = Contact pressure or Interference Pressure

$$p = \frac{\Delta}{\frac{d_{1o}}{E_2}\left(\frac{d_{2o}^2 + d_{1o}^2}{d_{2o}^2 - d_{1o}^2} + \upsilon_2\right) + \frac{d_{2i}}{E_1}\left(\frac{d_{2i}^2 + d_{1i}^2}{d_{2i}^2 - d_{1i}^2} - \upsilon_1\right)}$$ (1.2)

δ_{1o}= Change of the outer radius of the inner member (shaft)

$$\delta_{1o} = -\frac{pd_{2i}}{2E_1}\left(\frac{d_{2i}^2 + d_{1i}^2}{d_{2i}^2 - d_{1i}^2} - \upsilon_1\right)$$ (1.3)

δ_{2i} = Change of the inner radius of the outer member (hub)

$$\delta_{2i} = \frac{pd_{1o}}{2E_2}\left(\frac{d_{2o}^2 + d_{1o}^2}{d_{2o}^2 - d_{1o}^2} + \upsilon_2\right)$$ (1.4)

σ_1 = Radial stress at the contact surface of the inner member (shaft)

$$\sigma_1 = -\frac{pd_{2i}^2}{d_{2i}^2 - d_{1i}^2}\left(1 - \frac{d_{1i}^2}{d_{2i}^2}\right)$$ (1.5)

σ_2 = Radial stress at the contact surface of the outer member (hub)

$$\sigma_2 = \frac{pd_{1o}^2}{d_{2o}^2 - d_{1o}^2}\left(1 - \frac{d_{2o}^2}{d_{1o}^2}\right)$$ (1.6)

T = Torque that the pressed interference joint will resist

$$T = \frac{\pi d^2}{4}\mu pL$$ (1.7)

F_n= Normal force (relative to the press-fit surface)

$$F_n = p\pi dL$$ (1.8)

F_μ= Frictional axial "holding" force of the interference joint

$$F_\mu = \mu F_n \qquad\qquad (1.9)$$

E_1 = Elastic Modulus for the inner member (shaft)
E_2 = Elastic Modulus for the outer member (hub)
υ_1 = Poisson's Ratio for the inner member (shaft)
υ_2 = Poisson's Ratio for the outer member (hub)
μ = Coefficient of static friction at members interface
L = Contact length
d_{1o} = Outer diameter of the outer member (hub)
d_{1i} = Inner diameter of the outer member (hub)
d_{2o} = Outer diameter of the inner member (shaft)
d_{2i} = Inner diameter of the inner member (shaft)
    Note: $r_i = 0$ for a solid member
d = Nominal interference diameter = $(d_{i,outer} - d_{o,inner})/2$
Δ = Calculated interference = $d_{i,outer} - d_{o,inner}$

3.   Additional SMA Characteristics

NiTi material properties are dependent on the phase as seen in Figure 9. Examples of such properties are:

1)   SMA is more ductile in the martensite phase. The required stress to produce the same amount of strain in the martensite phase is lower than in the austenite phase.

2)   Poisson ratio for NiTi varies from 0.33 for martensite to 0.30 for austenite. The larger Poisson ratio is preferred for a higher contact pressure using Equation 1.2.

3)   Elasticity is dependent on phase. Martensite phase elasticity is less than that of the austenite phase.

4)   SMA has a 6% strain heat to recover [6]. The 6% strain tolerance is used in the design of the SMA coupling device as the upper bound limit.
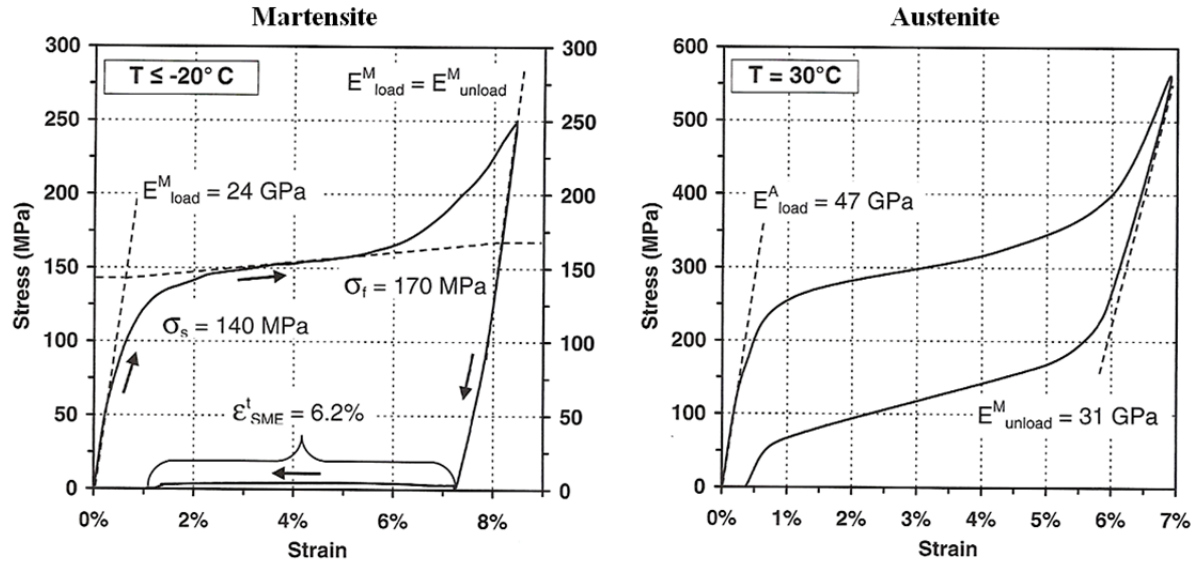
Figure 9.   Monotonic Loading of a NiTi SMA at Constant Temperatures. From [4]

Due to the pseudo-elastic[1] nature of the SMA, the results of Equations 1.2–1.9 can only be estimates. Not only are the Poisson ratio and modulus of elasticity different for each phase, but the coefficient of friction also changes. Research conducted at the University of California Los Angeles found that the coefficient of friction changed with adjustments in applied pressure. The coefficient of friction increased as the load increased [7]. In non-pseudo-elastic materials, the coefficient of friction is constant and frictional force is directly related to the applied normal force as in Equation 1.9

C.   COMPARE DEVELOPED DEVICES

Coupling devices for nano satellites are not as abundant as for larger spacecraft. As with all space rated applications, each component in a nano satellite must withstand the rigorous environments of space and space launch. Minimizing mass, power demand, and size is key, particularly for nano satellites

---

[1] Pseudoelasticity, sometimes called superelasticity, is an elastic (reversible) response to an applied stress, caused by a phase transformation between the austenitic and martensitic phases of a crystal.

and CubeSats. Below are examples of existing and experimental coupling devises.

1. Nichrome Burn Wire

The Naval Research Laboratory, with help from Co-op students, built a Nichrome burn wire release mechanism. In this model, a Vectran cable tie is used to secure the deployable structure. The mechanism utilizes a compressed spring in the stowed configuration to maintain contact between the Nichrome burn wire and the Vectran tie down cable. When electrical current passes through the Nichrome burn wire, it burns through the tie down cable; freeing the deployable structure. As seen in Figure 10, the stowed configuration has an intact tie down cable and a broken tie down cable in the deployed configuration.
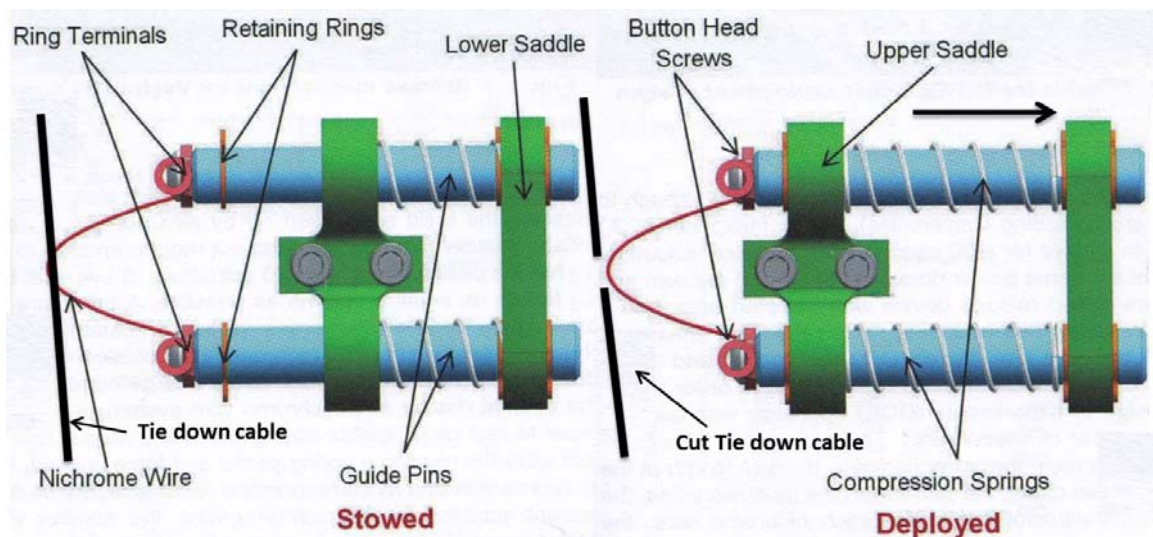
Figure 10.   Nichrome Burn Wire Release Mechanism in the Stowed and Deployed Configuration. After [8]

Figure 11 depicts a dual release setup used to provide dual redundancies for deployment. Overall dimensions for each mechanism are 32 mm (1.25 in)

long by 16.5 mm (0.65 in) wide by 11.5 mm (0.45 in) tall. 1.6 amps for 5.3 seconds are used to cut the cable tie using a 30 gauge Nichrome wire and a 200 denier Vectran cable

200 denier Vectran cable
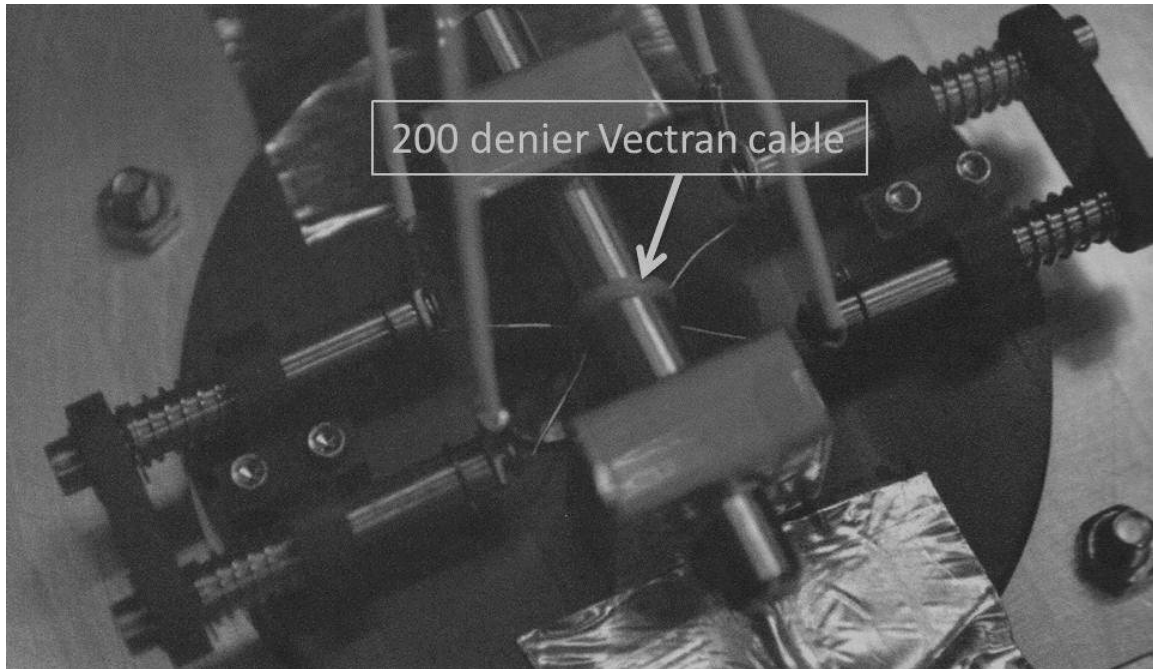
Figure 11.   Dual Release Mechanism with Single Tie Down Cable. From [8]

2.   TiNi Aerospace Model P5 Pin Puller

TiNi Aerospace produces six standard pin pullers (Figure 12). The P5 is the smallest of them with a diameter of 0.95 in and a length of 1.2 in. The pin in the extended position is under preload from a compressed spring. An SMA is used to release the latch, which initiates the retraction of the pin. The SMA is Joule heated (current passing directly to the SMA to heat it) making the pin puller a rapidly deploying mechanism [9].

Pinpuller P5

The P5 uses TiNi's patented trigger mechanism to retract the engagement Pin with 5 lbs of force and 0.250 in of stroke. It can be operated with as little as 0.5 amps of current.

Features:

- Redundant firing circuit
- Auto Shut Off Switch
- Simple manual reset*
- Space Qualified
- Fast Actuation (see below)

* Reset Tool Provided by TiNi Aerospace, Inc

1.25
(Length)

.950ø
(Nominal Body Diameter)
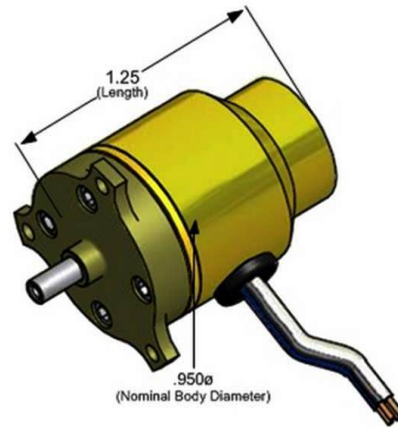
*Contact TiNi for detailed specification.

Function Time at Various Temperatures*

- −65°C
- 23°C
- 70°C
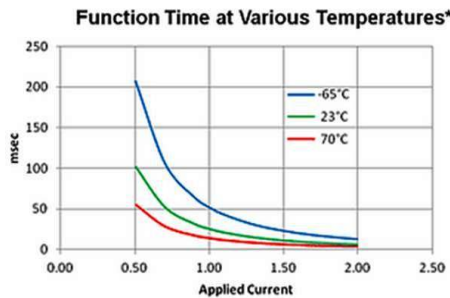
*Nominal values for reference only.

Mass:	1.06 oz. (30 g)
Power:	1.9 W @ 0.5 A
Operational Current:	0.5 to 2.0 A
Resistance:	7.7 ± 0.5 Ω @ 23°C
Pull Force:	5 lb-f [22.2 N] MIN
Pull Stroke:	0.250 in [6.3 mm] MAX
Axial Load (Actuation):	2 lb-f MAX
Side Load (Actuation):	10 lb-f MAX
Side Load (Non-Actuation):	50 lb-f MAX
Function Time:	35 ± 10 msec. @ 1.25 A @ 23°C
Reusable:	By Manual Reset
Life:	100 Cycles MIN
Operational :	−65° C to +70° C

*Specification subject to revision; Please contact TiNi Aerospace for detailed drawing (ICD). Note: Actuator resistance can be readily increased such that the actuator becomes operable from higher bus voltages.

Figure 12.   TiNi Pin Puller Model P5. From [10]

3.   SQUIGGLE Motor

The SQUIGGLE consists of a piezoelectric motor and a lead screw. The A nut is attached to the SQUIGGLE motor's lead screw. For nano satellite application, the SQUIGGLE motor's lead screw would attach to the deployable structure via a nut. Ultrasonic vibrations are actuated when current passes through the piezoelectric motor. These vibrations cause the lead screw to rotate, releasing the nut. Detailed specifications with drawings of the SQ-100 SQUIGGLE motor are shown in Figure 13.

17

SQ-100, SQ-100NM, and SQ-100V Series SQUIGGLE Motor

SQ-100 Series Motor	
Housing Diameter	12.3 mm max.
- Mounting Diameter	9.5 mm
Housing Length	36.6 mm
Shaft Diameter/Thread	3/16" x 100 threads/in (4.76 mm x 0.25 mm lead)
Shaft Length	See Ordering Information
Stall Force	5 N
Resolution (typical)	20 nm (without encoder)
Start/Stop Time	0.2 ms
Speed Range	0.001 to 2 mm/s
Range of Motion	See Ordering Information
Off-Power Hold	Yes (self-locking threads)
Operating Temperature	-20 to 40 °C

Motor Ordering Information

Model	Travel/Shaft length[1]
SQ-115-C1	15 mm / 63 mm
SQ-115V-C1[2]	15 mm / 63 mm
SQ-150-C1	50 mm / 103 mm

[1] Custom shaft length and range of motion on request.

[2] Vacuum motor operates to 10^{-7} Torr. Vacuum feed-throughs not included. Requirements: 3 wires, 30 gauge or greater, 200 V RMS.

Figure 13.   New scale Technologies Squiggle SQ-100. From [11]

D.   PREVIOUS ENGINEERING DESIGN UNIT

The Spacecraft Robotics Lab at the Naval Postgraduate School supports experimentation with, and creation of, new release mechanisms. CDR Will Crane, a 2010 graduate of the Naval Postgraduate School, developed a release mechanism using SMAs. The release mechanism is a non-explosive, single motion actuated mechanism small enough to be incorporated into a nano-satellite (dimensions listed in Figure 14). It uses an interference joint between a case-hardened-steel-bushing and a NiTi SMA ring. When heat is applied to the bushing, the NiTi ring and retaining bolt release from the bushing, allowing the attached structure to deploy. This section further reviews the Shape Memory

Alloy Single Motion Actuated Coupling (SMA^{2}C) device and the work done by Crane [4].

1. Design Unit

The concept of using a press-fitted SMA as a coupling device for nano satellites was previously researched by Will Crane.

- Micro-coupling integrated into Al 7075 housing
- Housing dimensions: 1.1" by 0.7" by 0.5"
- Connected to 10.0 V bus & draws 0.79 Amps
- Coupling capacity: +500 lbf
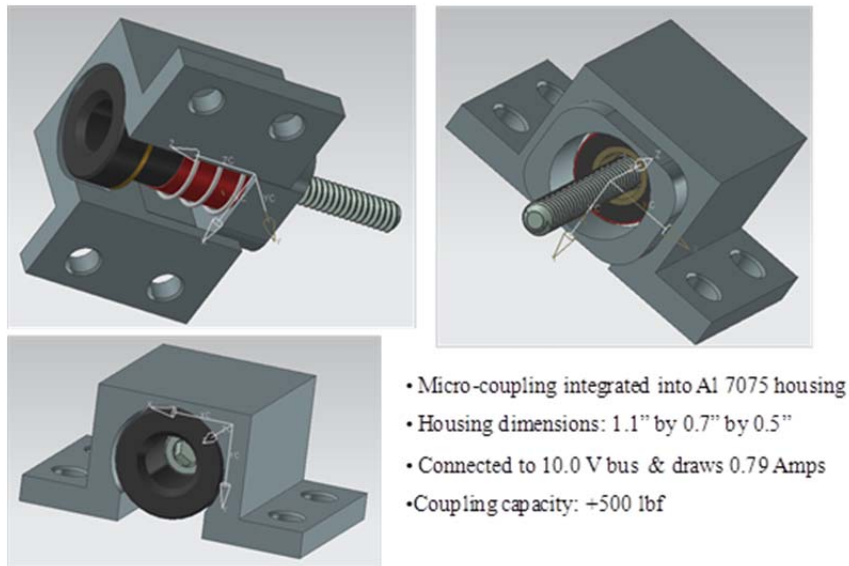
Figure 14.   Assembled View of SMA^{2}C Device. From [4]

The individual components of this Engineering Design Unit (EDU) are pictured in Figure 15 and Figure 16. A case-hardened-steel-bushing and NiTi SMA are used as the press-fit unit. A Kapton foil heater is wrapped around the case-hardened-steel-bushing as the heating element. The polyethermide isolation washer prevents heat from passing to the rest of the spacecraft during actuation. An aluminum push plate with a spring rests on the deployable structure, which is used to aid deployment. The retaining bolt's head rests on the SMA ring through storage and deployment. The other end of the retaining bolt is fastened to the deployable structure. The SMA is in an expanded detwinned martensite phase (see also Figure 6).
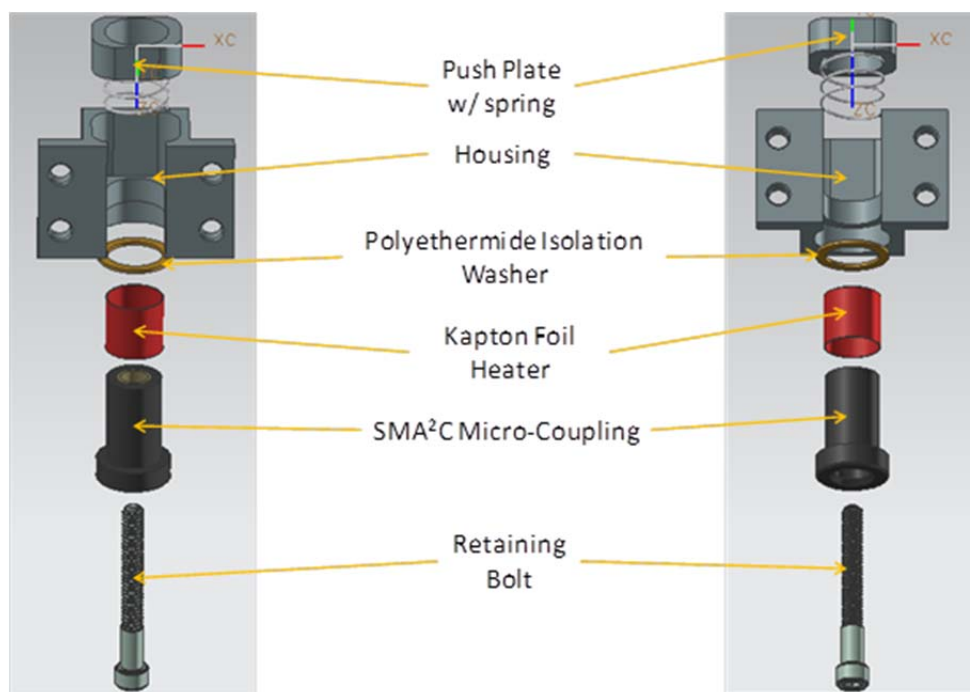
Figure 15.   Component View of SMA²C Device. From [4]
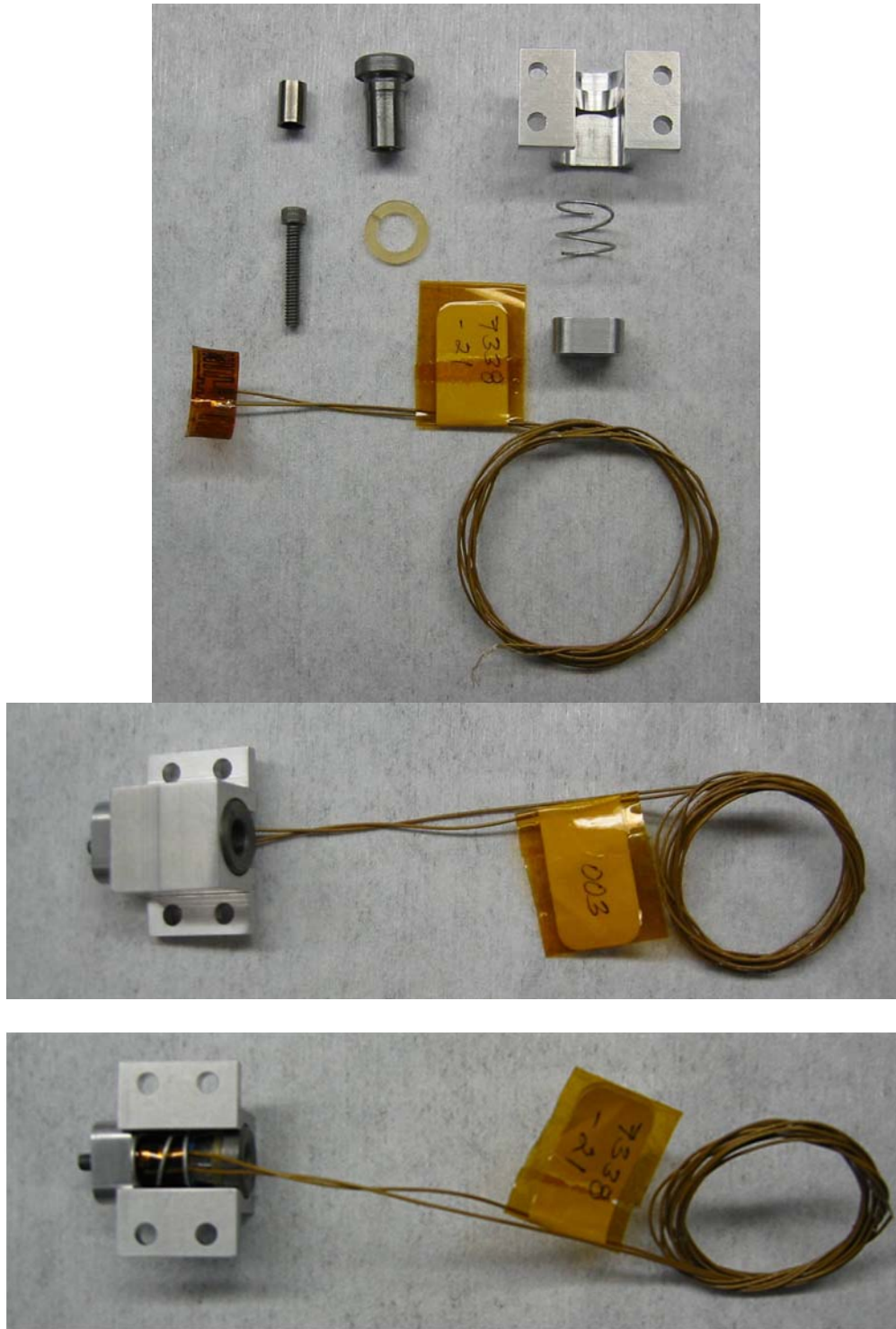
Figure 16.   SMA^{2}C Device EDU Assembled Test Unit. From [4]

When the bushing is heated (activation of the SMA^{2}C device via the Kapton foil heater) the SMA transitions from detwinned martensite to austenite.

The SMA with the retaining bolt will be released from the bushing, allowing the structure to deploy. Figure 17 is a graphical representation of the deployment sequence of the SMA^{2}C EDU.
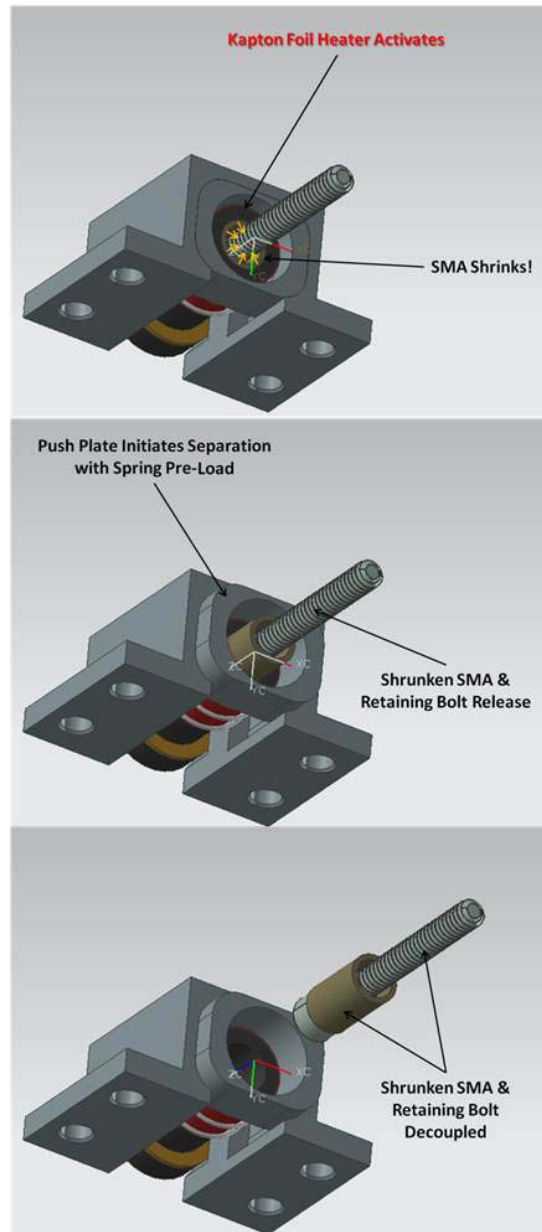
Figure 17.   SMA^{2}C Device Actuation Sequence. From [4]

2.   Testing

Testing parameters were designed to best achieve the goal of utilizing SMA^{2}C as a solar panel deployment mechanism in another Naval Postgraduate School CubeSat thesis, TINYSCOPE. Further discussion of TINYSCOPE's mission, size, and available power is found in another section of this paper.

a.   *Press-Fit and Separation*

Although using heat to bring a shaft and hub together allows a stronger axial holding force, this is not an option when using SMAs. If the hub is heated and the SMA shaft is inserted into the expanded hub, the SMA activates, transitioning from its twinned martensite to austenite phase as heat is transferred between the two pieces. This removes the SMA's ability to perform work when needed. The only available option is to use force to press-fit the SMA into the hub.

Each sample was press-fitted using a press, press pin, and a load cell to measure the force exerted on the SMA as it travels into the hub. Both the SMA and the hub were cleaned and lubricated with isopropyl alcohol before press-fitting. Half the samples were press-fitted in a top-down orientation (depicted in Figure 18 and Figure 19), and the other half were press-fitted in a bottom-up orientation. This was done to compare the holding strength effects of having the SMA continue travel all the way through the hub during extraction versus backing out in the same direction in which it was press-fitted.
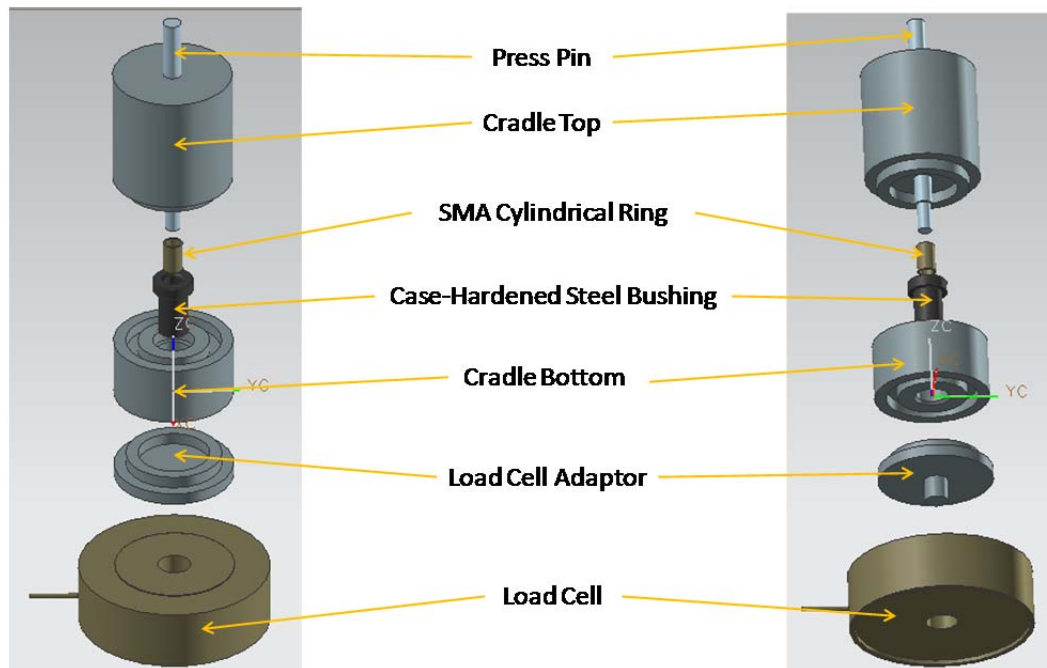
Figure 18.   Components of SMA C Press-Fit Cradle. From [4]

Top Down   Bottom Up
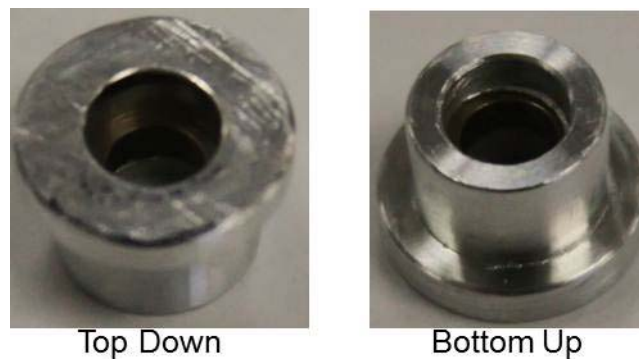
Figure 19.   Press-Fit Orientation

The holding force was tested using an Instron 8500 tensile machine load cell. Each sample is separated in the manner depicted in Figure 20.
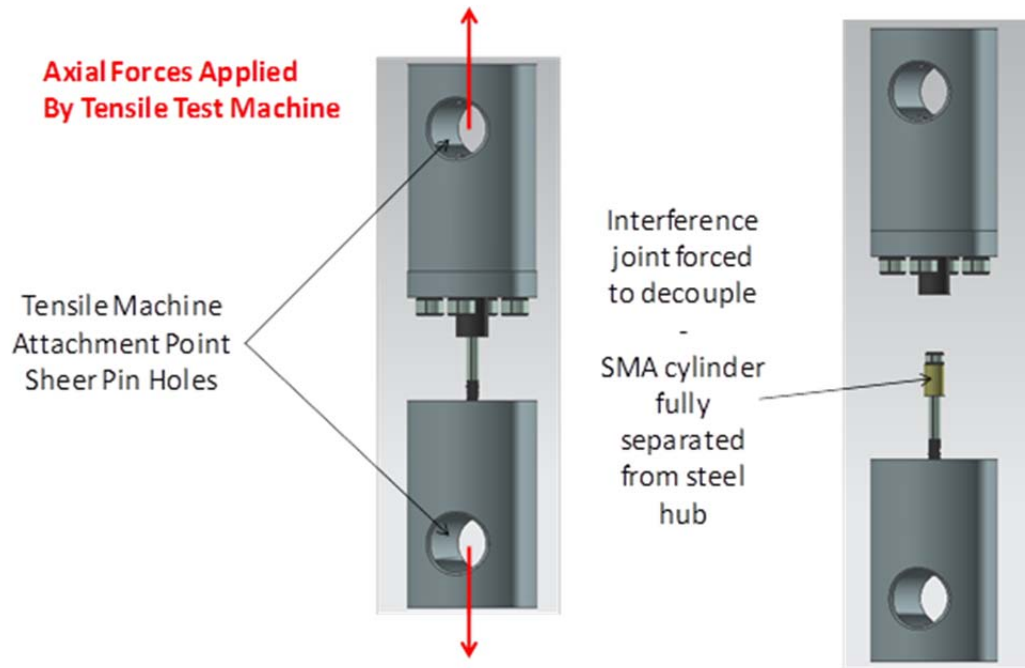
Figure 20.   SMA^{2}C Load Test Rig. From [4]

Using measured SMA and hub inner and outer diameter data, calculations were made to predict the axial holding force. The predictions have been compared to the actual tests. Various samples with three different interferences (1mil, 3mil, and 5mil) were used, see Figure 21.
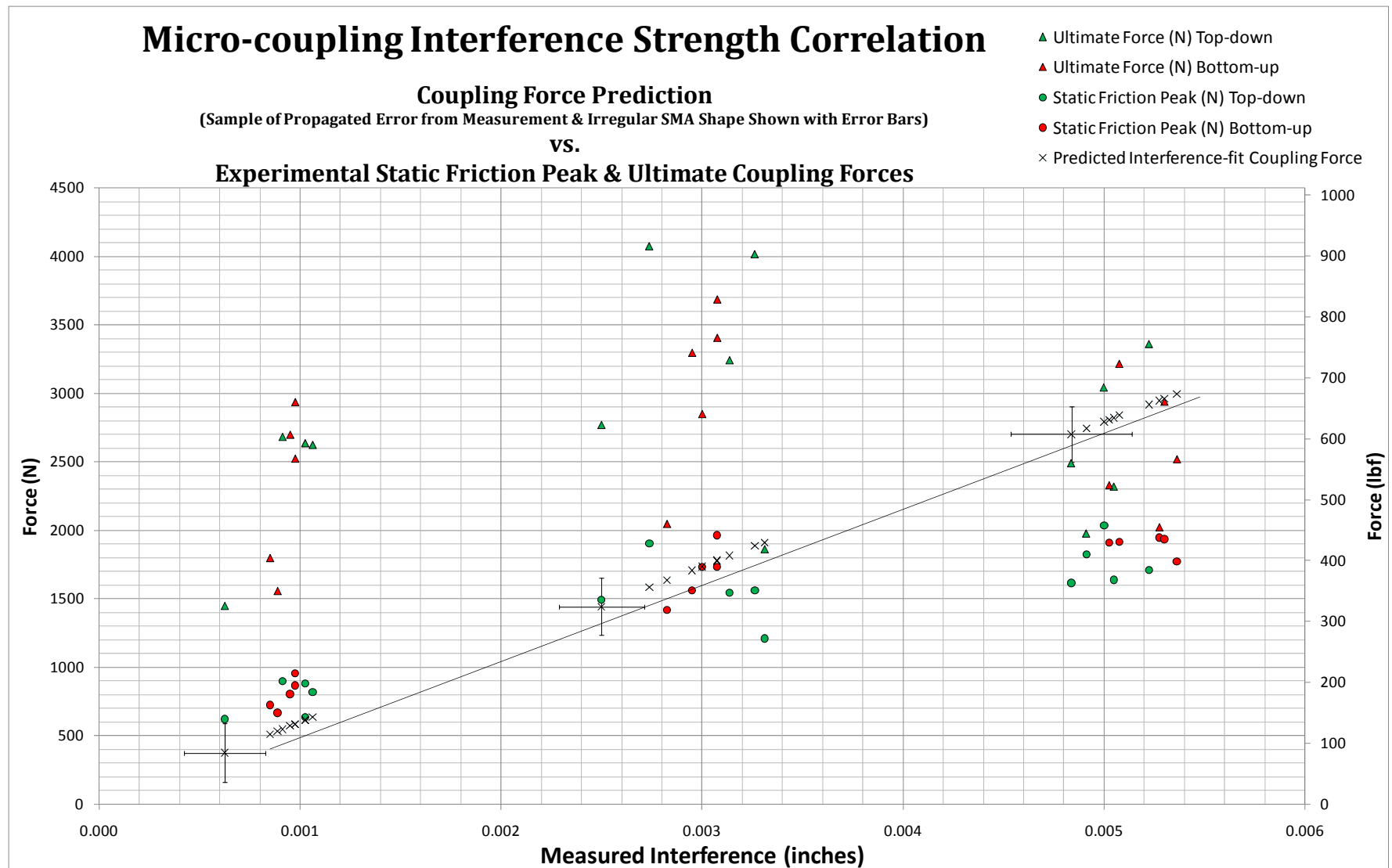
Figure 21.   SMA²C Micro-Coupling Initial and Ultimate Strength Test Data with Predicted Strength Values. From [4]

As mentioned in an earlier section, the intrinsic properties of SMA materials make predicting axial holding force difficult. The predicted values and the experimental values during extraction are shown in Figure 21. The data in Figure 21 also validates the increase in axial holding force with increasing interference values. Additionally, top down press-fitting—compared to bottom up press-fitting samples-had higher holding strength.

b.   Thermal Release

To measure the time and power required for release, testing was conducted in both open air and in a vacuum (29.5 in Hg). The data for both of these tests are shown in Figure 22 and Figure 23. Thermal couples were attached to the steel bushing and Kapton foil heater to record temperature data through actuation.
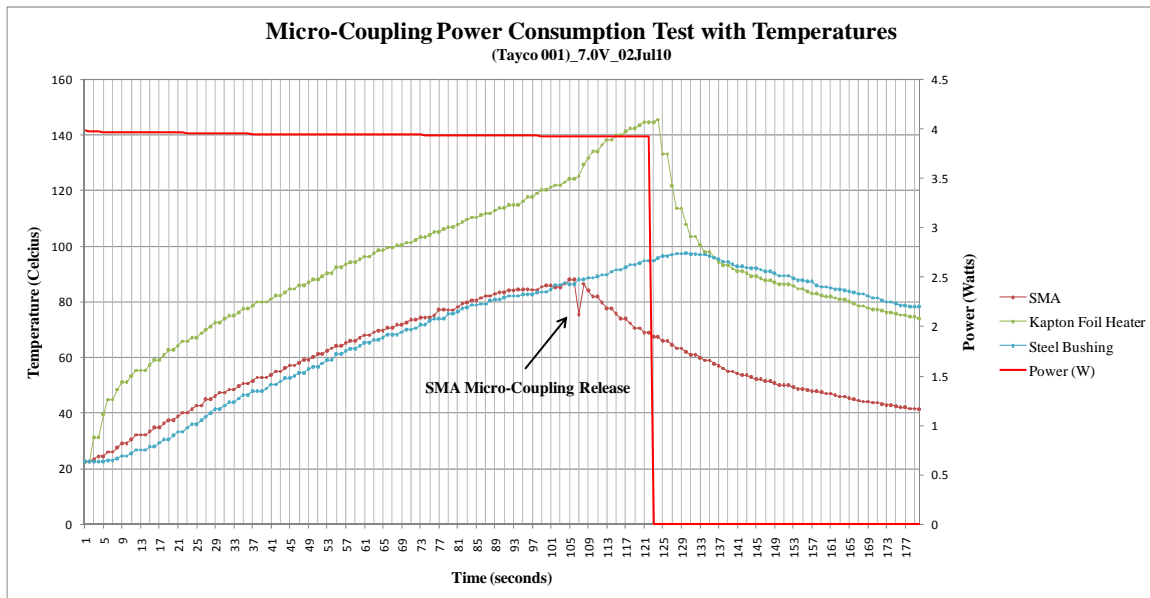
Figure 22.   Open Air Micro-Coupling Mechanism EDU Actuation Temperatures and Power Consumption Data. From [4]
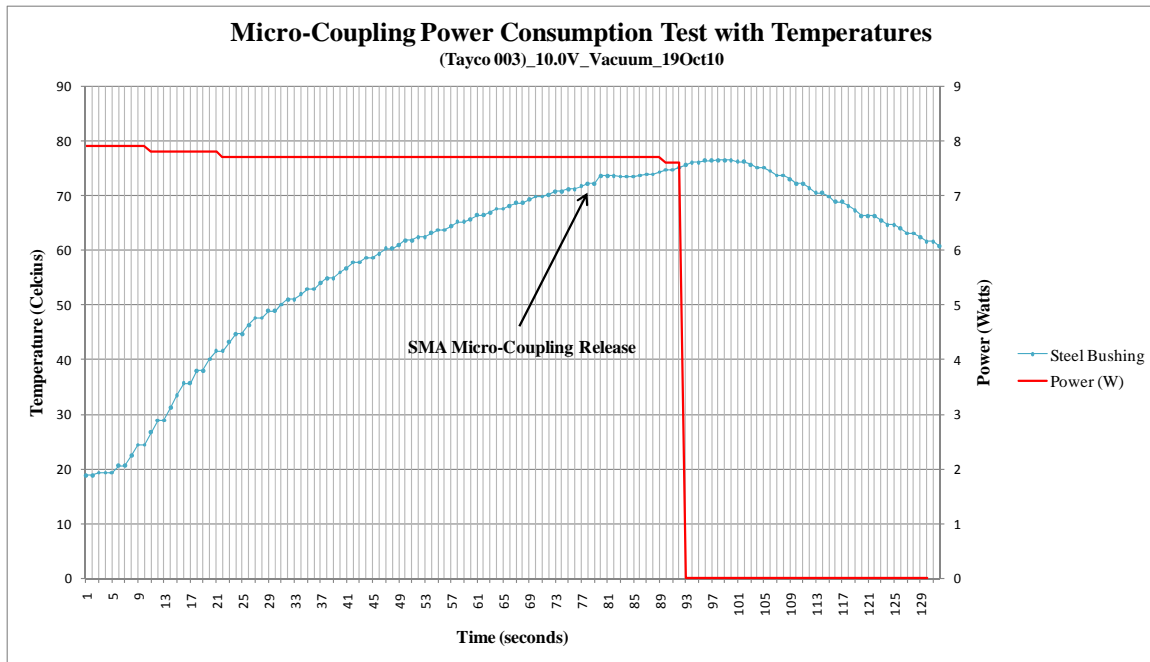
Figure 23.   EDU SMA^{2}C Device Actuation Temperatures and Power Consumption Data in Vacuum. From [4]

The SMA was released in open air in 105 seconds using 4 watts of power. Vacuum release occurred in 80 seconds using 7.74 watts.

3.   Future Work Identified by CDR Will Crane

The EDU possesses the strength needed to secure a CubeSat's solar panel. Additionally, the power it requires for activation is low enough to use TINYSCOPE's bus and onboard battery. Four main areas for future work in the development of the SMA^{2}C device were identified by Crane and include:

1) Reduce the overall device size.

2) Reduce the amount of power needed during activation.

3) Conduct vibration testing.

4) Conduct further thermal testing.

This thesis documents the completion of items 1 -3 of this list.

II.   PRELIMINARY TESTING

Testing was first conducted on the SMA^{2}C EDU to validate Crane's test results and to better understand testing procedures. The holding strength of the SMA^{2}C EDU is around 2,600 N (590 lbf), which greatly surpasses the estimated required holding strength for a CubeSat solar panel weighing 110 g (+/-5 g) [12]. Considering worst-case vibrational loads during launch at 30 GRMS, a minimum holding force of ~135 N (30 lbf)[2] in the axial direction is required. The normal force is directly related to the length of the shaft in Formula 1.8. Reducing the SMA length from 7.8 mm (0.307 in) to 2 mm (0.079 in) should also reduce the holding force to about 150 N (35 lbf).

Prior to purchasing additional materials, all preliminary tests were conducted using available leftover material from the previous thesis (7.8 mm length NiTi SMA's and case-hardened-steel-bushings with three different inner diameter sizes). New NiTi ring sample sizes were cut to compare holding strengths using different ring lengths.

Precautions were taken to reduce actuation via frictional heating of the SMA during cutting on the lathe. The lathe rotational speed was reduced and cold air was blown on the SMA during cutting, preventing any heat build-up. The first cuts on each of the unused NiTi rings experienced slight shrinkage. To minimize waste, two samples were cut from the same 7.8 mm NiTi ring for the 2 mm, and 3 mm length samples.

Unfortunately, the second cut samples experienced even greater shrinkage. The additional shrinkage was caused by stress on the SMA from clamping on the lathe. With the shrinkage during cutting, each sample's outer diameter remains within usable tolerance. (It did not reach the recovered diameter in its austenite phase.)

---

[2] A factor of 4 is added to account for peak forces. 0.1134 kg * 9.8 m/s^2 * 30 *4 = 135 N.

A.   PRESS-FIT

1.   Setup

Each NiTi ring's outer diameter was measured four times at different points and then averaged using the Mitutoyo 293 micrometer (tolerance of +/- 0.001 mm/0.00005 in). The inner diameter was measured using Deltronic gauge pins (step sizes of 0.0001 in). Each case-hardened-steel-bushing was measured in the same fashion as the NiTi rings. The three sets of case-hardened-steel-bushings have inner diameters of 5.05 mm (0.199 in), 5.10 mm (0.201 in), and 5.15 mm (.203 in). The measured NiTi rings and case harden steel bushings were matched by size to maximize the interference. Eight original uncut NiTi rings (only the first 2 mm of each ring is press-fitted) were also used as the control samples for the test.

The applied force during press-fitting was measured using Cooper Instruments LKCP 474 load cell, Cooper Instruments DFI 3900–03 readout, and a Python computer script file. Press-fitting procedure is listed in Appendix A.

2.   Data

Each sample's averaged SMA outer diameter, averaged bushing inner diameter, interference, Peak force, and the median force in both English and SI units are listed in Table 2. Due to slight shrinkage during the NiTi SMA sample cutting, each sample is listed separately in Figure 24. and Figure 25 to compare the effects between cut and uncut samples

The sample data from Table 2 is represented graphically in Figure 24 The NiTi SMA lengths are separated by color group. The cut and uncut 2 mm length NiTi SMAs are plotted in Figure 25.

| Sample | NiTi SMA | | | Bushing | | | | | | | |
	Avg Outer Diameter (mm) d2o	Avg Outer Diameter (in) d2o	Height (mm) L	Avg Inner Diameter (mm) d1o	Avg Inner Diameter (in) d1o	Interference (mm)	Interference (in)	Peak force press-fit(lbf)	Median force press-fit(lbf)	Peak force press-fit(N)	Median force press-fit(N)
1	5.178	0.2039	2.04	5.150	0.2028	0.028	0.0011	8.1	4.8	36.0	21.5
2	5.091	0.2004	2.11	5.043	0.1985	0.049	0.0019	30.0	18.6	133.6	82.6
3	5.085	0.2002	3.03	5.035	0.1982	0.050	0.0020	14.5	9.4	64.7	41.6
4	5.130	0.2019	4	5.103	0.2009	0.027	0.0011	11.7	5.5	51.9	24.7
5	5.091	0.2004	3.99	5.043	0.1985	0.049	0.0019	24.8	9.3	110.5	41.2
6	5.110	0.2012	4.96	5.048	0.1987	0.062	0.0024	13.2	9.9	58.5	44.1
7	5.112	0.2013	4.92	5.055	0.1990	0.057	0.0022	54.0	44.2	240.2	196.4
8	5.105	0.2010	6	5.048	0.1987	0.057	0.0023	36.3	27.1	161.3	120.6
9	5.103	0.2009	6.03	5.045	0.1986	0.058	0.0023	16.1	11.3	71.5	50.2
10	5.120	0.2016	7.02	5.082	0.2001	0.037	0.0015	6.2	4.8	27.8	21.3
11	5.107	0.2010	7	5.048	0.1987	0.059	0.0023	57.0	43.0	253.4	191.4
12	5.190	0.2043	2	5.068	0.1995	0.122	0.0048	139.9	41.1	622.3	182.8
13	5.179	0.2039	7.78	5.153	0.2029	0.027	0.0010	27.4	21.5	121.8	95.6
14	5.185	0.2041	2	5.053	0.1989	0.133	0.0052	69.7	41.9	310.2	186.4
15	5.183	0.2041	2	5.055	0.1990	0.128	0.0050	33.9	23.8	150.6	106.1
16	5.186	0.2042	2	5.050	0.1988	0.136	0.0053	47.8	40.9	212.8	181.9
17	5.192	0.2044	7.84	5.160	0.2031	0.031	0.0012	151.1	21.5	671.9	95.8
18	5.178	0.2038	7.8	5.143	0.2025	0.035	0.0014	26.9	20.7	119.7	91.9
19	5.185	0.2041	2	5.065	0.1994	0.120	0.0047	50.9	39.2	226.4	174.2
20	5.170	0.2035	7.87	5.103	0.2009	0.067	0.0026	16.9	14.3	75.2	63.6
21	5.180	0.2039	2	5.048	0.1987	0.132	0.0052	43.8	34.6	194.8	153.8
22	5.180	0.2039	2	5.100	0.2008	0.080	0.0031	24.9	4.6	110.7	20.6
23	5.180	0.2039	2	5.053	0.1989	0.128	0.0050	25.2	16.0	111.9	71.2

Table 2.   Sample Set 1 Press-Fit Data
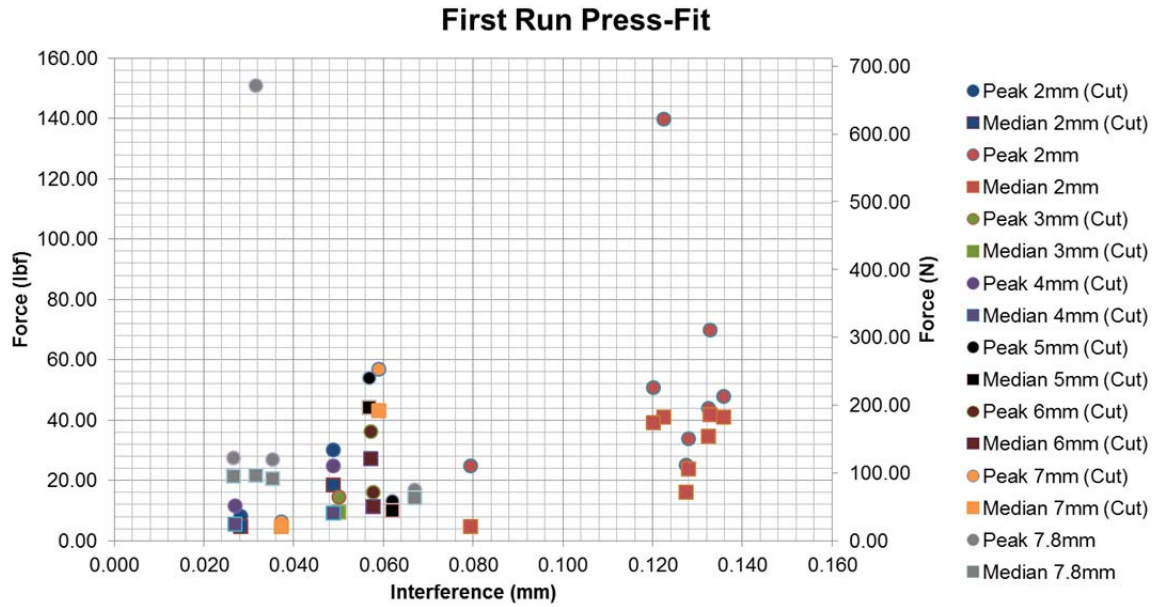
Figure 24.   Sample Set 1 Press-Fit Data
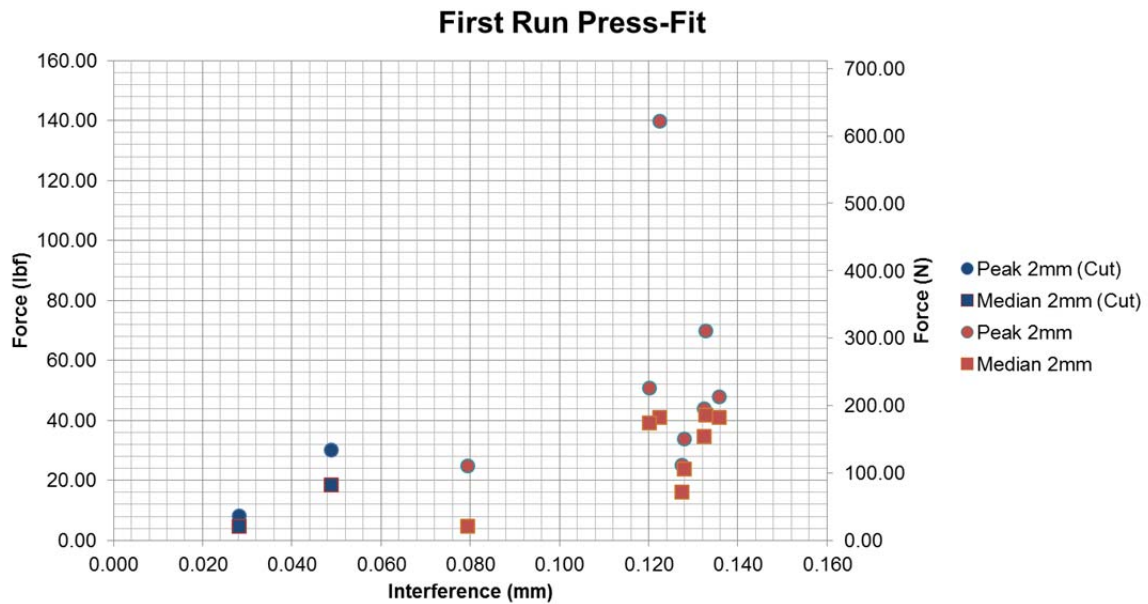
Figure 25.   Sample Set 1 Press-Fit Data (2 mm Length)

3.   Analysis

This preliminary testing was used to measure the relationship between both interference and NiTi SMA length and the force required to press-

32

fit the NiTi SMA into the case-hardened-steel-bushing. As shown in Figure 24 and Figure 25, an increased amount of force is required for higher interferences and/or NiTi SMA ring length. This data was used to correlate the amount of force required during press-fitting and the amount of holding stress achieved in the next subsection.

B.   HOLDING STRENGTH

1.   Setup

With the NiTi SMA rings press-fitted into case-hardened-steel-bushings, each sample was separated using the Instron 8500 tensile machine load cell as depicted in Figure 20. The speed of separation was 0.0021 mm/s for this test. Step by step procedures are listed in Appendix C.

2.   Data

The peak force of separation and steady force of separation are added to the data in Table 2 to give Table 3. The steady force in this experiment is the required separation force at 2 mm of the NiTi SMA travel during separation. This is used to document the difference between the static friction (peak force) and the kinetic friction (steady force).

	NiTi SMA			Bushing											
Sample	Avg Outer Diameter (mm) d2o	Avg Outer Diameter (in) d2o	Height (mm) L	Avg Inner Diameter (mm) d1o	Avg Inner Diameter (in) d1o	Interference (mm)	Interference (in)	Peak force press-fit(lbf)	Median force press-fit(lbf)	Peak force press-fit(N)	Median force press-fit(N)	Peak force sep. (lbf)	Steady force sep (lbf)*	Peak force sep. (N)	Steady force sep (N)*
1	5.178	0.2039	2.04	5.150	0.2028	0.028	0.0011	8.1	4.8	36.0	21.5	40.5	28.9	180.2	128.4
2	5.091	0.2004	2.11	5.043	0.1985	0.049	0.0019	30.0	18.6	133.6	82.6	45.4	24.1	201.9	107.1
3	5.085	0.2002	3.03	5.035	0.1982	0.050	0.0020	14.5	9.4	64.7	41.6	60.3	40.5	268.4	180.0
4	5.130	0.2019	4	5.103	0.2009	0.027	0.0011	11.7	5.5	51.9	24.7	24.5	20.2	109.2	89.9
5	5.091	0.2004	3.99	5.043	0.1985	0.049	0.0019	24.8	9.3	110.5	41.2	84.9	45.2	377.8	201.1
6	5.110	0.2012	4.96	5.048	0.1987	0.062	0.0024	13.2	9.9	58.5	44.1	122.3	82.5	543.9	366.8
7	5.112	0.2013	4.92	5.055	0.1990	0.057	0.0022	54.0	44.2	240.2	196.4	153.6	100.0	683.1	444.8
8	5.105	0.2010	6	5.048	0.1987	0.057	0.0023	36.3	27.1	161.3	120.6	176.4	116.5	784.9	518.4
9	5.103	0.2009	6.03	5.045	0.1986	0.058	0.0023	16.1	11.3	71.5	50.2	118.9	50.8	528.9	225.9
10	5.120	0.2016	7.02	5.082	0.2001	0.037	0.0015	6.2	4.8	27.8	21.3	92.7	76.9	412.3	341.9
11	5.107	0.2010	7	5.048	0.1987	0.059	0.0023	57.0	43.0	253.4	191.4	233.9	103.9	1040.6	462.3
12	5.190	0.2043	2	5.068	0.1995	0.122	0.0048	139.9	41.1	622.3	182.8	82.7	34.3	368.1	152.5
13	5.179	0.2039	7.78	5.153	0.2029	0.027	0.0010	27.4	21.5	121.8	95.6	176.1	124.4	783.5	553.2
14	5.185	0.2041	2	5.053	0.1989	0.133	0.0052	69.7	41.9	310.2	186.4	76.8	39.2	341.7	174.3
15	5.183	0.2041	2	5.055	0.1990	0.128	0.0050	33.9	23.8	150.6	106.1	105.1	49.6	467.6	220.7
16	5.186	0.2042	2	5.050	0.1988	0.136	0.0053	47.8	40.9	212.8	181.9	104.8	41.8	466.2	185.8
17	5.192	0.2044	7.84	5.160	0.2031	0.031	0.0012	151.1	21.5	671.9	95.8	303.0	165.7	1348.0	737.3
18	5.178	0.2038	7.8	5.143	0.2025	0.035	0.0014	26.9	20.7	119.7	91.9	166.4	65.1	740.1	289.8
19	5.185	0.2041	2	5.065	0.1994	0.120	0.0047	50.9	39.2	226.4	174.2	73.4	36.4	326.7	162.1
20	5.170	0.2035	7.87	5.103	0.2009	0.067	0.0026	16.9	14.3	75.2	63.6	289.3	173.0	1286.7	769.6
21	5.180	0.2039	2	5.048	0.1987	0.132	0.0052	43.8	34.6	194.8	153.8	81.1	43.0	360.6	191.1
22	5.180	0.2039	2	5.100	0.2008	0.080	0.0031	24.9	4.6	110.7	20.6	76.7	36.9	341.2	164.3
23	5.180	0.2039	2	5.053	0.1989	0.128	0.0050	25.2	16.0	111.9	71.2	101.0	47.2	449.3	209.9

Table 3.   Sample Set 1 Separation Data

As mentioned in Equation 1.2 and 1.8, the holding force is a function of both SMA ring length and interference between SMA ring and hub. This preliminary test varies both parameters. To better visualize both effects, each sample is grouped into their lengths and plotted in Figure 26 and Figure 27.
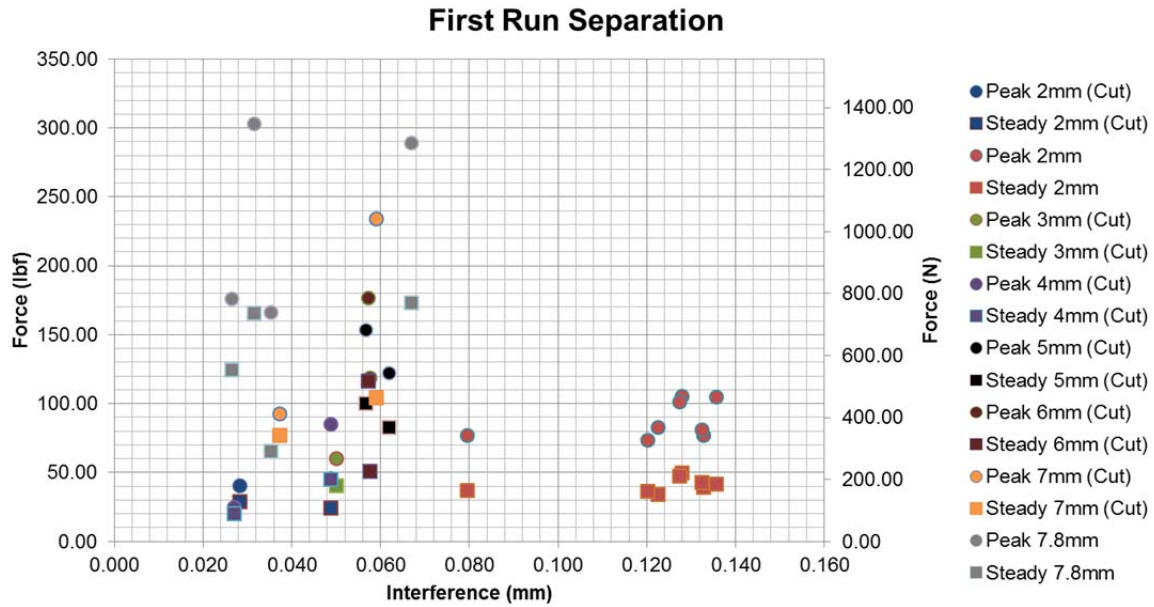
Figure 26.   Sample Set 1 Separation Data
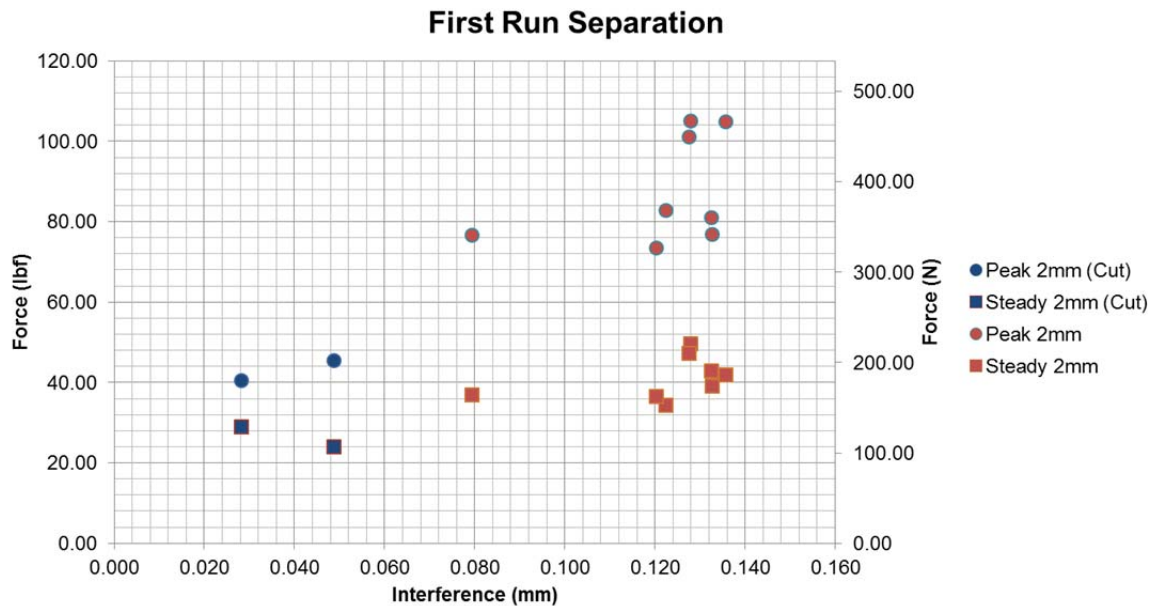
Figure 27.   Sample Set 1 Separation Data (2 mm Length)

3.   Analysis

As with press-fitting, an increase in interference and/or length strengthens the holding force. The peak force in all cases surpassed the

estimated 135 N (30 lbf) required holding strength. For the uncut 7.8 mm NiTi SMA rings inserted only 2mm into the case-hardened-steel-bushing, both peak force and steady force surpassed the 135 N (30 lbf) estimated required holding strength.

The peak separation force is greater than the peak press-fit force for every sample in this set. A contributing factor to this phenomenon is due to the case-hardened-steel-bushing's hardness property. During press-fitting, the case-hardened-steel-bushing undergoes little to no change in its inner diameter. The SMA continues to undergo stress during extraction, therefore increasing the force needed to extract the SMA ring.

III. TRADE OFF AND DESIGN

The three driving forces behind the design of the new coupling mechanism are to minimize size, mass, and activation energy from the previous unit. This goal is echoed in the selection of each component.

A. SMA

Of the various types of SMAs, the author elected to use the NiTi based SMA. The NiTi SMA was successfully used in the previous thesis, and performed well during preliminary testing in this thesis. In addition, the NiTi SMA has a greater amount of research and commercial use compared to other types of SMAs, allowing the use of existing data. Reducing the SMA ring size also reduces the mass and the amount of power required for activation.

Intrinsic Devices Inc. specializes in manufacturing NiTi products for fastening, sealing, and electrical interconnections. In keeping with roughly the same inner and outer diameters from the samples used above, this thesis selected the AGM0396–0064–0200 part number. The following are the supplied NiTi SMA properties:

1) G type NiTi composition with an As temperature range of 95–105°C (203–221°F).

2) Minimum supplied inner diameter of   3.96 mm

3) Maximum recovered inside diameter of   3.77 mm

4) Radial thickness range supplied of   0.61–0.66 mm

5) Axial length supplied between   1.9–2.1 mm

6) Minimum outer diameter shrinkage of   0.19 mm

7) Poisson's ratio   0.33

8) Yield strength   415 Mpa (60 kpsi)

9) Ultimate tensile strength   800 MPa (115 kpsi)

10) Young's modulus in tension   75 Gpa (11×10^6 psi)

11) Density   6.5 g/cm^3(0.235 lb/in^3)

12) Thermal conductivity   0.18 W/(cm-^{o}C) (10.4 BTU/(hr-ft-^{o}F)

The G type was selected to mitigate any pre-actuation due to ambient temperature changes between press-fitting and desired actuation in space. With specified supplied tolerances, the NiTi SMA rings' outer diameters range between 5.18 mm – 5.28 mm. Fully actuated outer diameters, in the austenite phase, are between 4.99 mm – 5.09 mm. Due to successful preliminary testing, 2 mm length rings meet the estimated holding force. This reduces the original size by a factor of 4.

B.   BUSHING

Crane selected case-hardened steel "press-fit-with -head" drill bushings for its material properties, particularly its high Young's modulus value and hardness. The bushings are manufactured with a high tolerance of +0.0001 in to +0.0004 in, providing good consistency between samples. Although smaller case hardened steel press-fit-with-head drill bushings are available, this author chose to explore other materials to use to minimize mass and power while maintaining the required holding force.

Aluminum alloys, although not as hard as steel, have lower density and higher thermal conductivity. The higher thermal conductivity allows heat to pass through with less resistance. These properties are ideal in reaching our goal to minimize mass and required power. Of all the aluminum alloys, 7075-T6 , 2024-T6, and 6061 T-6 are further considered in this thesis. Table 4 lists the different material properties for high carbon steel and various aluminum alloys.

	Young's Modulus (Gpa)	Young's Modulus (x 10^6 psi)	Tensile Yield Strength (Mpa)	Tensile Yield Strength (x 10^6 psi)	Poison's Ratio	Thermal Conductivity (W/(cm-°C))	Thermal Conductivity (BTU/(hr-ft-°F))	Density (g/cm^3)	Density (lb/in^3)	Machinability	Coefficient of Thermal Expansion (x10^{-6}/°C)	Coefficient of Thermal Expansion (x10^{-6}/°F)
Al 7075-T6	71.7	10.4	503	73	0.33	130	75.2	2.81	0.1	70%	23.6	13.1
Al 6061-T6	68.9	10	276	40	0.33	167	96.6	2.7	0.1	50%	23.2	12.9
AL 2024 T-6	72.4	10.5	345	50	0.33	151	87.3	2.78	0.1	70%	23.6	13.1
High Carbon Steel (AISI 1020)	207	30.015	350	50.8	0.29	51.9	30	7.87	0.28	65%	12.8	7.11
NiTi SMA (martensite)	30	4.35			0.33	0.18	10.4	6.5	0.24		11	6.1

Table 4.   Bushing Material Property Comparison. After [13]

All three aluminum alloys have similar material properties. Although Al 2024 T-6 has the highest thermal conductivity (equates to lower resistance and therefore less power required to activate the mechanism), this author selected the Al 7075-T6 due to higher tensile yield stress, higher corrosive resistance property, and significant space flight heritage.

The bushings, using the chosen Al 7075-T6 as the material type, are not commercially available with the required dimensions. Therefore, the bushings used in this thesis are from a solid AL 7075-T6 rod machined into bushings at the NPS machine shop. Care needs to be taken in manufacturing these parts, as their tolerances are quite tight (+/- 0.0001 in) and reproducibility can be a challenge. Two bushing styles in conjunction with the housings are shown in Figure 28 and Figure 29.

Two sets of bushing style A are machined with dimensions:

1) 5.156 mm and 5.182 mm (0.203 in and 0.204 in) inner diameter

2) 6 mm (0.236 in) total height

3) 8 mm (0.315 in) outer diameter of smaller section, 10.8 mm (0.425 in) outer diameter of head.

Bushing style A was ultimately chosen due to the smaller overall size when integrated into the respective housing. Further information on the style chosen is in the housing section below.
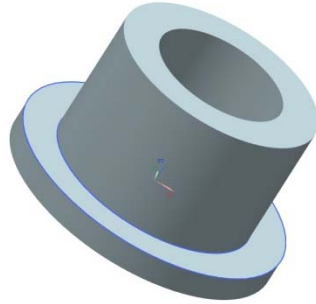
Figure 28.   Bushing Style A
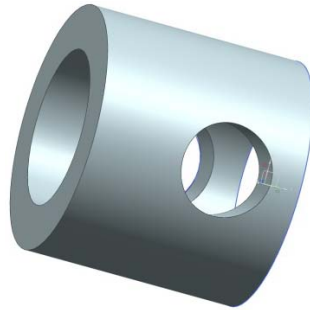
Figure 29.   Bushing Style B

C.   HEATING ELEMENT

Kapton foil heating elements are flexible heaters used in various applications throughout different industries. Tayco Engineering manufactures flexible heaters to include etched foil heaters (Figure 30). These heaters etch the heating element between the two Kapton layers.

Figure 30.   Tyco Engineering Inc. Flexible Heater. From [14]

The flexible heaters have low outgassing properties, can heat up to 232°C (450°F), and have significant space flight heritage. Using the dimensions of bushing style A, the required size needed is 25.13 mm x 4 mm (0.989 in x 0.18 in). The smallest pre-manufactured size available is 50 mm x 10 mm (2 in x 0.5 in). Although Custom manufacturing is available, the high cost (starting at $10,000.00 USD) of producing a low quantity custom order makes it prohibitive for this thesis. Another viable option is to wrap heater wire around the bushing as the heating element.

Nichrome wire comes in two variants, Nichrome 80 (also known as Nichrome A) and Nichrome 60 (also known as Nichrome C). Nichrome 80 is composed of 80% Nickel and 20% Chromium, while Nichrome 60 is composed of 60% Nickel, 16% Chromium, and the rest is a Silicon and Iron balance. Material properties for both types of Nichrome wire are listed in Table 5.

	Density (g/cm^3)	Density (lb/in^3)	Tensile Yield Strength (Mpa)	Tensile Yield Strength (x 10^6 psi)	Melting Point (Deg $^{\circ}$C)	Melting Point (Deg $^{\circ}$F)	Temperature Coefficient of Resistance (Ohms/Ohm/ Deg $^{\circ}$C)
Nichrome 60	8.2458	0.2979	758.4	0.11	1350	2460	0.00015
Nichrome 80	8.4119	0.3039	827.4	0.12	1400	2550	0.000085

Table 5.   Nichrome Data. After [15]

Both materials have similar characteristics. This thesis chose Nichrome 80 for its lower temperature coefficient of resistance per degree of change, and nonmagnetic attraction.

The heat dissipated by the Nichrome wire is directly proportional to the amount of current passing through the wire. The higher the current, the more heat produced by the wire. Current (I, measured in Amps) passing through the wire is a function of voltage (V, measured in Volts) and resistance (R, measured in Ohms)

V=I*R   (2.1)

To wrap the bushing 6 times, a 150 mm (5.91 in) length of Nichrome wire was needed in addition to 20 mm (0.75 in) for use as lead wire. A self-imposed power limit of 3.5 volts and 0.75 amps was used to select the proper wire gauge. Using Equation 2.1, this requires 4.66 ohms of resistance.

As seen in Table 6, Nichrome 80 gauge 31 wire and below provide 205°C (400°F) using the maximum current of 0.75 amps.

			Approximate Amperes to Heat NiChrome Wire
Gauge Wire	Diameter (mm)	°F °C	400 205	600 316	800 427	1000 538	1200 649	1400 760	1600 871	1800 982	2000 1093
10	2.591		16.2	23.3	29.7	37.5	46.0	56.0	68.0	80.0	92.0
11	2.311		13.8	19.2	24.8	31.5	39.0	48.0	57.0	67.0	78.0
12	2.057		11.6	16.1	20.8	26.5	33.5	40.8	48.0	56.0	65.0
13	1.829		9.80	13.6	17.6	22.5	28.2	34.2	41.0	48.0	55.0
14	1.626		8.40	11.6	15.0	18.8	23.5	29.0	34.6	40.5	46.0
15	1.448		7.20	10.0	12.8	16.1	20.0	24.5	29.4	34.3	39.2
16	1.295		6.40	8.70	10.9	13.7	17.0	20.9	25.1	29.4	33.6
17	1.143		5.50	7.50	9.50	11.7	14.5	17.6	21.1	24.6	28.1
18	1.016		4.80	6.50	8.20	10.1	12.2	14.8	17.7	20.7	23.7
19	0.914		4.30	5.80	7.20	8.70	10.6	12.7	15.2	17.8	20.5
20	0.813		3.80	5.10	6.30	7.60	9.10	11.0	13.0	15.2	17.5
21	0.7239		3.30	4.30	5.30	6.50	7.80	9.40	11.0	12.9	14.8
22	0.6426		2.90	3.70	4.50	5.60	6.80	8.20	9.60	11.0	12.5
23	0.5740		2.58	3.30	4.00	4.90	5.90	7.00	8.30	9.60	11.0
24	0.5105		2.21	2.90	3.40	4.20	5.10	6.00	7.10	8.20	9.40
25	0.4547		1.92	2.52	3.00	3.60	4.30	5.20	6.10	7.10	8.00
26	0.4039		1.67	2.14	2.60	3.20	3.80	4.50	5.30	6.10	6.90
27	0.3607		1.44	1.84	2.25	2.73	3.30	3.90	4.60	5.30	6.00
28	0.3200		1.24	1.61	1.95	2.38	2.85	3.40	3.90	4.50	5.10
29	0.2870		1.08	1.41	1.73	2.10	2.51	2.95	3.40	3.90	4.40
30	0.2540		0.92	1.19	1.47	1.78	2.14	2.52	2.90	3.30	3.70
31	0.2261		0.77	1.03	1.28	1.54	1.84	2.17	2.52	2.85	3.2
32	0.2032		0.68	0.90	1.13	1.36	1.62	1.89	2.18	2.46	2.76
33	0.1803		0.59	0.79	0.97	1.17	1.40	1.62	1.86	2.12	2.35
34	0.1600		0.50	0.68	0.83	1.00	1.20	1.41	1.60	1.80	1.99
35	0.1422		0.43	0.57	0.72	0.87	1.03	1.21	1.38	1.54	1.71
36	0.1270		0.38	0.52	0.63	0.77	0.89	1.04	1.19	1.33	1.48
37	0.1143		0.35	0.46	0.57	0.68	0.78	0.9	1.03	1.16	1.29
38	0.1016		0.30	0.41	0.50	0.59	0.68	0.78	0.88	0.98	1.09
39	0.0889		0.27	0.36	0.42	0.49	0.58	0.66	0.75	0.84	0.92
40	0.0787		0.24	0.31	0.36	0.43	0.50	0.57	0.64	0.72	0.79

Table 6.   Nichrome Wire Gauge, Temperature, Current Correlation. From [16]

As seen in Table 7, the 31 gauge Nichrome 80 wire has a total of 4.57 ohms when 170 mm (6.69 in) length is used. Having the 31 gauge 170 mm (6.69 in) Nichrome 80 wire, a total of 4.57 Ohms, 3.5 volts, 0.76 amps provide 205°C (400°F) to the bushing.

	NICHROME 60 ALLOY 675				NICHROME 80 ALLOY 650		
GAUGE SIZE	DIAMETER (in)	MM	OHMS/FT	GAUGE SIZE	DIAMETER (in)	MM	OHMS/FT
22	0.025	0.643	1.055	22	0.0253	0.6426	1.0155
23	0.023	0.574	1.322	23	0.0226	0.5740	1.2726
24	0.020	0.511	1.671	24	0.0201	0.5105	1.6089
25	0.018	0.455	2.107	25	0.0179	0.4547	2.0287
26	0.016	0.404	2.670	26	0.0159	0.4039	2.5711
27	0.014	0.361	3.348	27	0.0142	0.3607	3.2236
28	0.013	0.320	4.252	28	0.0126	0.3200	4.0942
29	0.011	0.287	5.286	29	0.0113	0.2870	5.0905
30	0.010	0.254	6.750	30	0.0100	0.2540	6.5000
31	0.009	0.226	8.522	31	0.0089	0.2261	8.2060
32	0.008	0.203	10.547	32	0.0080	0.2032	10.1563
33	0.007	0.180	13.390	33	0.0071	0.1803	12.8943
34	0.006	0.160	17.007	34	0.0063	0.1600	16.3769
35	0.006	0.142	21.524	35	0.0056	0.1422	20.7270
36	0.005	0.127	27.000	36	0.0050	0.1270	26.0000

Table 7.   Nichrome 80 and Nichrome 60 Gauge Versus Resistance. After [15]

D.   HOUSING

1.   Design I

The first housing consideration was to keep the same design while decreasing the length. By decreasing the bushing from 15.875 mm (0.625 in) to 6 mm (0.236 in), the new housing is reduced to 27.94 mm (1.1 in) by 7.90 mm (0.311 in) by 12.7 mm (0.5 in). Use of Nichrome wire vice the Kapton foil heater presents some difficulty. There is little room for the Nichrome wire as it is thicker than the Kapton foil heater once installed around the bushing. Despite the strength and stability of this design, this thesis aimed to minimize any unused space and eliminate the need for extra parts such as thermally isolating washers and push plates (although a spring can still be used for pre-tensioning).

The second consideration was the implementation of the housing in the CubeSat. With this design, the housing needed to be installed on the adjacent panel. Although not a structural or size constraint problem, having the housing attached to the adjacent panel makes removal of that panel problematic, as the deployable structure would have to be removed from SMA^{2}C. Secondly, angle consideration during attachment of the housing to the adjacent panel needed to be taken into account to have the deployment angle parallel to the deployment path. (Solar panels travel a circular/arc path they are hinged at one end and secured on the opposite end.)

2. Design II

To avoid attachment angle difficulties and un-restrict housing placement (on the facing panel or adjacent panel), a pivot design was considered. Figure 31 and Figure 32 are different views of this design.
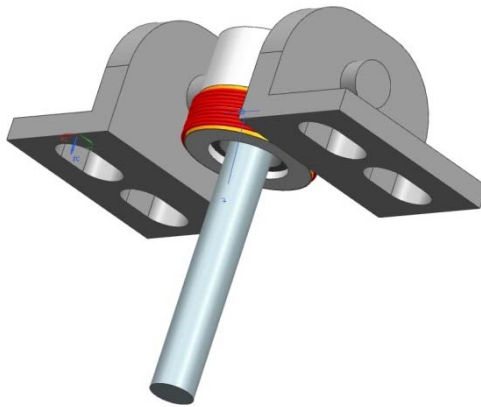
Figure 31.   Design Concept II Bottom View
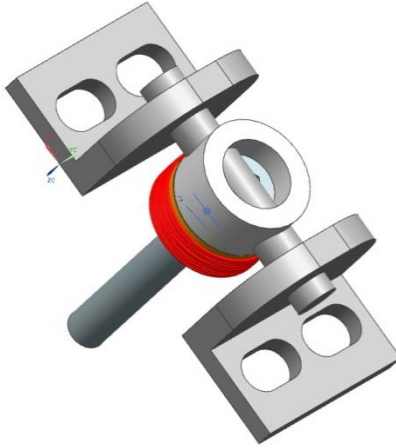
Figure 32.   Design Concept II Top View

This design allows the bushing to rotate as needed (very small angle) during deployment. It also allows the unit to be installed on any of the panels. Lastly, this design solved the need for additional space for the Nichrome wire. The dimensions are 28.81 mm (1.13 in) by 13 mm (0.52 in) by 10 mm (0.39 in). The one drawback to this design is the additional space needed compared to design I.

3.   Design III

In keeping with the same bushing design selected in the previous section, an open-air housing approach was used. Figure 33 and Figure 34 are different views of this design.
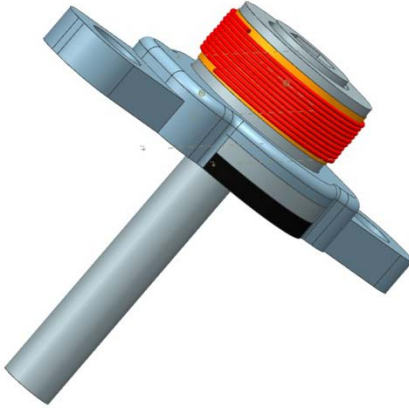
Figure 33. Design III Side View
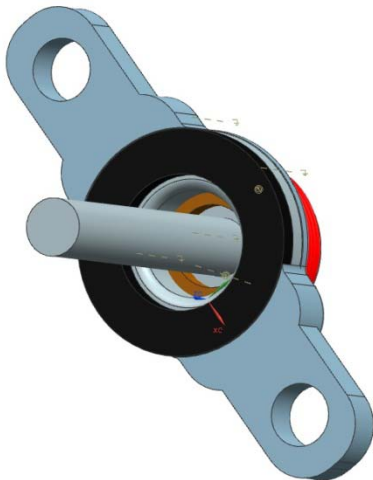
Figure 34. Design III Bottom View

The new dimensions are 26.8 mm (1.06 in) by 10.9 mm (0.43 in) by 7 mm (0.28 in); a reduction compared to the original SMA^{2}C and Design I. A comparison of all the design dimensions is listed in Table 8.

	Length (mm)	Width (mm)	Height (mm)	Length (in)	Width (in)	Height (in)
SMA2C	27.94	17.78	12.7	1.1	0.7	0.5
Design I	27.94	7.9	12.7	1.1	0.31	0.5
Design II	28.81	10	13	1.13	0.39	0.52
Design III	26.8	10.9	7	1.06	0.43	0.28

Table 8.   Housing Dimensions

46

Materials used for the previous two designs are aluminum. This design uses polycarbonate (PC) material printed with a Fortus 3D printer available for student use at NPS.

The 3D printing on the Fortus 3D production system using the PC material produces functional end-use parts. Parts made on this printer are widely used in the automotive, aerospace, medical, and various other industries. [17] The PC material is not only strong enough to be used as the housing material, but is also thermally insulating The thermally insulating (not thermally conductive) property serves as the thermal washer, eliminating the need for additional material between the bushing and housing. Because the A_s temperature for the SMA is 95–105°C (203–221°F), the PC material can withstand such temperatures as listed in Table 9.

Mechanical Properties	Metric	English
Tensile Strength	68 MPa	9,800 psi
Tensile Modulus	2,300 Mpa	330,000 psi
Thermal Properties	Deg C	Deg F
Heat Defelection @ 66 psi	138	280
Heat Deflection @ 264 psi	127	261
Vicat Softening	139	282
Glass Transition	161	322

Table 9.   Polycarbonate Material Properties. After [17]

E.   EDU

The final EDU consist of a 4–40 A286 alloy screw for use as a retaining bolt, PC housing, 31 gauge Nichrome wire, Kapton tape, NiTi ring, Al 7075-T6 bushing, and a thin PC washer. For added security, especially during vibrations due to launch, a thin layer of thermal epoxy (TRA-BOND 2151) is added around the upper rim of the Kapton tape.

All the components of the EDU are shown in Figure 35 and Figure 36. Actual EDUs used during testing are shown in Figure 37 and Figure 38. A hex washer is used against the top side of the bushing to prevent the retaining bolt from falling inside the CubeSat during installation. In Figure 38 the hex bolt is seen resting on the bushing, with and without the PC washer.
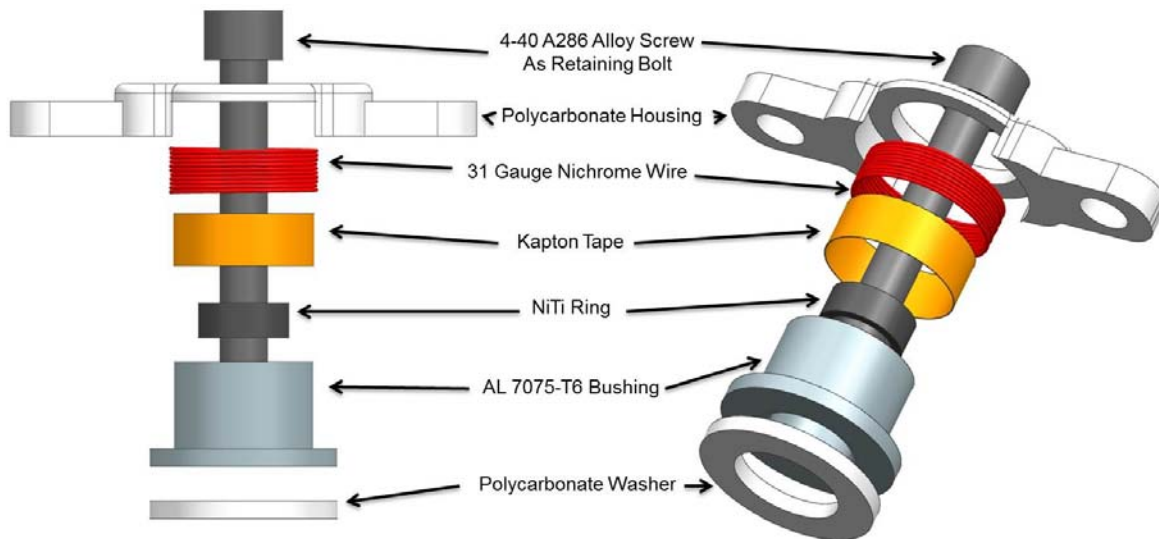
Figure 35.   Engineering Design Unit
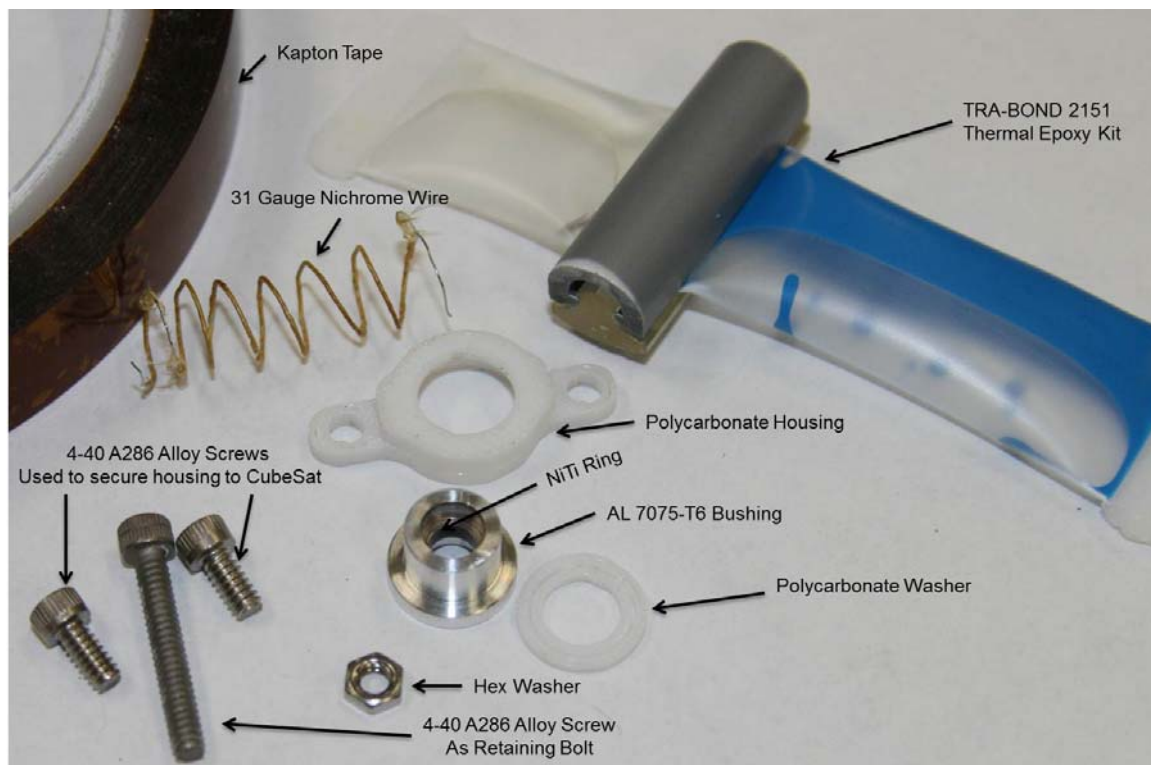
Figure 36.   EDU Sub Components
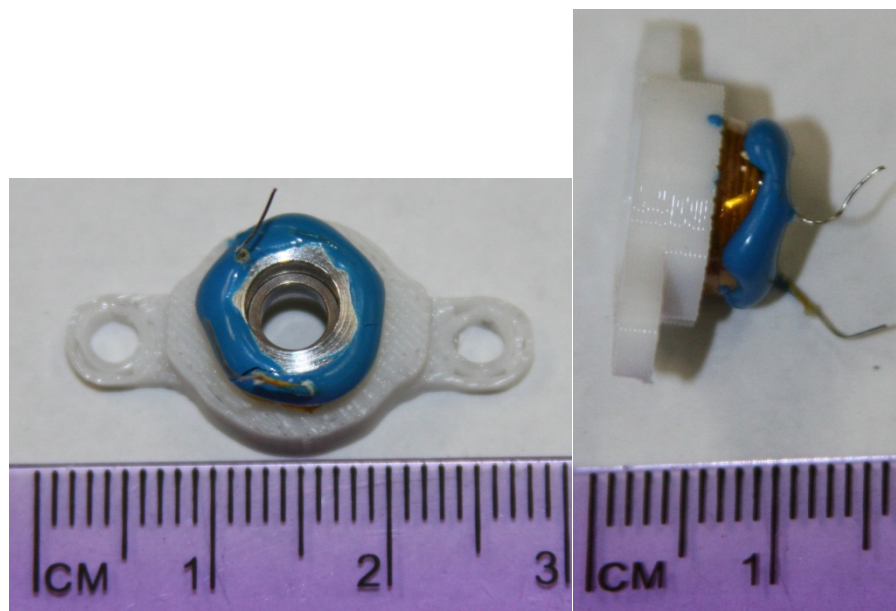
Figure 37.   EDU

Figure 38.   EDU with Hex Washer

IV. TESTING

With the design phase complete, the EDU was tested to validate performance. Two sets of strength tests, two sets of thermal releasability tests, and one set of vibrational testing were performed. Each testing procedures' step by step instructions are listed in Appendices A-E. Below are the different tests conducted and their results.

A. STRENGTH

1. Press-Fit Sample Set Two

a. Setup

Six Al 7075-T6 bushings were machined from a solid rod. The inner diameters of the bushings varied between 5.072 mm – 5.156 mm (0.1997 in– 0.2030 in). Two samples with the case-hardened-steel-bushings were used (samples 7 and 8) to determine the effects of using Al 7075-T6 vice using the case-hardened steel for the bushing material. Measurements for the inner diameters were taken using the Deltronic gauge pins (step sizes of 0.0001 in).

Ten new 2 mm length NiTi rings' outer diameters were measured in four separate locations using the Mitutoyo 293 micrometer (tolerance of +/- .001 mm/0.00005 in). The measurements were then averaged and listed in Table 10. The inner diameter was measured using the gauge pins. Each NiTi ring and bushing was then matched according to their size (smallest NiTi with the smallest inner diameter bushing).

The measuring device, Cooper Instruments LKCP 474 load cell and Cooper Instruments DFI 3900–03 readout, has a data recording frequency of once per second. During the press-fitting of this sample set, a fine threaded press is used. This allows for a slower press-fitting operation to get additional

data from the load cell. The items and overall set-up used for press-fitting are seen in Figure 39. Appendix A lists step-by-step procedures used for press-fitting.

Figure 39.   Press-Fit Setup

Figure 40 is a close up view of the separation set-up. Appendix C list step-by-step procedures used for force separation of the SMA from the bushing.
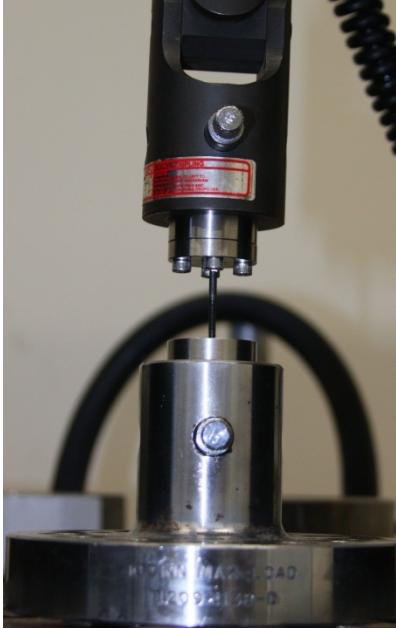
Figure 40.   Separation Testing

b.   Data

Table 10 lists each sample's measurements prior to press-fitting. The peak and median force is also recorded and listed in Table 10.

	NiTi SMA			Bushing							
Sample	Avg Outer Diameter (mm) d2o	Avg Outer Diameter (in) d2o	Height (mm)	Avg Inner Diameter (mm) d1i	Avg Inner Diameter (in)	Interference (mm)	Interference (in)	Peak force press-fit(lbs)	Median force press-fit(lbs)	Peak force press-fit(N)	Median force press-fit(N)
1	5.282	0.2079	2	5.072	0.1997	0.209	0.0082	169.8	19.5	755.5	86.8
3	5.285	0.2081	2	5.116	0.2014	0.170	0.0067	189.4	41.3	842.6	183.7
4	5.286	0.2081	2	5.118	0.2015	0.168	0.0066	82.8	61.8	368.4	274.8
5	5.290	0.2083	2	5.138	0.2023	0.151	0.0060	145.0	39.0	645.2	173.3
6	5.292	0.2084	2	5.156	0.2030	0.136	0.0054	149.3	46.7	664.2	207.6
7	5.293	0.2084	2	5.151	0.2028	0.142	0.0056	112.5	44.4	500.3	197.6
8	5.293	0.2084	2	5.149	0.2027	0.144	0.0057	139.2	36.9	619.4	164.3

Table 10.   Sample Set 2 Press-Fit Data

Figure 41 is a plot of the peak and median amount of force needed to press-fit each sample.vs. the interference of each sample.
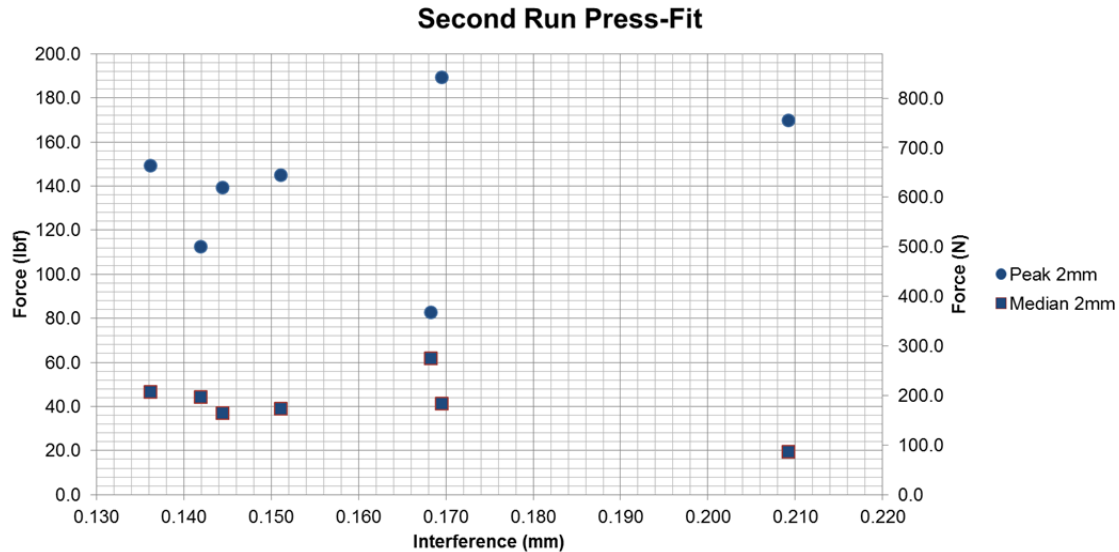
Figure 41.   Sample Set 2 Press-Fit Data

c.   *Analysis*

Problems, such as galling, were evident during the press-fit using the fine threaded press. The initial theory is that the problem was caused by the Al 7075-T6's inability to withstand the tighter interferences. (After running sample set 3 with the original press, it is concluded that the problem lies in using the fine threaded press. The fine threaded press does not have enough strength to conduct the press-fit, and therefore causes the NiTi ring to come in at an angle (vice parallel) to the bushing. Sample number two had severe galling and it is not included in the data.)

The correlation between interference and force required to press-fit the samples is shown in Table 10 and Figure 41. The peak force required increases with higher interferences, but all require about the same median force.

2. Holding Strength Sample Set 2

a. *Setup*

Setup is identical to our preliminary testing using the Instron 8500 tensile machine load cell as depicted in Figure 20. The speed of separation was sped up from 0.0021 mm/s to 0.016 mm/s for this test.

b. *Data*

Table 11 adds the peak separation force and the separation force needed after 2 mm of travel to Table 10.

Sample	NiTi SMA Avg Outer Diameter (mm) d2o	Avg Outer Diameter (in) d2o	Height (mm)	Bushing Avg Inner Diameter (mm) d1i	Avg Inner Diameter (in)	Interference (mm)	Interference (in)	Peak force press-fit(lbs)	Median force press-fit(lbs)	Peak force press-fit(N)	Median force press-fit(N)	Peak force sep. (lbs)	At 2mm Seperation force(lbs)*	Peak force sep. (N)	At 2mm Seperation force(N)*
1	5.282	0.2079	2	5.072	0.1997	0.209	0.0082	169.8	19.5	755.5	86.8	114.2	55.1	508.0	245.0
3	5.285	0.2081	2	5.116	0.2014	0.170	0.0067	189.4	41.3	842.6	183.7	100.3	46.1	446.0	205.0
4	5.286	0.2081	2	5.118	0.2015	0.168	0.0066	82.8	61.8	368.4	274.8	80.3	59.6	357.0	265.0
5	5.290	0.2083	2	5.138	0.2023	0.151	0.0060	145.0	39.0	645.2	173.3	70.6	40.2	314.0	179.0
6	5.292	0.2084	2	5.156	0.2030	0.136	0.0054	149.3	46.7	664.2	207.6	102.7	51.7	457.0	230.0
7	5.293	0.2084	2	5.151	0.2028	0.142	0.0056	112.5	44.4	500.3	197.6	69.5	64.7	309.0	288.0
8	5.293	0.2084	2	5.149	0.2027	0.144	0.0057	139.2	36.9	619.4	164.3	50.4	45.0	224.0	200.0

Table 11.   Sample Set 2 Separation Data

Figure 42 is a plot representing the peak force and the force required after 2 mm of travel vs. interferences for each sample in this set.
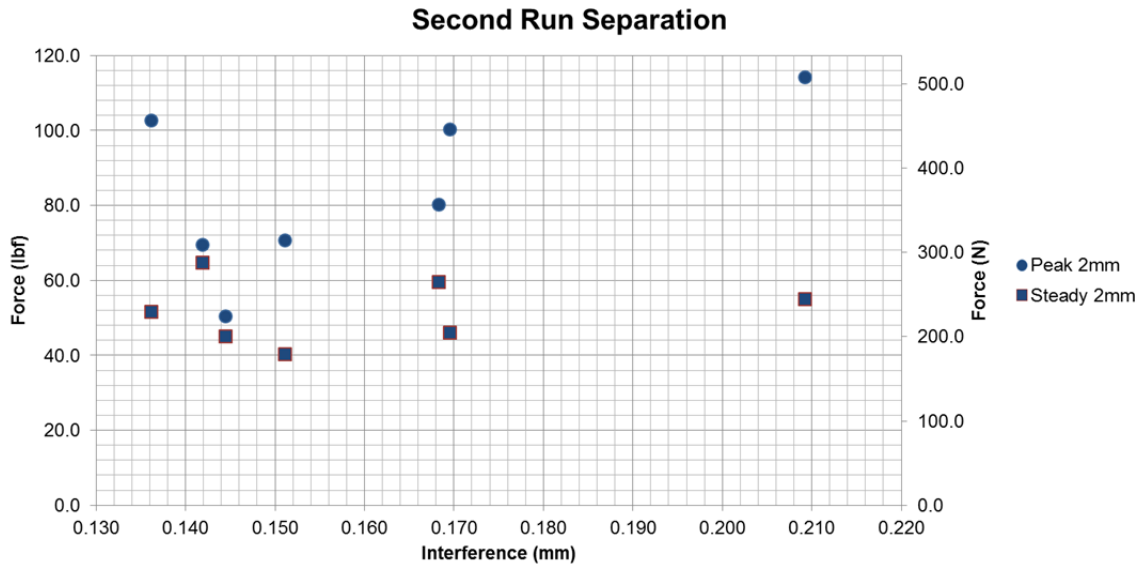
Figure 42.   Sample Set 2 Separation Data

c.   *Analysis*

All samples exhibited holding forces above the desired 135 N (30 lbf). There is a slight correlation between increasing the interference and achieving higher holding force, as expected using Equations 1.2 and 1.8. The case-hardened-steel-bushings (samples 8 and 9) exhibited slightly more holding strength compared with their AL 7075-T6 counterparts. This too is expected using Equations 1.2 and 1.8, with the AL 7075-T6 having a lower modulus of elasticity.

Due to initial galling, the new interference objective for the third sample set is 0.120 mm +/- 0.02 mm (0.0047 in +/ 0.00079 in). It is thought that this will prevent galling of the Al 7075-T6 bushing due to lower interference. However, after conducting sample set 3 the galling is determined to be caused by using the inadequate smaller press, not the high interferences used during sample set 2.

The peak press-fit force was greater than the peak separation force in each of the samples in this set. The opposite was true for sample set 1 when case-hardened-steel-bushing was used vice the AL 7075-T6 bushing. AL 7075-

56

T6 is softer than case-hardened steel. The AL 7075-T6 bushings' inner diameter slightly expanded during the press-fitting process. This reduces the interference joint leading to the decreased holding force.

3.   Press-Fit Sample Set 3

a.   Set Up

For sample set 3, twenty new AL 7075-T6 bushings were machined with inner diameter ranges of 5.121 mm – 5.197 mm (0.2016 in – 0.2046 in). This range was chosen to have an interference of 0.12 mm +/ 0.02 mm (0.0047 in +/ 0.00079 in) as mentioned above. The five previous Al 7075-T6 bushings and matching NiTi rings were used again (samples 1,3–6). These samples are reused to study the holding forces using the same samples a second time. The case-hardened-steel-bushings are not used (samples 7,8) at this time as they exhibited roughly the same holding strength as their Al 7075-T6 counterparts. Press-fitting was conducted using the same press during the design phase (larger press with bigger teeth).

Each 2 mm length NiTi ring used during sample set 3 (samples 9–28) was a new, unused sample. Measurements are taken and paired with the bushings the same way as sample set 2 (smallest SMA outer diameter with smallest AL 7075-T6 bushing inner diameter).

b.   Data

Table 12 lists sample set 3's measurements before press-fitting and the recoded peak and median force required to press-fit the SMA rings into the AL 7075-T6 bushings

Sample	NiTi SMA			Bushing		Interference (mm)	Interference (in)	Peak force press-fit(lbs)	Median force press-fit(lbs)	Peak force press-fit(N)	Median force press-fit(N)
	Avg Outer Diameter (mm) d2o	Avg Outer Diameter (in) d2o	Height (mm)	Avg Inner Diameter (mm) d1i	Avg Inner Diameter (in)						
1	5.133	0.2021	2	5.072	0.1997	0.061	0.002	127.5	59.2	567.3	263.5
3	5.160	0.2031	2	5.108	0.2011	0.052	0.002	111.2	52.3	494.6	232.8
4	5.167	0.2034	2	5.116	0.2014	0.051	0.002	72.0	39.4	320.2	175.4
5	5.192	0.2044	2	5.141	0.2024	0.051	0.002	77.4	60.4	344.2	268.5
6	5.205	0.2049	2	5.159	0.2031	0.047	0.002	56.7	36.3	252.0	161.3
9	5.290	0.2083	2	5.197	0.2046	0.093	0.004	7.8	3.0	34.6	13.6
10	5.288	0.2082	2	5.197	0.2046	0.091	0.004	31.4	13.9	139.7	61.9
11	5.287	0.2082	2	5.189	0.2043	0.098	0.004	40.2	9.9	178.9	44.2
12	5.286	0.2081	2	5.171	0.2036	0.115	0.005	82.4	44.5	366.4	198.0
13	5.286	0.2081	2	5.171	0.2036	0.115	0.005	121.0	51.7	538.4	230.1
14	5.286	0.2081	2	5.169	0.2035	0.117	0.005	121.4	92.7	540.0	412.4
15	5.285	0.2081	2	5.166	0.2034	0.118	0.005	164.7	98.0	732.7	435.9
16	5.281	0.2079	2	5.166	0.2034	0.115	0.005	122.0	85.0	542.7	377.9
17	5.279	0.2078	2	5.166	0.2034	0.112	0.004	108.3	82.0	481.7	364.9
18	5.278	0.2078	2	5.166	0.2034	0.112	0.004	120.9	86.5	538.0	384.9
19	5.278	0.2078	2	5.164	0.2033	0.114	0.005	134.1	89.2	596.6	396.7
20	5.278	0.2078	2	5.161	0.2032	0.117	0.005	122.1	47.3	543.1	210.4
21	5.277	0.2078	2	5.156	0.203	0.121	0.005	94.7	57.3	421.4	255.1
22	5.277	0.2078	2	5.156	0.203	0.121	0.005	103.8	60.1	461.9	267.5
23	5.277	0.2078	2	5.149	0.2027	0.128	0.005	85.5	65.7	380.1	292.1
24	5.277	0.2078	2	5.149	0.2027	0.128	0.005	100.7	81.6	448.0	362.8
25	5.276	0.2077	2	5.149	0.2027	0.128	0.005	99.6	76.7	443.1	341.1
26	5.274	0.2077	2	5.144	0.2025	0.131	0.005	138.9	55.2	617.7	245.3
27	5.274	0.2076	2	5.136	0.2022	0.138	0.005	131.0	77.7	582.7	345.6
28	5.274	0.2076	2	5.121	0.2016	0.153	0.006	148.4	45.7	660.2	203.3

Table 12.   Sample Set 3 Press-Fit Data

Figure 43 is a plot of both peak force and median force required to press-fit vs. interference for each sample.
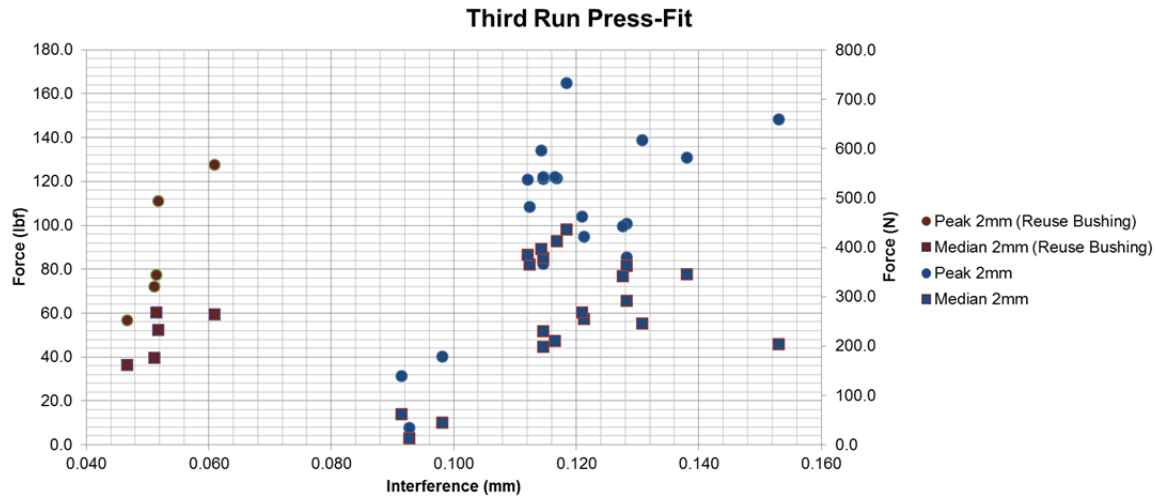
Figure 43.   Sample Set 3 Press-Fit Data

c.   *Analysis*

Again, there is a direct correlation between the interference and force required during press-fitting. The higher the interference, the higher the force required to press-fit. Here the reused bushings and NiTis require less force the second time around (compared with sample set 2). The NiTi rings for the reused samples exhibit a reduction of size due to the stress placed on them during the initial press-fit and separation.

4.   **Holding Strength Sample Set 3**

a.   *Set Up*

Press-fitting the third sample set was conducted in the same fashion as before, but uses the original press from the design phase. Using the larger press allows for a smooth press-fit without galling effects. The tradeoff is having fewer data points from the load cell during press-fitting.

b.   *Data*

Table 13 adds to Table 12 the peak separation force and the separation force needed after 2 mm of travel.

59

| | NiTi SMA | | | Bushing | | | | | | | | | At 2mm | | At 2mm |
Sample	Avg Outer Diameter (mm) d2o	Avg Outer Diameter (in) d2o	Heig ht (mm)	Avg Inner Diamet er (mm) d1i	Avg Inner Diamet er (in)	Interfer ence (mm)	Interfer ence (in)	Peak force press-fit(lbs)	Media n force press-fit(lbs)	Peak force press-fit(N)	Median force press-fit(N)	Peak force sep. (lbs)	Sepera tion frce(lbs)*	Peak force sep. (N)	Sepera tion force(N)*
1	5.133	0.2021	2	5.072	0.1997	0.061	0.002	127.5	59.2	567.3	263.5	120.0	33.7	533.8	150.0
3	5.160	0.2031	2	5.108	0.2011	0.052	0.002	111.2	52.3	494.6	232.8	106.6	49.0	474.3	217.8
4	5.167	0.2034	2	5.116	0.2014	0.051	0.002	72.0	39.4	320.2	175.4	77.4	47.1	344.3	209.6
5	5.192	0.2044	2	5.141	0.2024	0.051	0.002	77.4	60.4	344.2	268.5	84.7	31.0	376.8	138.0
6	5.205	0.2049	2	5.159	0.2031	0.047	0.002	56.7	36.3	252.0	161.3	60.0	36.8	266.8	163.8
9	5.290	0.2083	2	5.197	0.2046	0.093	0.004	7.8	3.0	34.6	13.6	6.8	0.0	30.3	
10	5.288	0.2082	2	5.197	0.2046	0.091	0.004	31.4	13.9	139.7	61.9	20.3	16.6	90.1	73.9
11	5.287	0.2082	2	5.189	0.2043	0.098	0.004	40.2	9.9	178.9	44.2	26.0	1.3	115.6	5.8
12	5.286	0.2081	2	5.171	0.2036	0.115	0.005	82.4	44.5	366.4	198.0	68.6	42.6	305.3	189.6
13	5.286	0.2081	2	5.171	0.2036	0.115	0.005	121.0	51.7	538.4	230.1	98.0	63.0	436.0	280.4
14	5.286	0.2081	2	5.169	0.2035	0.117	0.005	121.4	92.7	540.0	412.4	105.5	30.4	469.1	135.4
15	5.285	0.2081	2	5.166	0.2034	0.118	0.005	164.7	98.0	732.7	435.9	83.3	47.1	370.6	209.7
16	5.281	0.2079	2	5.166	0.2034	0.115	0.005	122.0	85.0	542.7	377.9	86.4	39.9	384.5	177.7
17	5.279	0.2078	2	5.166	0.2034	0.112	0.004	108.3	82.0	481.7	364.9	85.4	40.4	379.9	179.8
18	5.278	0.2078	2	5.166	0.2034	0.112	0.004	120.9	86.5	538.0	384.9	106.6	48.3	474.1	214.9
19	5.278	0.2078	2	5.164	0.2033	0.114	0.005	134.1	89.2	596.6	396.7	80.6	40.4	358.6	179.7
20	5.278	0.2078	2	5.161	0.2032	0.117	0.005	122.1	47.3	543.1	210.4	64.8	39.9	288.1	177.3
21	5.277	0.2078	2	5.156	0.203	0.121	0.005	94.7	57.3	421.4	255.1	99.1	45.9	440.9	204.0
22	5.277	0.2078	2	5.156	0.203	0.121	0.005	103.8	60.1	461.9	267.5	77.2	50.0	343.6	222.5
23	5.277	0.2078	2	5.149	0.2027	0.128	0.005	85.5	65.7	380.1	292.1	75.1	41.6	334.3	185.1
24	5.277	0.2078	2	5.149	0.2027	0.128	0.005	100.7	81.6	448.0	362.8	153.8	61.7	684.0	274.3
25	5.276	0.2077	2	5.149	0.2027	0.128	0.005	99.6	76.7	443.1	341.1	108.8	54.2	484.0	241.2
26	5.274	0.2077	2	5.144	0.2025	0.131	0.005	138.9	55.2	617.7	245.3	56.6	48.4	251.8	215.4
27	5.274	0.2076	2	5.136	0.2022	0.138	0.005	131.0	77.7	582.7	345.6	100.3	42.3	446.3	188.3
28	5.274	0.2076	2	5.121	0.2016	0.153	0.006	148.4	45.7	660.2	203.3	88.6	58.4	394.3	259.7

Table 13.   Sample Set 3 Separation Data

Figure 44 plots the peak separation force and the force required after 2 mm of travel vs. interference for each sample in sample set 3.
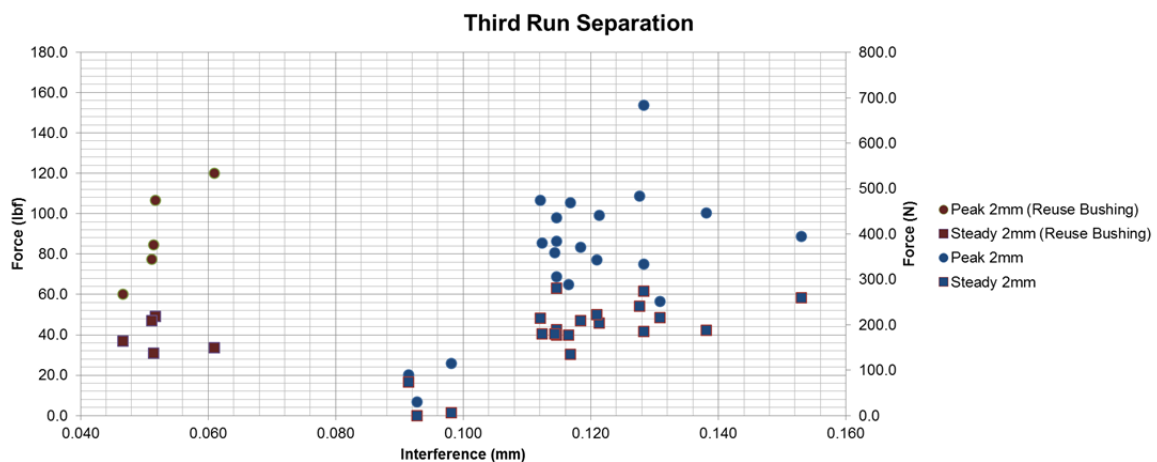

Figure 44.   Sample Set 3 Separation Data

c. Analysis

The reused samples (1,3–6) exhibited a reduction in holding force. This was due to the decrease in interference. Additionally, the reused Al 7075-T6 bushings and NiTi have already undergone stress causing the inner diameter of the bushing to slightly expand and the NiTi ring to slightly contract. The remaining new samples perform well with holding strength above the desired 135 N (30 lbf), with the exception of samples 9–11. These three samples have an interference that is too small. The press-fitting of these three samples, as shown in Table 12 and Figure 43, required very little force. As with sample set 2, there is a correlation between the required force needed during press-fitting and the force required to separate the NiTi rings from the AL 7075-T6 bushings.

Upon further review (after sample set 3 separation), the inner diameter of the top and bottom entrances differ by as much as +/- 0.018 mm (+/- 0.007 in). Additionally, inserting the gauge pins from one end resulted in obstruction, vice having a smooth and straight barrel. Further changes in manufacturing procedures (such as drilling/lathing from one end all the way through vice drilling/lathing from both ends) will ensure more evenness in the barrel.

As in sample set 2, the peak press-fit force was greater than the peak separation force for the new unused samples in this set (samples 9 – 28). Samples 1 – 6 (the reused AL 7075-T6 bushings from sample set 2) had similar peak press-fit and peak separation peak forces. The inner diameter for samples 1 – 6 in this sample set did not increase as previously occurred during sample set 2.

B. RELEASABILITY

1. Thermal Release Sample Set 1

a. *Set Up*

For the first thermal test, the AL 7075-T6 bushings and NiTi rings were reused from sample set 3. Reusing the NiTi rings vice using new NiTi rings for the first thermal release sample set was done to conserve the limited number of new NiTi rings available for this thesis. The AL 7075-T6 bushings from the conclusion of sample set 3 separation was separated by the inner diameter size (smallest to largest). The NiTi rings used after sample set 3 separation testing (not fresh unused NiTi ring samples) were measured and then matched to the six AL 7075-T6 bushings selected to have an interference between 0.1 mm–0.133 mm (0.004 in–0.0053 in).

The six samples were press-fitted in the same manner as sample set 3, and then assembled as listed in Appendix B. Once assembled, resistance measurements of the Nichrome wire were conducted using a CEN-TECH P35017 multimeter. Additional resistance measurements of the wires leading to the Gwinstek GPS 4303 power supply and the total resistance between the power supply and the connected sample are recorded in Table 14. This is done to verify that there is no short between the power supply and the tested sample.

Two thermal leads were used. Ideal locations to take thermal readings are on the NiTi ring, on the AL 7075-T6 bushing, and on the Nichrome wire. Placing a thermal lead on the NiTi ring will partially secure the ring in the bushing, disrupting the release experiment. For this reason no thermal lead was placed on the NiTi ring.

The first lead was used to measure the temperature of the Nichrome wire on top of the EDU. The second lead was used to measure a contact point on the bottom of the AL 7075-T6 bushing and on top of the PC washer (Figure 45). Measurements were taken using the OMEGA HH147U data logger thermometer and stored in the computer for analysis.
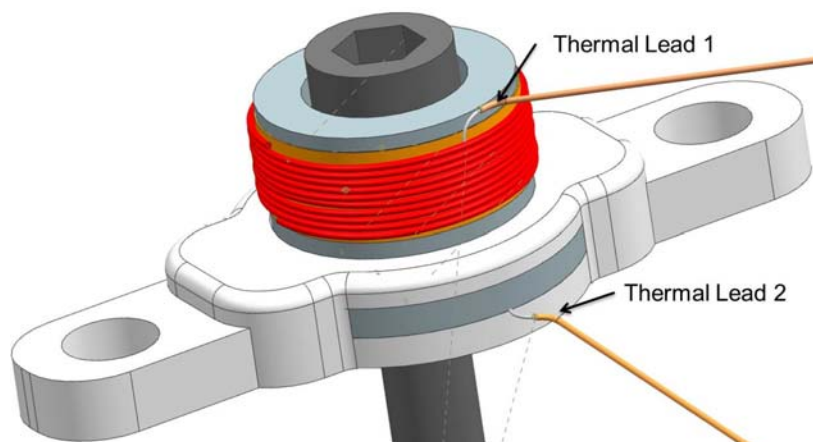
Figure 45.   EDU With Thermal Leads

After securing the sample to the stand in the vacuum chamber and securing the thermal leads, the power leads were connected to the Nichrome wire, the glass cylinder was placed over the setup (Figure 4**Error! Reference source not found.**6) and the air was pumped out to 26.5 in-Hg (89740 Pa). The power supply was set not to exceed 3.5 volt and 1.0 amps per set design constraints. With the timer started, the power supply was turned on and the temperatures were recorded.
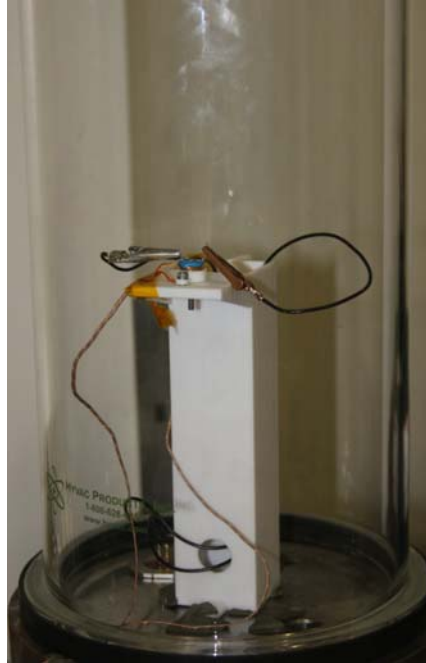
Figure 46.   Thermal Release In Vacuum

b.   Data

Measurements of the six samples were taken before press-fitting. The samples where assembled and had further measurements (Nichrome wire resistance after sample assembly to the EDU and resistance measurements of the entire test bed) were taken. The peak temperature and time required to disengage the NiTi ring from the bushing is also listed in Table 14.

| | NiTi SMA | | | Bushing | | | | | | | | | | | | | |
Sample	Avg Outer Diameter (mm) d2o	Avg Outer Diameter (in) d2o	Height (mm)	Avg Inner Diameter From Top (mm) d1i	Avg Inner Diameter From Bottom (mm) d1i	Avg Inner Diameter From Top (in)	Avg Inner Diameter From Bottom (in)	Interference (mm)	Interference (in)	Actuation Time (s)	Peak Temperature (C)	Peak Temperature (F)	Equipment resistance (ohms)	Device resistance (ohms)	Total testbed resistance (ohms)	Amps	Volts	Vacuume (in-Hg)
1	5.226	0.2058	2	5.116	5.116	0.2014	0.2014	0.111	0.0044	128	122	251.6	0.65	5.15	5.25	0.66	3.1	26.5
2	5.231	0.2060	2	5.118	5.118	0.2015	0.2015	0.113	0.0045	100	112	233.6	0.65	5.35	5.55	0.73	3.5	26.5
3	5.223	0.2056	2	5.141	5.123	0.2024	0.2017	0.100	0.0039									
4	5.269	0.2074	2	5.146	5.149	0.2026	0.2027	0.120	0.0047	96	118	244.4	0.65	5.15	5.3	0.72	3.4	26.5
5	5.282	0.2080	2	5.149	5.149	0.2027	0.2027	0.133	0.0053	78	107	224.6	0.65	5.15	5.25	0.72	3.4	27
6	5.283	0.2080	2	5.146	5.154	0.2026	0.2029	0.130	0.0051	91	106	222.8	0.65	5.25	5.45	0.72	3.5	27

Table 14.   First Thermal Release

Figure 47 is the graphical representation of the time and temperature recordings for each sample.
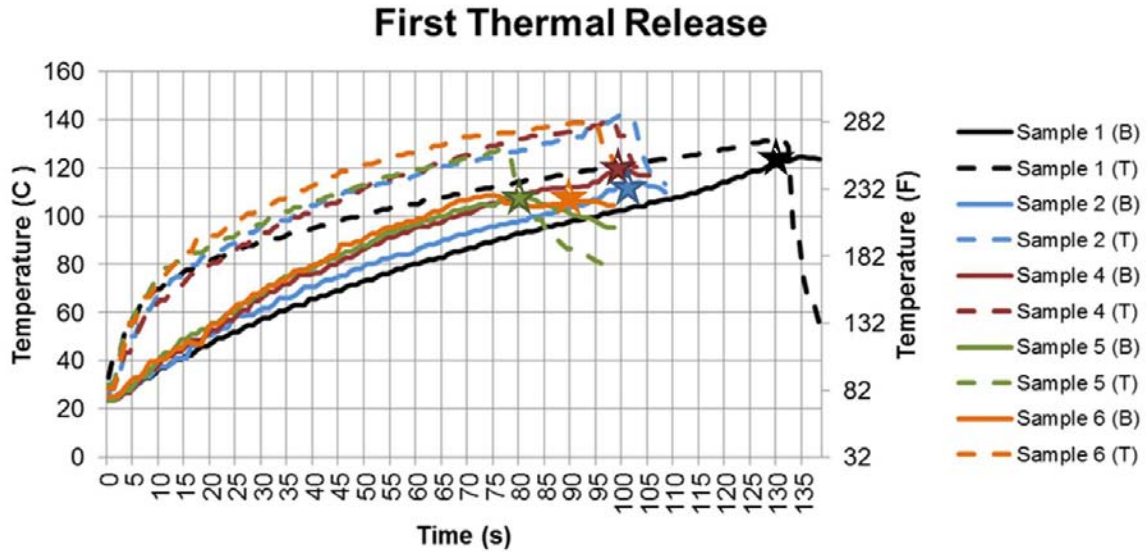

Figure 47.   First Thermal Release

Figure 48 is a graphical representation of the temperature difference data between the two ends of the bushing. One end had the Nichrome wire wrapped around the bushing, while the other end was resting on the PC washer.
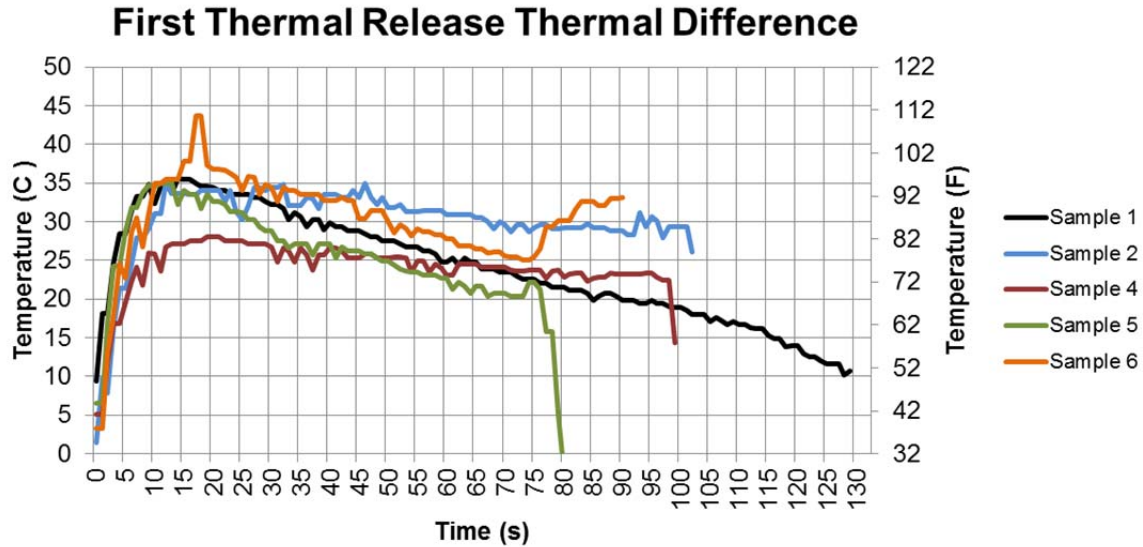
Figure 48.   Thermal Difference between the Two Leads for the First Set

c.   Analysis

Each sample successfully released with the exception of sample 3. A washer between the head of the retaining bolt and the NiTi ring was inserted to isolate any thermal transfer during actuation and calculate any beneficial effects. Unfortunately, the washer chosen was not adequate to withstand high temperatures and melted to the AL 7075-T6 bushing. This prevented the retaining bolt and the NiTi ring from completely releasing.

The bottom of the AL 7075-T6 bushing lagged up to around 35°C (95°F) from the Nichrome wire. Over time, the Al 7075-T6 bushings temperature difference gradually decreased after the initial peak.

There is a correlation between the amount of current and the release time for each sample. The higher current leads to more heat and quicker release. Due to successful results, a second set of tests was conducted using new unused NiTi rings.

2. Thermal Release Sample Set 2

a. Set Up

The AL 7075-T6 bushings from the conclusion of sample set 3 separation were ranked by how straight the barrels are (least amount of difference between the top and bottom entrance inner diameters), followed by the inner diameter size. Six samples were chosen for the straightness and smallest inner diameter. New NiTi rings were measured and paired with the six selected AL 7075-T6 bushings to have an interference of 0.1 mm – 0.13 mm (0.004 in – 0.005 in). One additional sample (sample 7) was used from sample 5 during vibration testing (next section below). This sample successfully passed vibration testing and was used to determine its release ability after vibration testing. All other steps used in the previous thermal release set up were followed in this thermal release set.

b. Data

Table 15 lists the same information as Table 14, but for thermal release sample set 2.

| Sample | NiTi SMA | | | | Bushing | | | Interference (mm) | Interference (in) | Actuation Time (s) | Peak Temperature (C) | Peak Temperature (F) | Equipment resistance (ohms) | Device resistance (ohms) | Total testbed resistance (ohms) | Amps | Volts | Vacume (in-Hg) |
	Avg Outer Diameter (mm) d2o	Avg Outer Diameter (in) d2o	Height (mm)	Avg Inner Diameter From Top (mm) d1i	Avg Inner Diameter From Bottom (mm) d1i	Avg Inner Diameter From Top (in)	Avg Inner Diameter From Bottom (in)											
1	5.260	0.2071	2	5.151	5.126	0.2028	0.2018	0.134	0.0053	84	106	222.8	0.977	5.4	5.9	0.73	3.5	26
2	5.271	0.2075	2	5.164	5.144	0.2033	0.2025	0.127	0.0050	82	107	224.6	0.973	5.55	5.6	0.73	3.5	26.5
3	5.272	0.2076	2	5.146	5.164	0.2026	0.2033	0.108	0.0043	89	115	239	0.973	5.2	5.5	0.73	3.7	26.5
4	5.282	0.2079	2	5.171	5.177	0.2036	0.2038	0.105	0.0041	79	87.1	188.8	0.973	5.8	5.75	0.73	3.4	26.5
5	5.286	0.2081	2	5.174	5.174	0.2037	0.2037	0.112	0.0044	42	106	222.8	0.973	5.25	5.4	0.96	4.9	26.5
6	5.287	0.2082	2	5.171	5.179	0.2036	0.2039	0.108	0.0043	93	89	192.2	0.973	5.2	5.3	0.73	3.5	26.5
7	5.266	0.2073	2	5.146	5.149	0.2026	0.2027	0.120	0.0047	85	99	210.2	0.973	5.1	5.3	0.73	3.6	26.5

Table 15.   Second Thermal Release

Figure 49 is the graphical representation of the time and temperature recordings for each sample in this set.
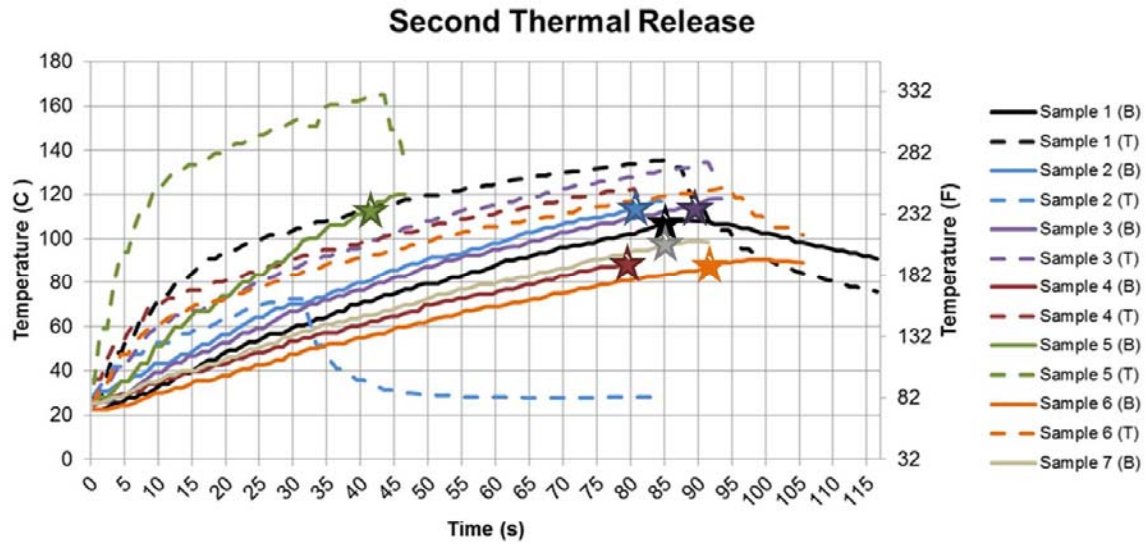
Figure 49.   Second Thermal Release

Figure 50 is a graphical representation of the temperature difference data between the two ends of the bushing. One end had the Nichrome wire wrapped around the bushing, while the other end was resting on the PC washer.
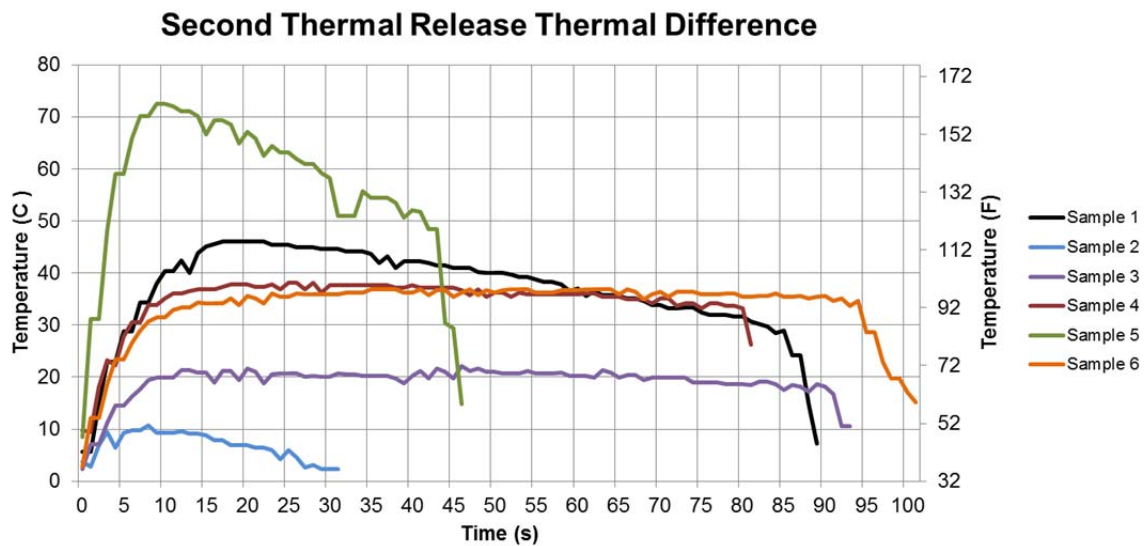

Figure 50.   Thermal Difference between the Two Leads for the First Set

c.   Analysis

Each sample successfully deployed upon activation. Using 3.5 volt and 0.73 amps (2.55 watt), the activation times ranged between 79 and 93 seconds. The previously vibrated sample (sample 7 in this set) successfully deployed. This verified that a successful deployment was achieved after vibration testing (simulating launch conditions).

When the power was increased to 4.9 volt and 0.96 amps (4.704 watt), actuation time decreases to 42 seconds. But in increasing the power, the thermal difference between the Nichrome wire and the AL 7075-T6 bushing was greater than the lower power samples (Figure 50). The Nichrome wire also peaked at a higher temperature of 165°C (329°F), compared to 135°C (275°F) (Figure 49).

Vibration In determining the frequency and level for vibrational testing, data from NPSCuL (Table 16) was used. NPSCuL (Figure 51) is a Naval Postgraduate School project used as a CubeSat launcher.
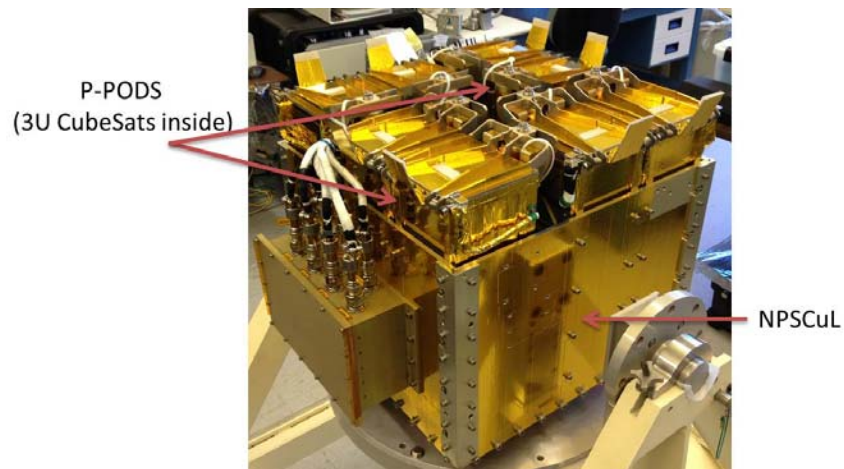
Figure 51.   NPSCuL With Eight P-PODS in the Secured Configuration. From [18]

The NPSCuL is able to carry and deploy a combination of various sizes of CubeSats into orbit as a secondary payload on a rocket. Once in orbit, the NPSCuL opens each P-POD door sequentially, thereby releasing the CubeSats

in that P-POD. NPSCuL launched on NRO L-36 on September 13, 2012, releasing eleven CubeSats.

NPSCuL was vibration tested using inputs to the base from worst case Atlas V launch vehicle Max Predicted Environment (MPE) spectrum. Acceptance testing of NPSCuL was further conducted in February 2012. The measured responses at the NPSCuL to P-POD interference were measured during the test. This data was then scaled and enveloped by 6 dB to arrive at the qualification vibration testing[3].

X-Axis			
Freq, Hz	ASD, g^2/Hz		
	Acceptance	Protoqual	Qual
20	0.03	0.06	0.12
45	3.15	6.3	12.6
55	3.15	6.3	12.6
80	0.17	0.35	0.70
150	0.17	0.35	0.70
180	0.05	0.1	0.2
380	0.05	0.1	0.2
450	0.12	0.24	0.48
1200	0.12	0.24	0.48
2000	0.01	0.02	0.04
Overall Grms	15.1	21.4	30.3

Y-Axis			
Freq, Hz	ASD, g^2/Hz		
	GEMSat Acceptance	GEMSat Protoqual	Qual
20	0.05	0.10	0.20
45	1.80	3.60	7.20
55	1.80	3.60	7.20
80	0.23	0.46	0.92
120	0.23	0.46	0.92
130	0.10	0.20	0.40
200	0.10	0.20	0.40
300	0.19	0.37	0.75
400	0.19	0.37	0.75
600	0.09	0.18	0.36
2000	0.09	0.18	0.36
Overall Grms	15.9	22.5	31.8

Z-Axis			
Freq, Hz	ASD, g^2/Hz		
	Acceptance	Protoqual	Qual
20	0.04	0.08	0.16
45	0.30	0.60	1.20
130	0.30	0.60	1.20
155	0.09	0.18	0.36
220	0.09	0.18	0.36
240	0.14	0.28	0.56
300	0.14	0.28	0.56
400	0.05	0.10	0.20
1000	0.05	0.10	0.20
1100	0.02	0.04	0.08
2000	0.02	0.04	0.08
Overall Grms	10.5	14.8	21.0

Table 16.   NPSCuL Vibration Testing Data. From [19]

The EDU was designed to secure the deployable structure along its axis (Z-axis). The intent of the EDU was to take advantage of the deployable hinge to secure/restrict any movement along the other two axes (X and Y axis). The author not only tested the EDU's ability to withstand vibrational loads along the Z-axis, but also tested the limits along the Y-axis during vibration (because of symmetry along X and Y-axis, X-axis testing was not conducted). Furthermore, the author used an unrestrained X and Y axis setup for the mass for additional

---

[3] Qualification level testing is the most demanding testing conducted throughout the spacecraft testing levels. Testing intensity levels begin at the Acceptance test, followed by a 3dB increase for the proto-qualification testing, and a 6dB increase from acceptance testing level to reach the qualification testing.

worst case scenarios (if the solar panel was not supported at the opposite end), and to test in the Y axis.

3. Setup

The X-Axis vibration levels from Table 16 were used to create the testing environment for the EDU vibration test along the Z-axis. The X-Axis data has the highest Qual levels of all three tests, allowing the EDU to be tested using worst case scenario data. Figure 52 is a picture of the components used for vibration testing.

Figure 52.   Vibration Testing Components

The orientation used for the vibration testing is shown in Figure 53.
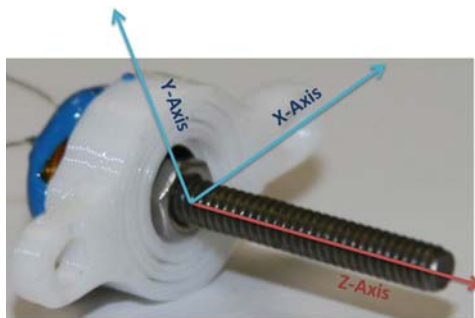
Figure 53.   Reference Axis for Vibration Testing

As mentioned above, the mass of the 3U solar panel is 110 g (+/- 5 g), including the weight of all the panel hardware such as the hinge and spring. The

effective mass of the solar panel at the tip is less than the entire mass due to the solar panel's opposite supported end. The author chose to add a factor of safety and ignored the fact that the solar panel is supported at the opposite end, therefore assuming a worst case mass of 116 g. A 116 g (0.26 lb) machined solid brass block (Figure 52) was used to simulate the mass of the solar panel. The mass was secured to each sample under a pre-load measured using a torque wrench. Having a measured pre-load allows for the additional analysis between the vibrational performance of the EDU and the amount of pre-load between the NiTi ring and the brass mass on each EDU sample (listed in Table 17). Establishing the pre-load also serves as a way to estimate the samples' static holding force without having to extract the entire NiTi ring from the AL 7075-T6 bushing. Additional information in setting pre-load for each sample is listed in Appendix E.

A single axis accelerometer was attached to the same block as the EDU to serve as the control signal during vibration testing. A three axis accelerometer was attached to the brass mass to record the vibration effects. The test bed vibrated in an up and down orientation. Testing in the Z-axis configuration is depicted in Figure 54, and testing in the Y-axis is depicted in Figure 55. Further detailed setup procedures are listed in Appendix E.
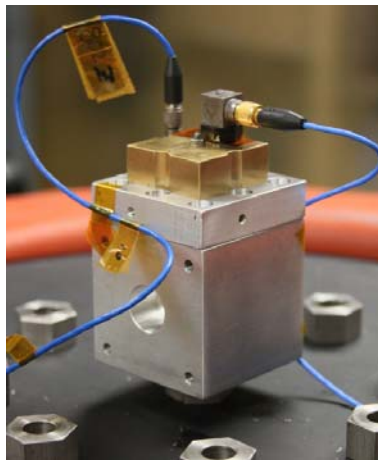
Figure 54.   Vibration Testing in the Z-Axis

72
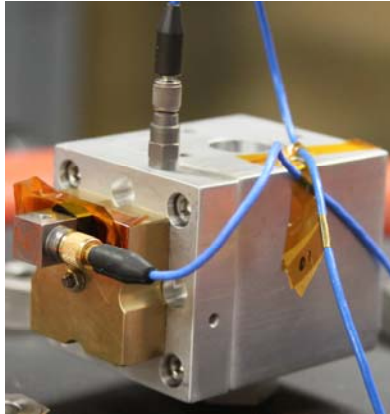
Figure 55.   Vibration Testing in the Y-Axis

The X-axis frequency and acceptance levels from Table 16 are used for the random vibration test bed with the following levels and durations (in minute:second format).

Level 1   -15 dB   0:00:30

Level 2   -12 dB   0:00:30

Level 3   -9 dB   0:00:30

Level 4   -6 dB   0:00:30

Level 5   -3 dB   0:00:30

Level 6   0 dB   0:03:00

Guidance from the Military Handbook 340A was taken when programing the vibration test bed. This includes conducting random vibrations to span between 20 Hz to 2,000 Hz, having a 1 second time segment overlap by at least 50 percent, and a resolution no greater than 1/6 octave (but not less than 5 Hz) [20]. Additionally, a sinusoidal vibration sweep (once from 20 Hz to 2,000 Hz, then back from 2,000 Hz to 20 Hz) was conducted before and after the random vibration testing. This sinusoidal vibration sweep was used to analyze the samples natural frequencies, and was used to determine if any changes/movement of the mass in relation to the EDU occurred due to the random vibration testing.

73

4. Data

Table 17 lists each samples measurements prior to being press-fit, the force required to press-fit, the amount of pre-load on the retaining bolt against the SMA, and the outcome form vibration testing. The values representing the vibration testing are successful tested levels.

	NiTi			Bushing												
Sample	Avg Outer Diameter (mm) d2o	Avg Outer Diameter (in) d2o	Height (mm)	Avg Inner Diameter From Top (mm) d1i	Avg Inner Diameter From Bottom (mm) d1i	Avg Inner Diameter From Top (in)	Avg Inner Diameter From Bottom (in)	Interference (mm)	Interference (in)	Peak force press-fit(lbs)	Median force press-fit(lbs)	Peak force press-fit(N)	Median force press-fit(N)	Vibe y-axis dB passed	Vibe z-axis dB Passed	Pre-load (lb-in)	Pre-load (N-m)
1	5.284	0.2080	2	5.174	5.174	0.2037	0.204	0.110	0.0043	94.8	41.5	421.9	184.4	-9	0	1.5	0.17
2	5.282	0.2080	2	5.169	5.169	0.2035	0.204	0.113	0.0045	101.2	45.4	450.4	201.8	-	-3	1	0.11
3	5.276	0.2077	2	5.164	5.164	0.2033	0.203	0.112	0.0044	62.6	37.1	278.3	165.0	-3	0	1.1	0.12
4	5.272	0.2076	2	5.166	5.161	0.2034	0.203	0.111	0.0044	76.0	17.1	337.9	75.9	-	-3	1	0.11
5	5.266	0.2073	2	5.149	5.146	0.2027	0.203	0.120	0.0047	81.2	18.2	361.3	81.1	-6	0	1	0.11
6	5.271	0.2075	2	5.149	5.149	0.2027	0.203	0.123	0.0048	61.1	32.3	271.6	143.7	-6	0	1.9	0.21

Table 17.   Vibration Test Results Overview

Figure 56 is the sinusoidal sweep that was conducted on each sample prior to Z-axis random vibration testing. Figures 56–59 have similar axis plotting intensity (g levels) vs. frequency.
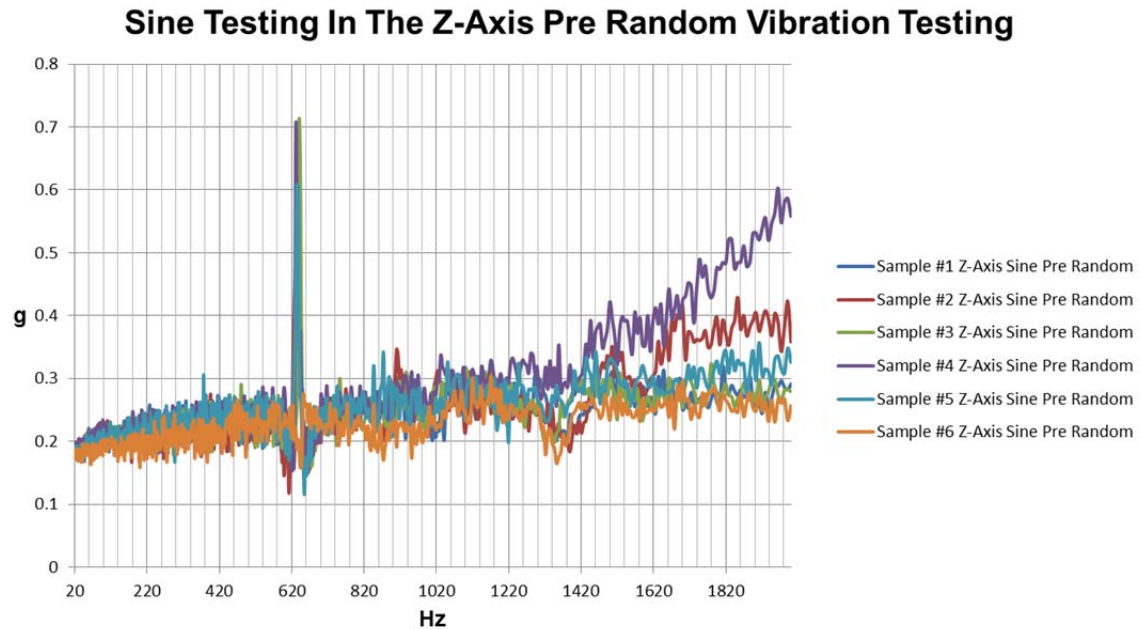
Figure 56.   Pre Z-Axis Random Vibration Sinusoidal Sweep aor All Samples

Figure 57 is the post sinusoidal sweep conducted on the samples that survived the 0 dB level random vibration test.
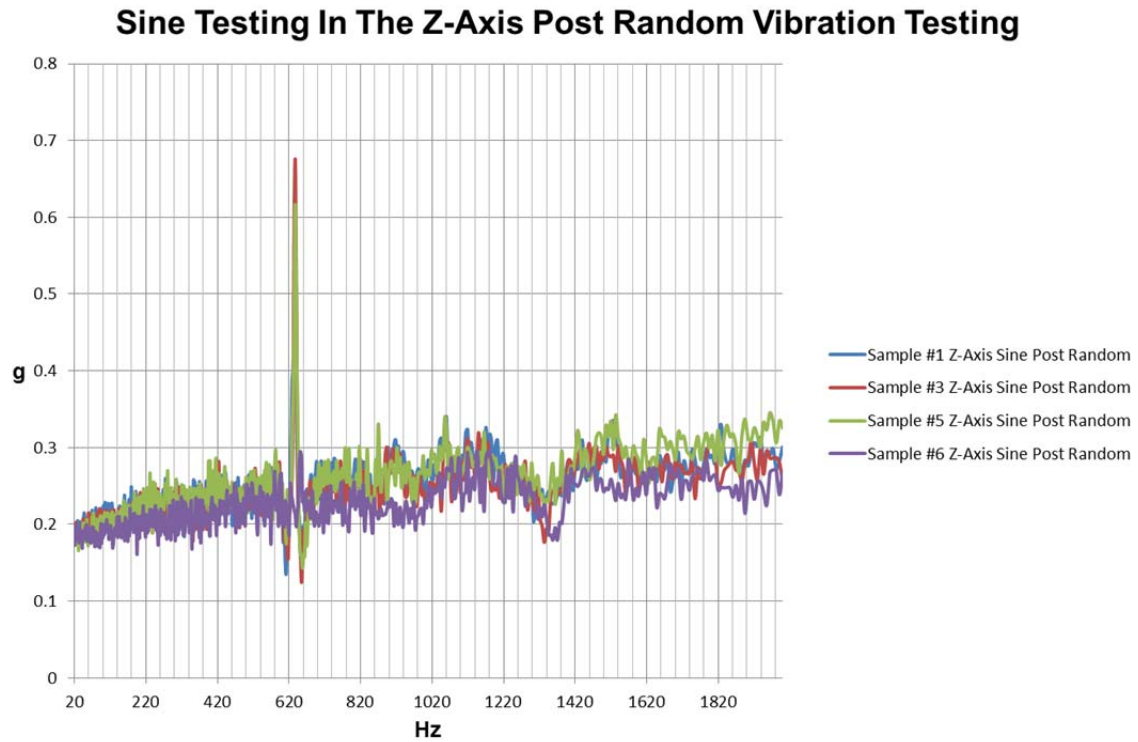
Figure 57.   Post Z-Axis Random Vibration Sinusoidal Sweep
for Samples 1, 3, 5, and 6

Figure 58 is the sinusoidal sweep conducted before the Y-axis random vibration testing.
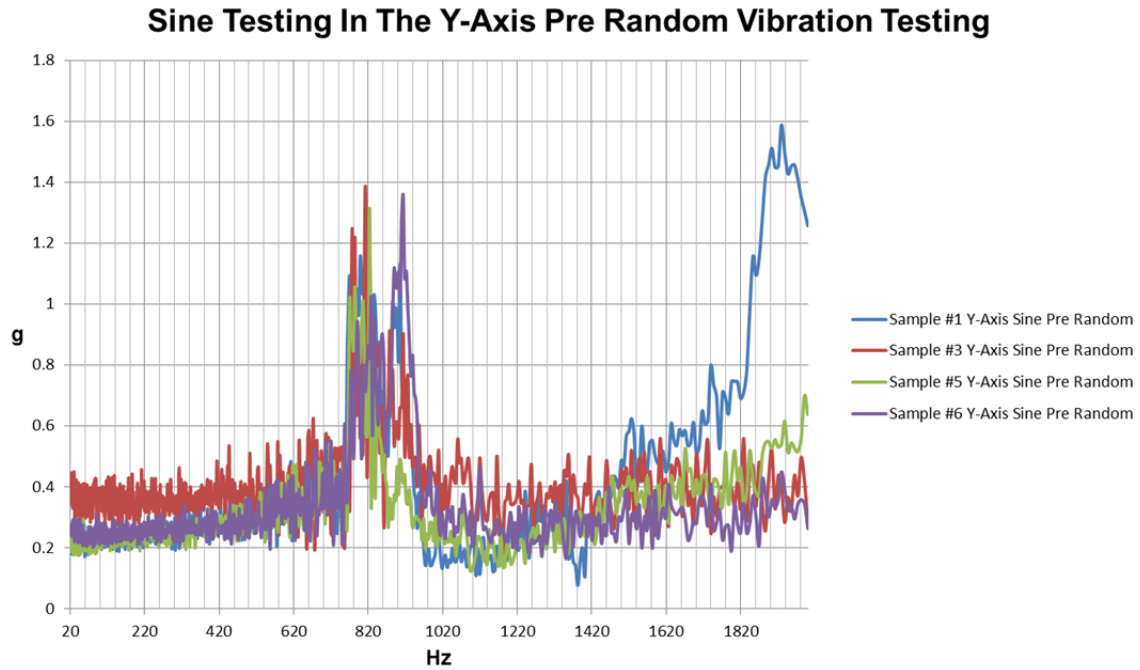
Figure 58.   Pre Y-Axis Random Vibration Sinusoidal Sweep for Samples 1, 3, and 5

Figure 59 is the sinusoidal sweep post Y-axis random vibration testing.
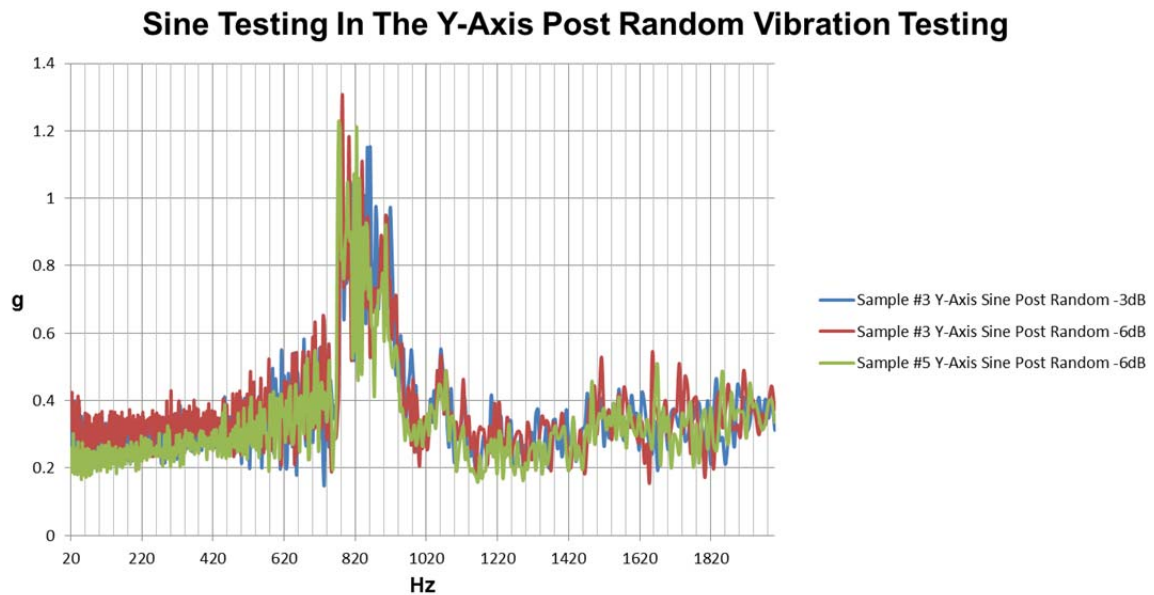
Figure 59.   Post Y-Axis Random Vibration Sinusoidal Sweep for Sample 3 and 5

Figure 60 is a plot of sample 6 when it underwent random vibration testing at 0 dB levels in the Z-axis. The red lines represent the maximum and minimum safety margins. The blue lines represent the measured response on the brass mass.

Random   **Measurement, On Mass, (+Z)**

```
Chan.no:           4
Chan.type:         M
DOF:               20
Level:             0.0 dB
Resolution:        2 Hz
Contr.strat.:      Maximum
Unit:              g²/Hz
RMS (act.):        30.57 g
RMS (req.):        30.27
Contr.strat.:      Closed loop

-- Time on act. level --
elapsed:           000:02:37
remaining:         000:00:22

-- Time total --
elapsed:           000:05:07
remaining:         000:00:22

Date:              08-06-12
Time:              10:02:01
```

W:\Thesis\Random\Sample # 6_Z_Random.rrn
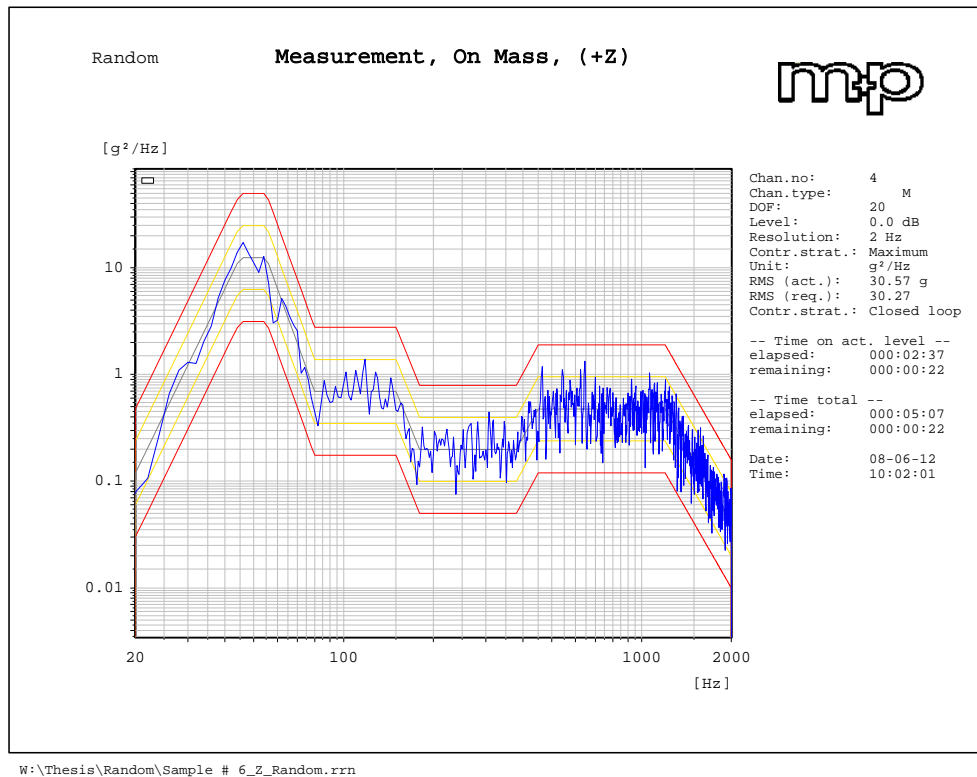
Figure 60.   Z-Axis Random Vibration on Sample 6

Additional individual random vibration and sinusoidal vibration plots are listed in Appendix F.

5.   Analysis

The Z-axis pre-random vibration testing sinusoidal sweep (Figure 56) for all six samples share a similar peak natural frequency around 650 Hz. All six samples have similar frequency responses up to 1400 Hz, with diverging responses to 2,000 Hz. This indicates a difference in each sample's physical characteristics (such as holding strength performance). Two samples failed to

reach the 0 dB (30.3 GRMS) random vibration tests (both samples broke off at -3 dB levels). Those two samples that failed are the same two samples with the diverging higher frequency responses in Figure 56 (higher g levels), validating the importance of conducting sinusoidal sweeps in order estimate a successful random vibration test. (Or successfully securing a solar panel through the vigorous vibrations caused by launching into orbit.) The post Z-axis sinusoidal (Figure 57) tests on the remaining four samples that passed the random Z-axis testing show no change from the previous sinusoidal sweep (Figure 56), indicating a solid performance from the EDU samples.

Of the six samples, four samples held the brass mass throughout the entire Z-axis random vibration test (30.3 GRMS). The other two samples held the mass up to -3 dB levels (21.4 GRMS). Those samples that passed the Z-axis random vibrations test (Samples 1,3,5,6) all had higher pre-load set compared to the other two samples (Samples 2, and 4). The increased pre-load directly correlates to the amount of holding force the sample is able to achieve.

Testing conducted in the Y-axis was used to determine the EDU's X and Y-axis limits. Those samples that passed the Z-axis random vibration testing were then tested in the Y-axis configuration (Figure 55). The samples all passed levels to -9 dB (10.74 GRMS), with the maximum passed level of -3 dB (21.4 GRMS) for sample number 3 (Table 17). The Y-axis sinusoidal sweeps for samples 1, 3, and 5 prior to Y-axis random vibration testing are shown in Figure 58. Sample 5 was not tested to 0 dB levels, but taken to -6 dB levels and stopped to ensure a vibrated sample for thermal release testing. The other samples (1, 3, and 6) were all set to random vibration test level of 0 dB, and the test was only terminated after failure. This was done to determine the Y-axis random vibration test limits and to determine any correlation between the sinusoidal sweep and random vibration limits as found during Z-axis testing.

The peak natural frequencies found in Figure 58 have a broader range (compared to the nice narrow range) and greater g levels than those seen in Figure 56 indicating movement of the brass mass. Sample 1 has the highest g

response with higher frequencies above 1600 Hz, and failed with random vibration levels above -9 dB. Sample 3 was randomly vibrated three times to levels up to -6 dB, -3 db, and 0 dB with failure at 0 dB. Sample 5 was randomly vibrated to level -6 dB for reasons mentioned above. The Y-axis sinusoidal sweep g levels at 2,000 Hz results have a direct correlation to holding strength in the Y-axis during random vibration testing (just as in the Z-axis tests).Sample 1 had the highest g level at 2,000 Hz, and also failed the random vibration test at the lowest level of -9 dB.

Frequency response measurements are constantly taken during the random vibration tests. It was observed that the natural frequency peak shifts during failure, when the brass mass is ejected. This shift in natural frequency indicates a change in the sample's characteristics, with loosening of the brass mass in this case. Although this observation is not useful when the EDU is integrated and launched on a CubeSat, it led to terminating the random vibration test safely to prevent any damages to the test bed.

Figure 60 is sample 6's random vibration test data showing the $\frac{g^2}{Hz}$ spectrum vs. Hz. This sample successfully passed the z-axis random vibration testing as depicted by staying within the envelope. For completeness the subsequent random vibration test data for the samples is included in Appendix F.

THIS PAGE INTENTIONALLY LEFT BLANK

V. INTEGRATION

The TINYSCOPE project is planning to use a modified 3U Pumpkin CubeSat. For this thesis, the author chose to simulate integrating the SMAC release mechanism EDU into this structure. Figure 61 is picture of a 3U Pumpkin CubeSat with the solar panels in the deployed configuration.
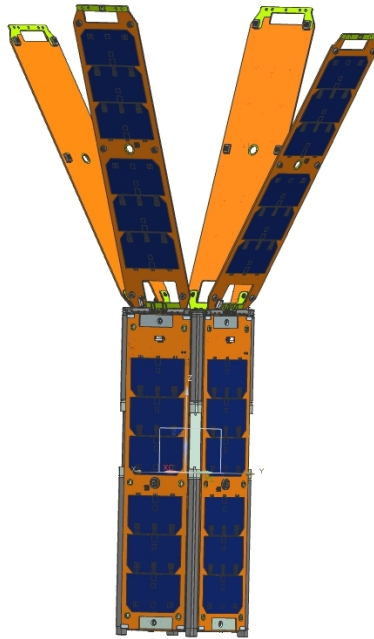
Figure 61.   Pumpkin 3U CubeSat in the Deployed Configuration. After [21]

A closer look at the springs on the solar panel can be seen in Figure 62.
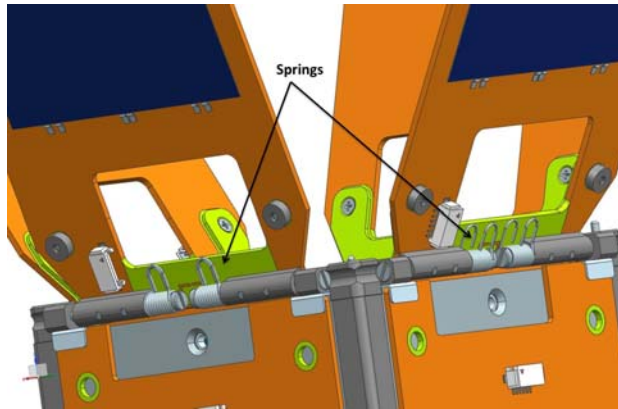
Figure 62.   View of Springs on Solar Panels. After [21]

The Pumpkin 3U CubeSat's solar panels are secured with a spring hinge on the top end, and with a rubber band on the bottom external part of the structure. When the CubeSat is placed inside the CubeSat launcher (NPSCuL), the rubber band is taken off and the solar panel is secured along the walls of the launcher in the stowed configuration (Figure 63). When the CubeSat deploys from the launcher, the solar panels drag along the walls of the launcher and immediately spring open to the deployed configuration (Figure 61) once free from the launcher. This type of deployment is commonly referred to as "dragging." As stated above, draggers are not allowed on more recent launches, creating a demand for more secure deployment solutions.
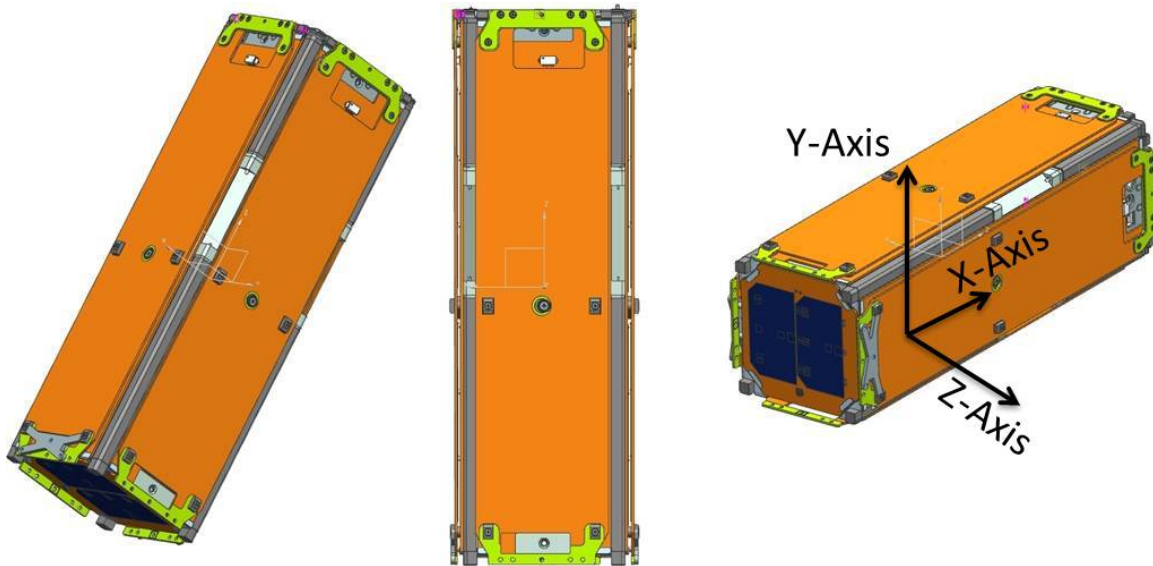
Figure 63.   Pumpkin 3U CubeSat in the Stowed Configuration. After [21]

A close up view of the 3U Pumpkin base is shown in Figure 64. In this figure, the bottom plate is shown and removed to illustrate the amount of space available to attach the EDU.
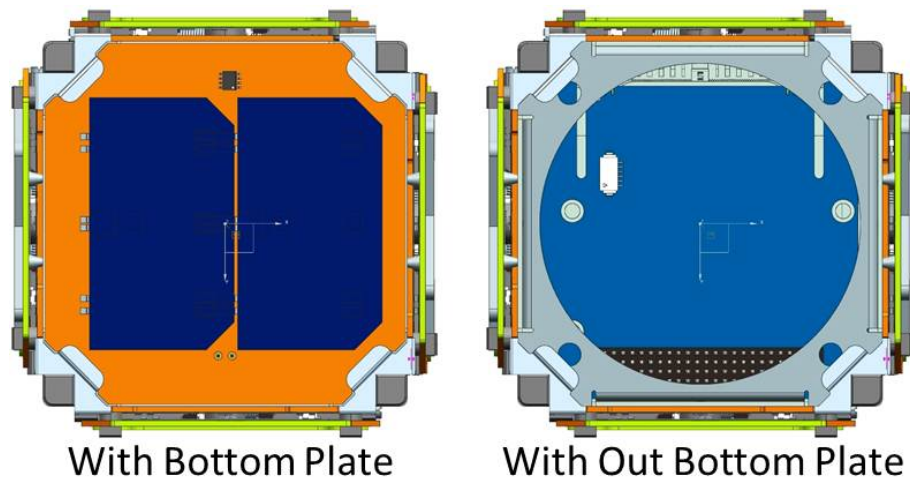
Figure 64.   Bottom View of CubeSat With and Without Bottom Plate Views. After [21]

The author takes advantage of existing holes to integrate the EDU. To attach the solar panel, mounting hardware (Figure 65) is created to line up with the retaining bolt on the EDU.

Figure 65.   Solar Panel Mounting Hardware

The mounting hardware has two cones that protrude into the Pumpkin structure, providing additional support in the X-axis and Y-axis. This was done to further restrict any small movements at the end of the solar panel, which is restricted on top by the hinge. This additional restriction allows the EDU to observe little acceleration in the X-axis and Y-axis during launch with the Z-axis carrying all the load, operating within the EDU vibrational load limits as tested above. The placement of the EDU with and without the mounting hardware can be seen in Figure 66. Without the mounting hardware, the EDU would not be able to secure the solar panel.
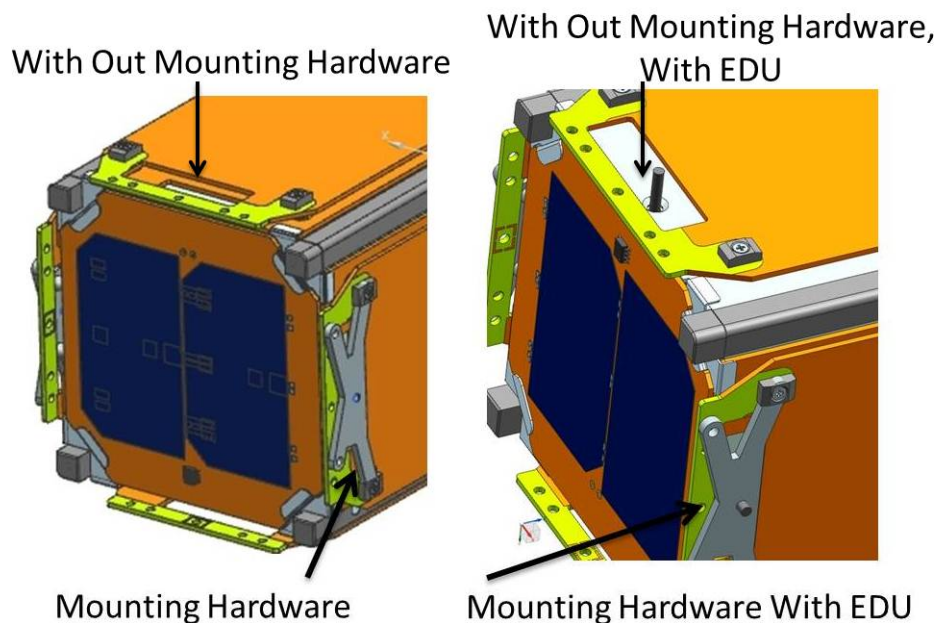
Figure 66.   Pumpkin Bottom View Without and With Mounting Hardware
and EDU. After [21]

Each solar panel has a corresponding EDU attached to it (Figure 67). Figure 67 is similar to Figure 64, but this time the EDU's are installed. Additionally, it can be seen in Figure 67 that the mounting hardware does not add to the overall outer dimensions of the 3U CubeSat structure, therefore ensuring no unwanted contact between NPSCuL and TINYSCOPE.

EDU With Bottom Plate   EDU With Out Bottom Plate
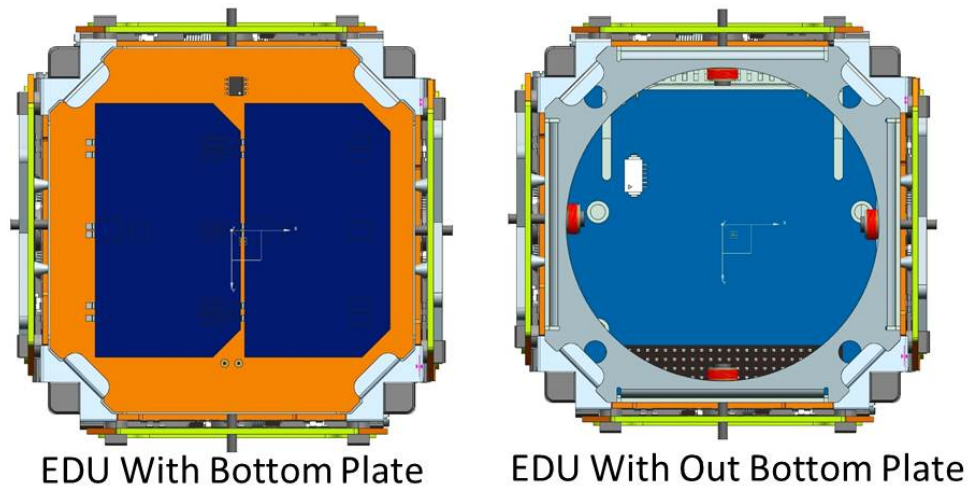
Figure 67.   Pumpkin CubeSat With EDU Bottom Views. After [21]

When activated, the retaining bolt and the NiTi ring release from the AL 7075-T6 bushing, allowing the solar panel to swing along its spring hinge to the final deployed configuration. The deployment sequence of the EDU incorporated in the Pumpkin 3U structure is shown in Figure 68 (without the bottom plate for illustration purposes). The first step is to pass current to the Nichrome wire. This in turn heats up the AL 7075-T6 bushing and NiTi ring. The NiTi ring shrinks and releases from the Al 7075-T6 bushing. The solar panel begins to deploy as the holding bolt and NiTi ring fully decouple from the AL 7075-T6 bushing. The solar panel hinge swings the solar panel to its final deployed configuration.
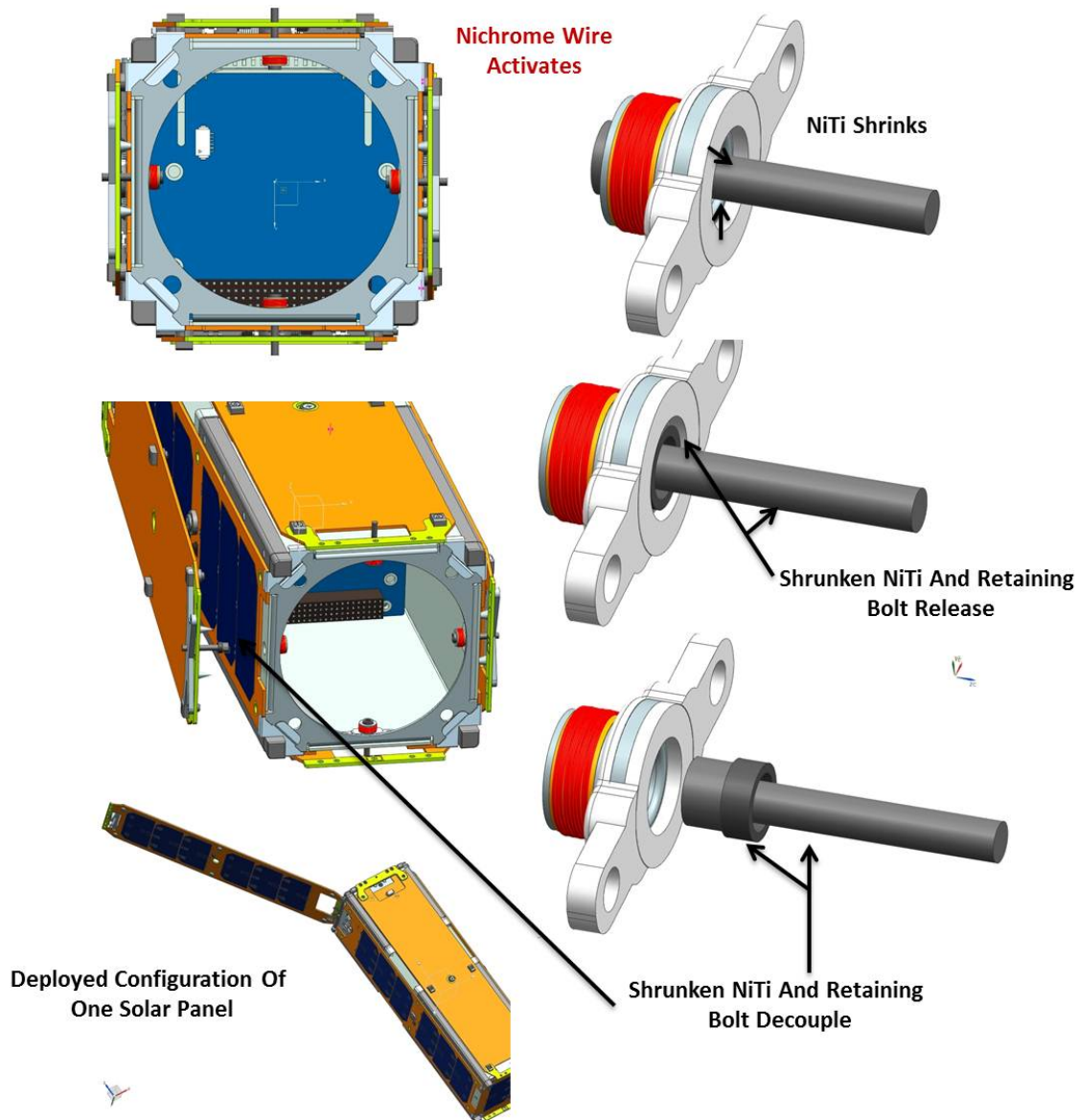
Figure 68.   Deployment Sequence of EDU on CubeSat. After [21]

TINYSCOPE uses a 12-cell battery pack providing 6.6 amp-hours or 95 watt-hours of capacity and supplying a 12 volt primary and 5 volt secondary electrical bus[4]. The EDU uses 3.5 volts, 0.73 amps (2.55 watt) of power to fully deploy the solar panel. Increasing the voltage (and therefore current) decreases the activation time if needed. The required power from the EDU to fully activate and deploy is well within TINYSCOPE's power capacity.

VI. CONCLUSION AND RECOMMENDATION

A. SMA COUPLING

Shape Memory Alloys (SMAs) are used in various industries. In dentistry, shape memory alloys are used in the wire for braces. The person's body heat activates the transformation from the detwinned martensite phase to its austenite phase causing the wire to shrink and straighten. Another application is in pipe coupling. Shape memory alloy tubes are created to have a cold austenite phase. Further cooling and stretching (now in the detwinned martensite phase) allows the coupling device to shrink and clamp down on the two pipe ends at room temperature (austenite phase) as shown in Figure 6. This transformation causes the SMA rings to have a "shrink wrap" effect when heated. This thesis takes the reverse approach to the pipe coupling by using SMA rings as an interference joint release mechanism.

Available mechanical methods to secure and deploy appendages (such as solar panels) on CubeSats are very limited. The limitations are primarily due to the size and power constrains imposed by the CubeSats form factor (as small as 1000 cm^3 structure). This thesis introduces the use of SMA (NiTi) in conjunction with an AL 7075-T6 bushing to create an interference joint. This securing mechanism releases in a non-mechanical and non-explosive manner, increasing the probability of success while eliminating residual shock from deployment.

1. Synopsis

When the ring is initially formed it is in the austenite phase. It is not until the ring is cooled and expanded (added stress) that it assumes the detwinned martensite phase. In the detwinned martensite phase the ring can perform mechanical work. When heat is applied, the ring shrinks back to its original size vice expanding as most commonly metals do. This characteristic makes the interference joint possible for a release mechanism. The shape memory alloy ring is press-fit into the AL 7075-T6 bushing in the detwinned martensite phase.

Once activated, the shape memory alloy ring shrinks to its austenite phase and is released from the AL 7075-T6 bushing.

The relationship between the material properties and interferences with respect to estimated holding force in the axial direction are listed in Equations 1.2–1.9. SMAs material properties (modulus of elasticity and Poisson's ratio) are different between detwinned martensite and austenite phases. The equations also assume a perfect circular ring and circular hub, both of which are hard to achieve. The non-perfect circular rings and hubs create "hot" and "cold" spots. "Hot spots" are places where there is increased interference between the two pieces, and "cold spots" are where there is no contact between the two pieces.

A solar panel with all the hardware (springs, hinges, screws) for a 3U CubeSat weighs 110 g +/- 5 g (0.24 lb +/-.011 lb). Estimating a worst case vibrational load due to launch conditions of 30 GRMS, this thesis estimates a required holding force of 135 N (30 lbf) in the axial direction. Using a 7.8 mm (0.307 in) length, 5.18 mm (0.204 in) outer diameter SMA ring in a case hardened steel bushing with interference of 0.127 mm (0.005 in), 2,600 N (590 lbs) of static holding force in the axial direction is achieved[4]. This greatly surpasses the minimum required holding force. To reduce the size and required power for activation, this thesis uses a SMA ring of 2 mm (0.079 in) length and 5.24 mm (0.207 in) outer diameter in a AL 7075-T6 bushing with interference of 0.127 mm (0.005 in). In so doing, 343 N (77 lbf) of static holding force in the axial direction is achieved.

Using Al 7075-T6 as the bushing material allows heat to pass to the NiTi ring with low resistance. The small NiTi ring and the AL 7075-T6 bushing (using Nichrome 31 gauge wire as the heating source) require 2.55 watts (3.5 volt, 0.75 amp) of power to activate in 85 seconds. Increasing the power to 4.7 watt (4.9 volts, 0.96 amps) decreases the activation time to 42 seconds. This variation allows for further customization between allotted power from the CubeSat to activate the device, and time of activation desired.

Random vibration testing in the axial (Z-Axis) direction was successful to 30 GRMS levels with samples using 0.12 mm (0.0047 in) and above interferences. Using a sine sweep test prior to conducting the random vibration test allows for predictions to be made regarding the coupling device's ability to withstand the 30 GRMS load.

2. Future Work

The NiTi ring geometry can be further studied to reach an optimum size to holding ratio. In this thesis, the size selected was able to statically hold the mass of a solar panel, and maintain security in the axial direction during vibration testing. A further margin of safety needs to be achieved by possible SMA length change or tighter interference. Care must be taken when changing the amount of interference. There is a limit due to buckling effects, and the possibility of returning the SMA to its austenite phase size with high interferences. With any geometry changes, total mass, size, and power required for activation must all be minimized to implement into a CubeSat successfully.

B. SMA DEVICE

1. Synopsis

The author was able to build upon the work conducted by CDR Will Crane. The EDU design now meets the size and power constraints imposed by CubeSats. The EDU was tested in a vacuum and at room temperature and randomly vibrated while restraining a solid brass mass. Further testing in a vacuum and additional vibration testing using a CubeSat structure and solar panel is needed to qualify the EDU as a fully certified flight unit.

2. Future Work

The random vibration testing validated the assumption that the EDU was designed to withstand Z-axis loads during launch conditions, but is unable to withstand high loads in the X and Y-axis. The addition of the specially-designed

mounting hardware will eliminate the X and Y-axis loads from the EDU. Testing using the mounting hardware is needed to further validate this claim.

Finally, thermal vacuum testing below room temperature needs to be conducted to validate the EDU's performance in the full range of launch and orbit thermal environments.

APPENDIX A.   PRESS-FIT PROCEDURES

1) Prior to press-fitting, clean both NiTi ring and AL 7075-T6 bushing using isopropyl alcohol. This will remove any residual oils left over from the manufacturing process.

2) Place the load cell in a plastic bag. This will protect the load cell during press-fitting and from the use of isopropyl alcohol as a lubricant. Place the adapter cradle on top of the load cell.
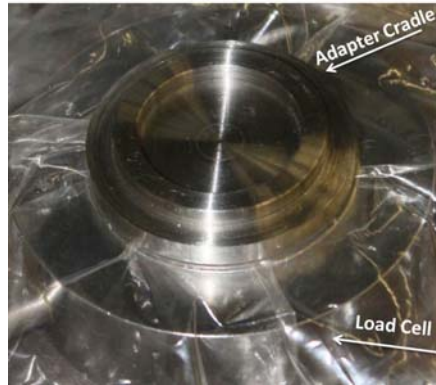
3) Place the load cell with the adapter cradle on the base of the press.

4) Place the AL 7075-T6 bushing on the adapter cradle. Press-fitting in the bottom-up orientation is shown below.

5) Place the bottom cradle on top of the AL 7075-T6 bushing.

6) Slide the press pin through the opening of the top cradle. Place the NiTi ring on the press pin.

7) Fill the AL 7075-T6 bushing with isopropyl alcohol, and place the assembly pictured above on top of the bottom cradle. Ensure that the NiTi ring is centered on the AL 7075-T6 bushing.

8) Using a python script to record the amount of force on the load cell, engage the press to push the press pin down. This will cause the NiTi ring to be press-fitted into the AL 7075-T6 bushing.

APPENDIX B   ASSEMBLY
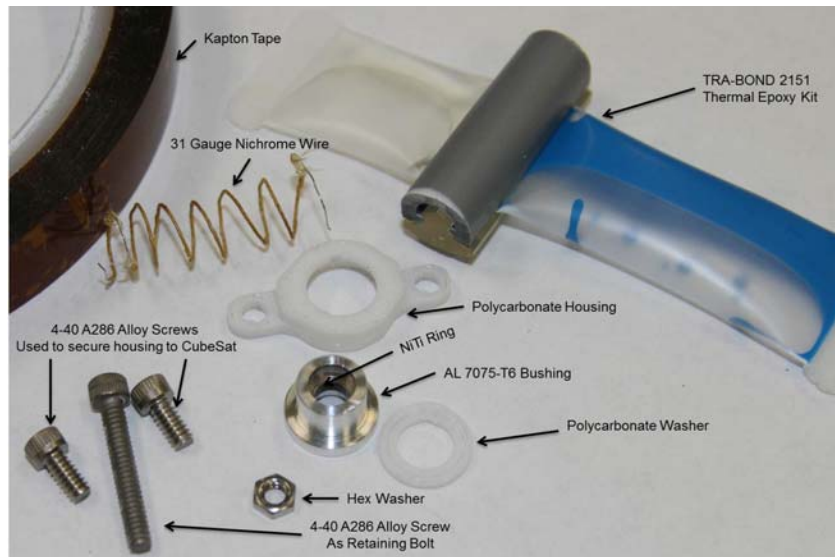
1) To assemble the EDU, the NiTi ring must already be press-fitted into the AL 7075-T6 bushing. Those pieces, already joined, are pictured in the figure above.

2) Place the Polycarbonate housing on top of the AL 7075-T6 bushing.

3) Wrap the 31 gauge Nichrome wire around the AL 7075-T6 bushing. Wrap one layer of Kapton tape around the Nichrome wire to prevent any unwinding.
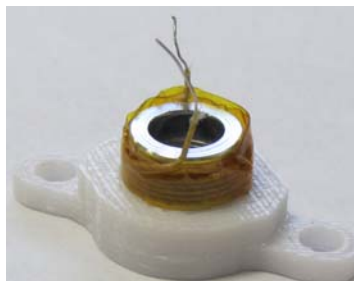
4) Place a small amount of TRA-BOND 2151 thermal epoxy on the upper portion of the Kapton tape. This will further secure the Nichrome wire and prevent the Kapton tape from unwinding during extreme conditions (such as strong vibrations)
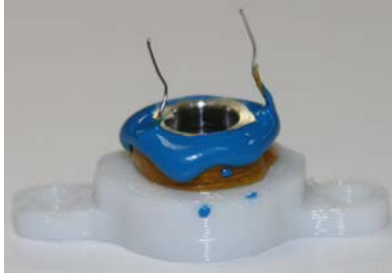
5) Slide the 4–40 A286 Alloy screw (retaining bolt) from the top of the assembly.

6) Screw the hex washer onto the retaining bolt. This serves to prevent the retaining bolt from sliding out (especially once installed inside the CubeSat).

7) Place the polycarbonate washer on the AL 7075-T6 bushing. This completes the assembly.

APPENDIX C. SEPARATION PROCEDURES

1) Take the press-fitted sample and place it in the middle holder.

2) Flip the middle holder (with the sample) and place it on top of the top holder. Secure the middle holder on the top holder with the fastening screws.

3) Slide the retaining screw through the bottom opening of the top holder, and up through the sample.

4) Place the top holder in the upper mounting of the tensile machine and secure it with a pin.

5) Place the bottom holder in the lower mounting. Secure it in place with a pin. Rotate the retaining bolt by hand into the bottom holder, eliminating any slack between the bottom holder and the top of the NiTi ring.

6) Begin extraction at a rate of 1mm per second.
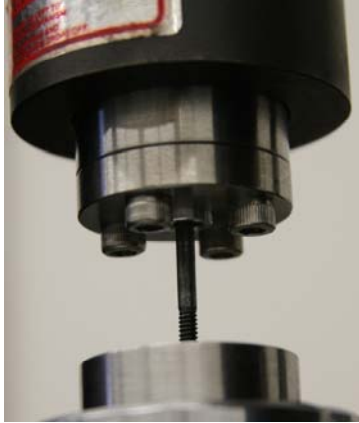
7) A depiction of the NiTi ring being extracted from the AL 7075-T6 bushing is shown below.

8) Continue extracting until NiTi is fully released from the AL 7075-T6 bushing. All data is recorded using the tensile machine supplied software.

APPENDIX D.   THERMAL RELEASE PROCEDURES
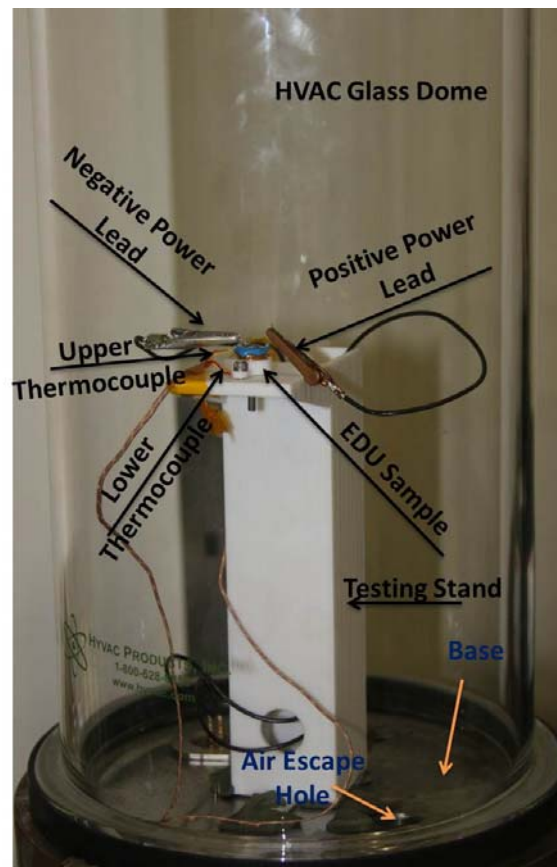
1) With the EDU sample fully assembled, place the polycarbonate washer on the testing stand. Place the lower thermocouple on top of the polycarbonate washer.
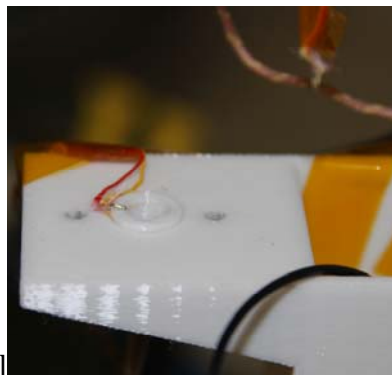
2) Place the EDU sample on top of the thermocouple and PC washer. Secure the EDU onto the testing stand with 4–40 screws. Using an ohm

meter, measure the resistance of the Nichrome wire prior to attaching any power leads. Measure the entire path between the power source with the power leads connected to the Nichrome wire. Record the data for both measurements.

3) Place the upper thermocouple lead between the AL 7075-T6 bushing and the Nichrome wire on top of the EDU. Not all samples used the final TRA-BOND thermal epoxy. This allowed for said measurement. Those samples with the TRA-BOND epoxy (seen in figure below) do not have the upper thermocouple attached on the Nichrome wire, but have it placed on the inside of the AL 7075-T6 bushing.
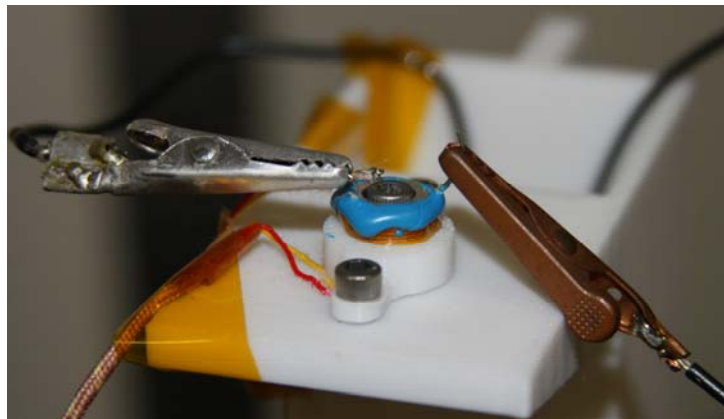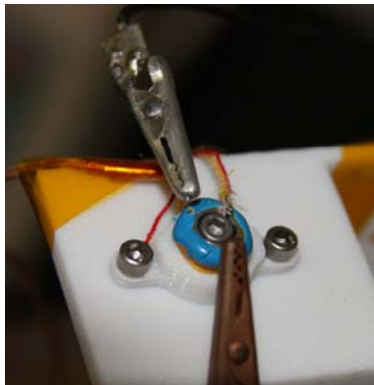
4) The HVAC glass dome is placed over the testing stand. A vacuum is created inside the dome by removing the air with a pump via the holes on the bottom of the base.
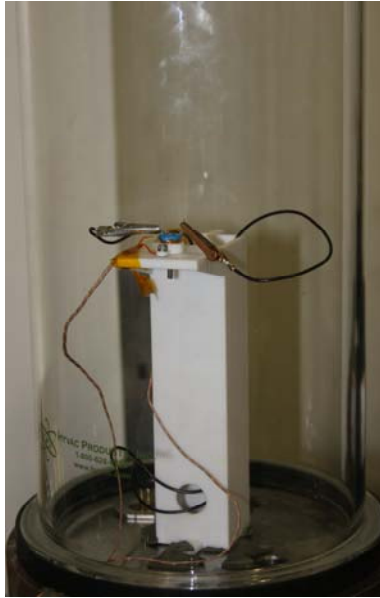
5) Power supply (Laboratory DC Power Supply Gwinstek GPS-4303) is set to provide a maximum of 3.5 volts and 0.75 amps. With the onset of power to the EDU, time and temperature are recorded using the OMEGA HH147U Data Logger Thermometer.

6) Once the NiTi ring and retaining bolt are released from the AL 7075-T6 bushing, power is secured and timer is stopped. The vacuum seal is broken and air is allowed to return back into the glass dome.

THIS PAGE INTENTIONALLY LEFT BLANK

APPENDIX E.   VIBRATION TESTING PROCEDURES
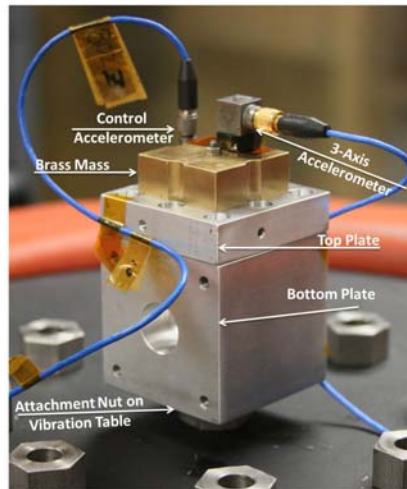
1) Secure the bottom plate to the vibration table via a screw from the hole in the top center of the block. (For illustration purposes, the following steps are pictured on an ordinary table vice the vibration table.)

2) Secure the sample EDU to the inside of the top plate via small screws.

3) Screw the threaded brass mass to the top of the top plate via the holding bolt. A hex washer is used to better secure the brass mass, preventing the screw from walking out during vibration testing.

4) For Z-Axis testing, secure (via four screws) the top plate with the EDU and brass mass on top of the bottom plate.

5) For Y-Axis testing, secure (via four screws) the top plate with the EDU and brass mass on the side of the bottom plate.

6) Attach the 3-Axis accelerometer to the brass mass, and the single axis (control) accelerometer to the top plate.
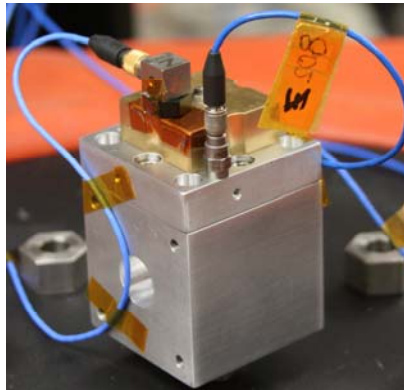
7) Connect the leads to the accelerometers. Conduct a full forward and backward sine sweep (20Hz to 2,000Hz)

8) Conduct random vibration test.

9) Conduct a post sine sweep.

10) Steps 7–9 are repeated for Y-Axis testing
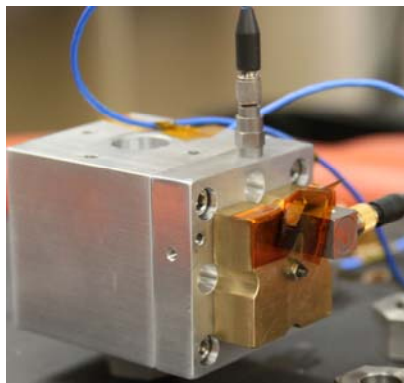
THIS PAGE INTENTIONALLY LEFT BLANK

APPENDIX F.   ADDITIONAL DATA

Sine

[g]

W:\Thesis\Sine\Sample # 1_Z_
Sine_Post-Random.rsn
  002: [08-29-12 14:29]
    04: Measurement, On Mass
    , (+Z) - Test Axis [g]
    ■ Meas. Signal
      Comments:
      ■ 5th device - testing in Z
        Random
  003: [08-29-12 14:31]
    04: Measurement, On Mass
    , (+Z) - Test Axis [g]
    ■ Meas. Signal
      Comments:
      ■ 5th device - testing in Z
        Random
W:\Thesis\Sine\Sample # 1_Z_
Sine_Pre-Random.rsn
  002: [08-29-12 14:16]
    04: Measurement, On Mass
    , (+Z) - Test Axis [g]
    ■ Meas. Signal
      Comments:
      ■ 5th device - testing in Z
  003: [08-29-12 14:17]
    04: Measurement, On Mass
    , (+Z) - Test Axis [g]
    ■ Meas. Signal
      Comments:
      ■ 5th device - testing in Z

[Hz]

W:\Thesis\New folder\VibMultiPlot all sine.gpd

Sample 1 Pre and Post sine plot in the Z-Axis

110

Sample 1 Z-Axis random vibration testing to 0 dB

111

Random **Measurement, On Mass, (+Y) - Test Axis**
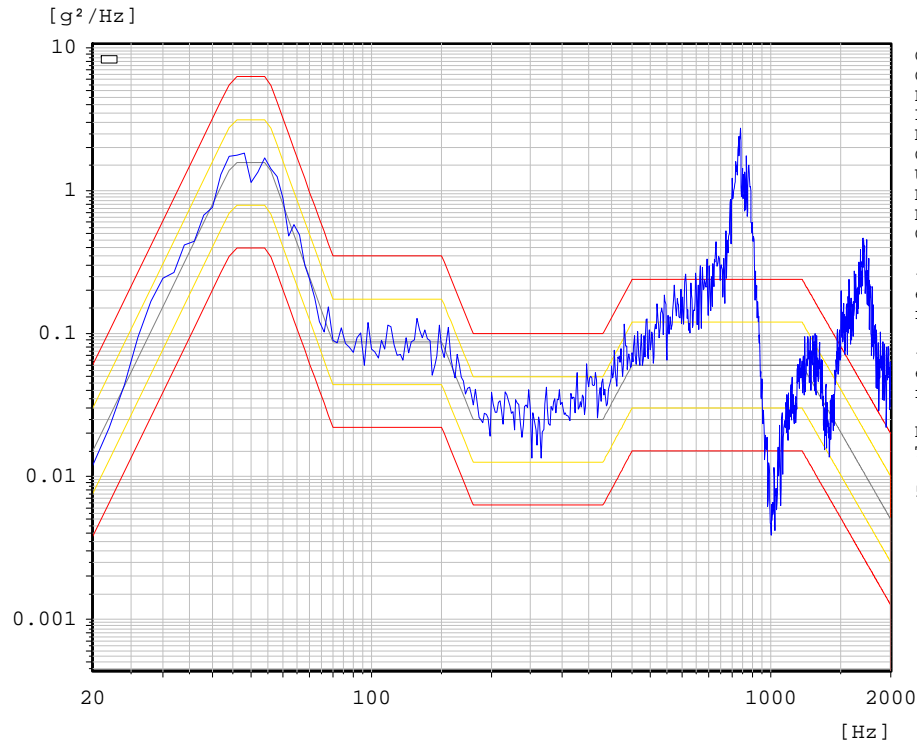
[g²/Hz]

Chan.no: 3
Chan.type: M
DOF: 30
Level: -9.0 dB
Resolution: 2 Hz
Contr.strat.: Maximum
Unit: g²/Hz
RMS (act.): 19.07 g
RMS (req.): 10.74
Contr.strat.: Closed loop

-- Time on act. level --
elapsed: 000:00:17
remaining: 000:00:12
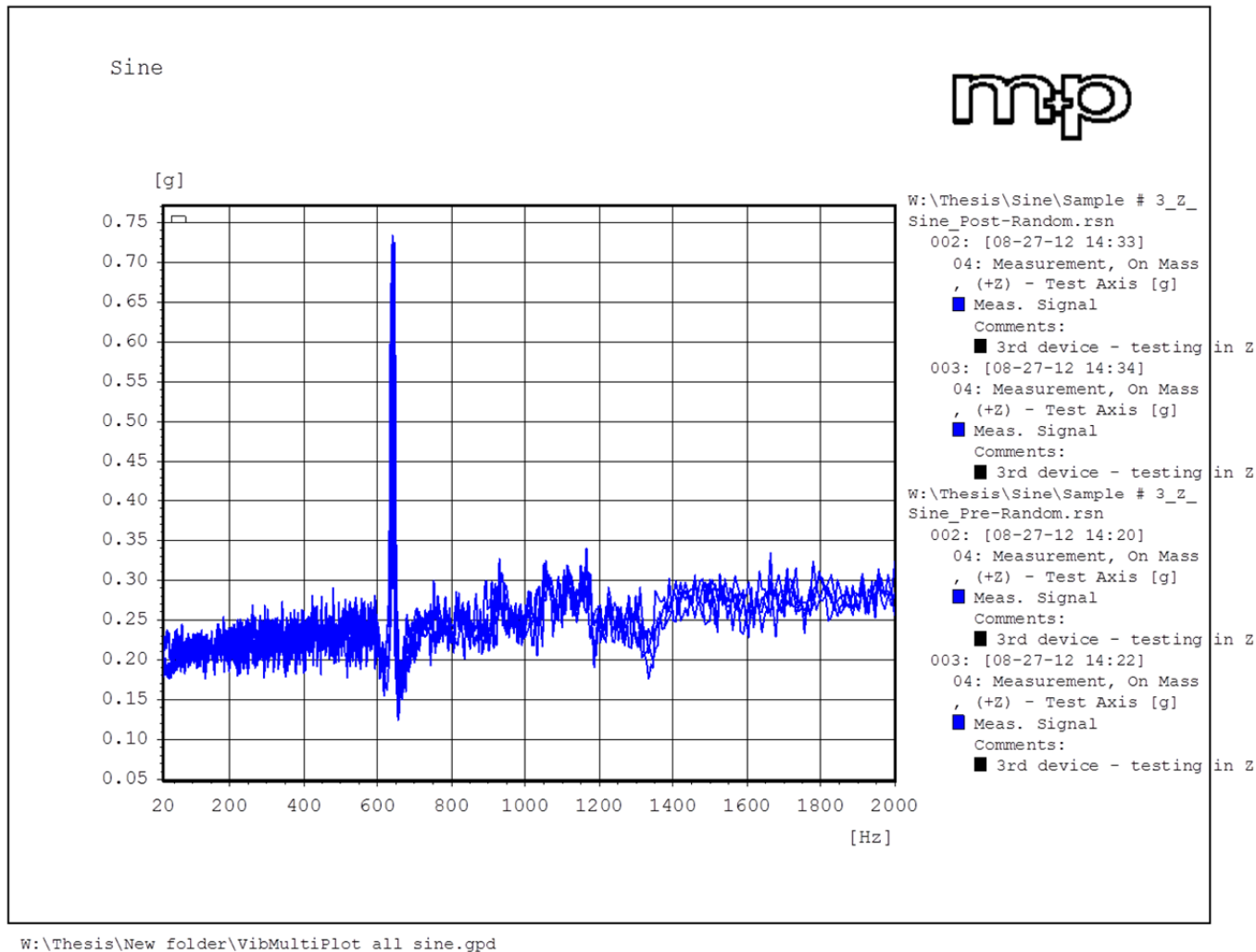
-- Time total --
elapsed: 000:01:17
remaining: 000:02:12

Date: 08-30-12
Time: 09:19:19

5th Component - Random in Y

[Hz]

W:\Thesis\Random\Sample # 1_Y_Random_0dB.rrn

Sample 1 Y-Axis random vibration to -9 dB

112

Sample 2 Z-Axis random vibration testing to -3 dB

113

Sample 3 Pre and Post sine plot in the Z-Axis

Sample 3 Z-Axis random vibration testing to 0 dB

115

Sample 3 Pre and Post sine plot in the Y-Axis
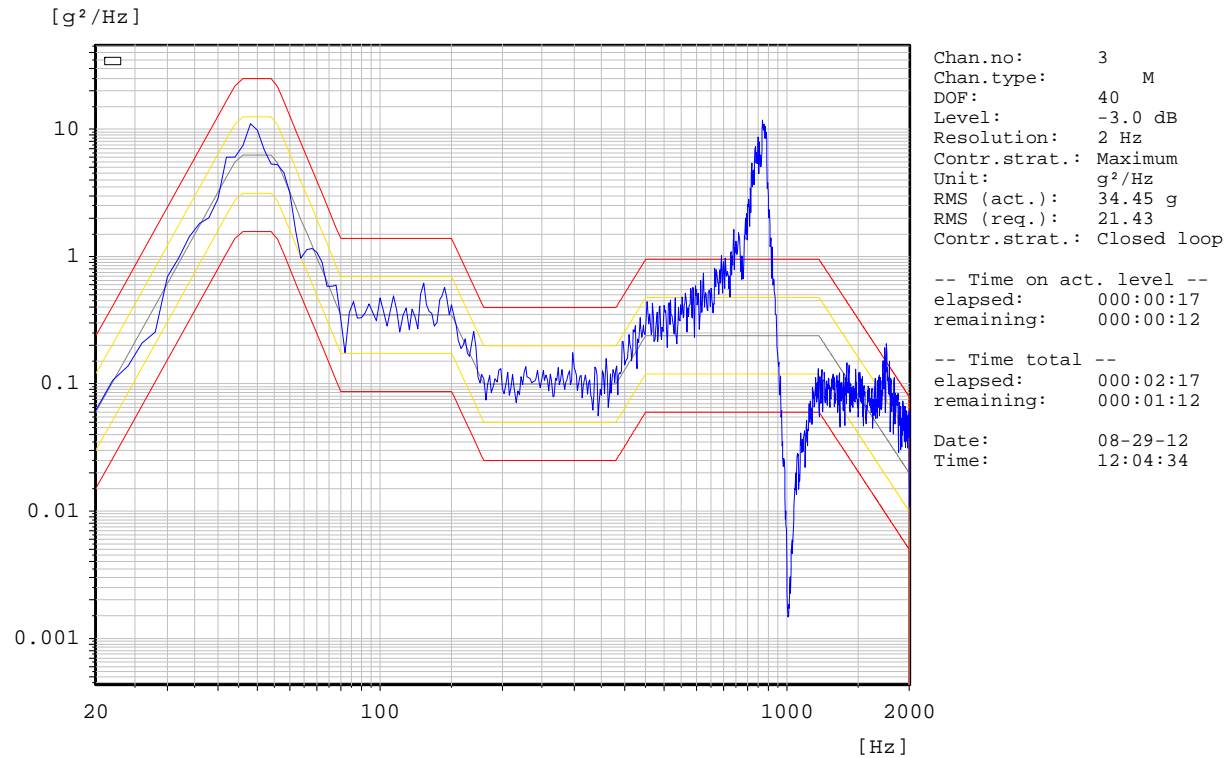
116

Random **Measurement, On Mass, (+Y) – Test Axis**
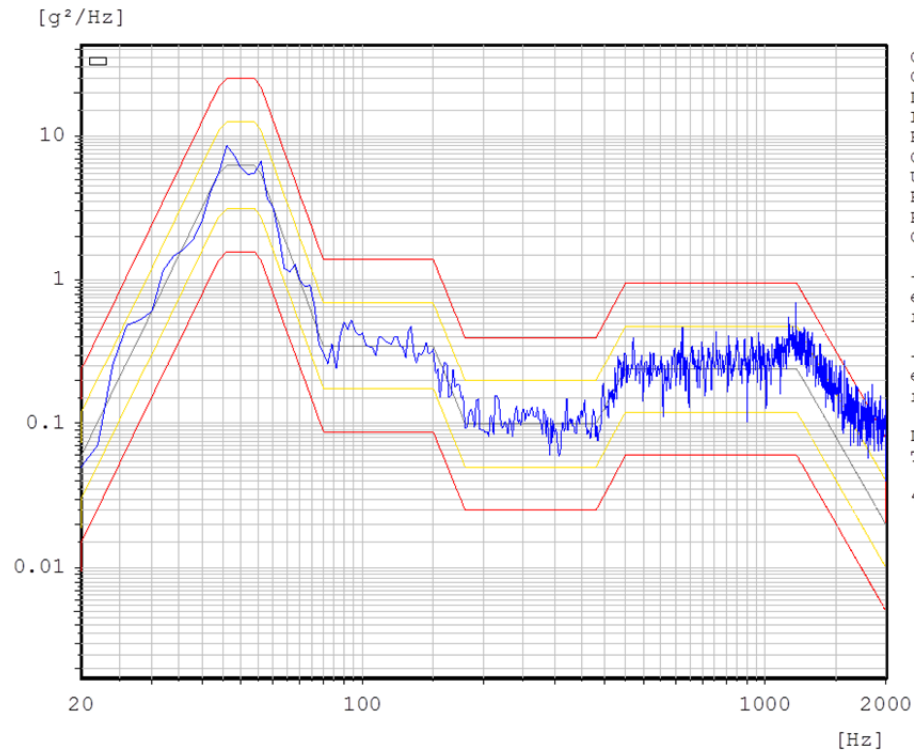
[g²/Hz]

Chan.no:	3
Chan.type:	M
DOF:	40
Level:	-3.0 dB
Resolution:	2 Hz
Contr.strat.:	Maximum
Unit:	g²/Hz
RMS (act.):	34.45 g
RMS (req.):	21.43
Contr.strat.:	Closed loop

-- Time on act. level --
elapsed: 000:00:17
remaining: 000:00:12

-- Time total --
elapsed: 000:02:17
remaining: 000:01:12

Date: 08-29-12
Time: 12:04:34

[Hz]

W:\Thesis\Random\Sample # 3_Y_Random_0dB.rrn

Sample 3 Y-Axis random vibration testing to -3 dB

117
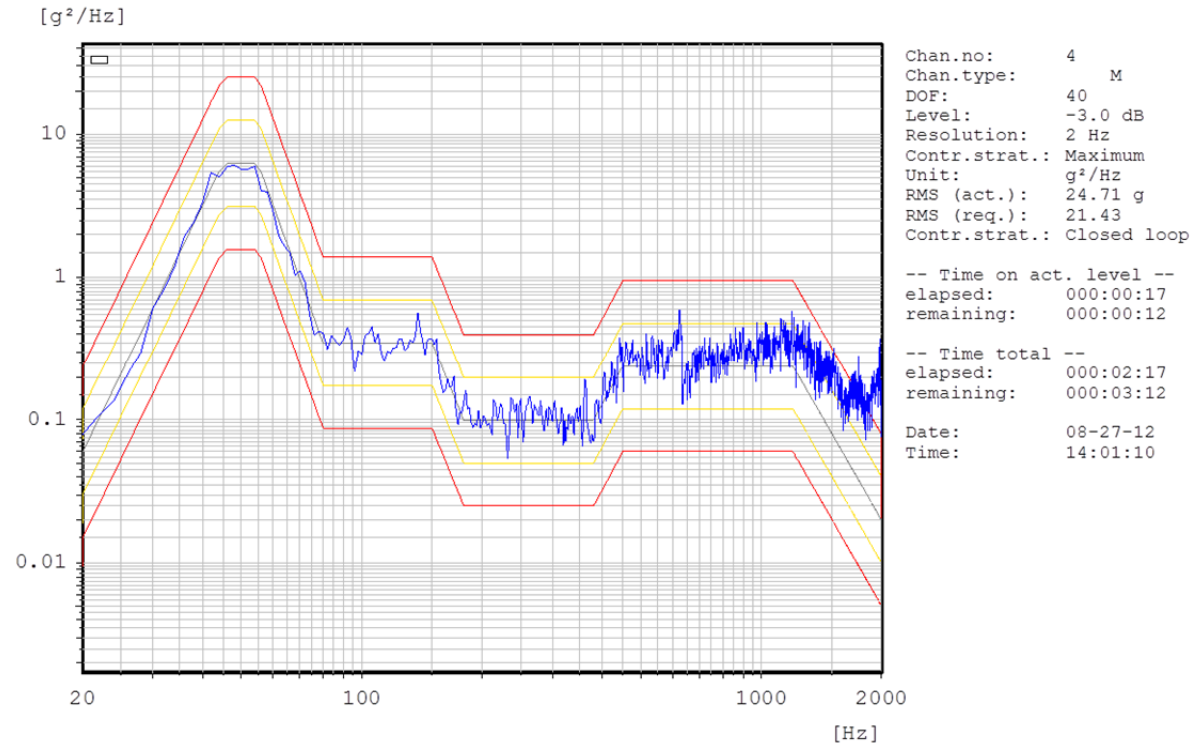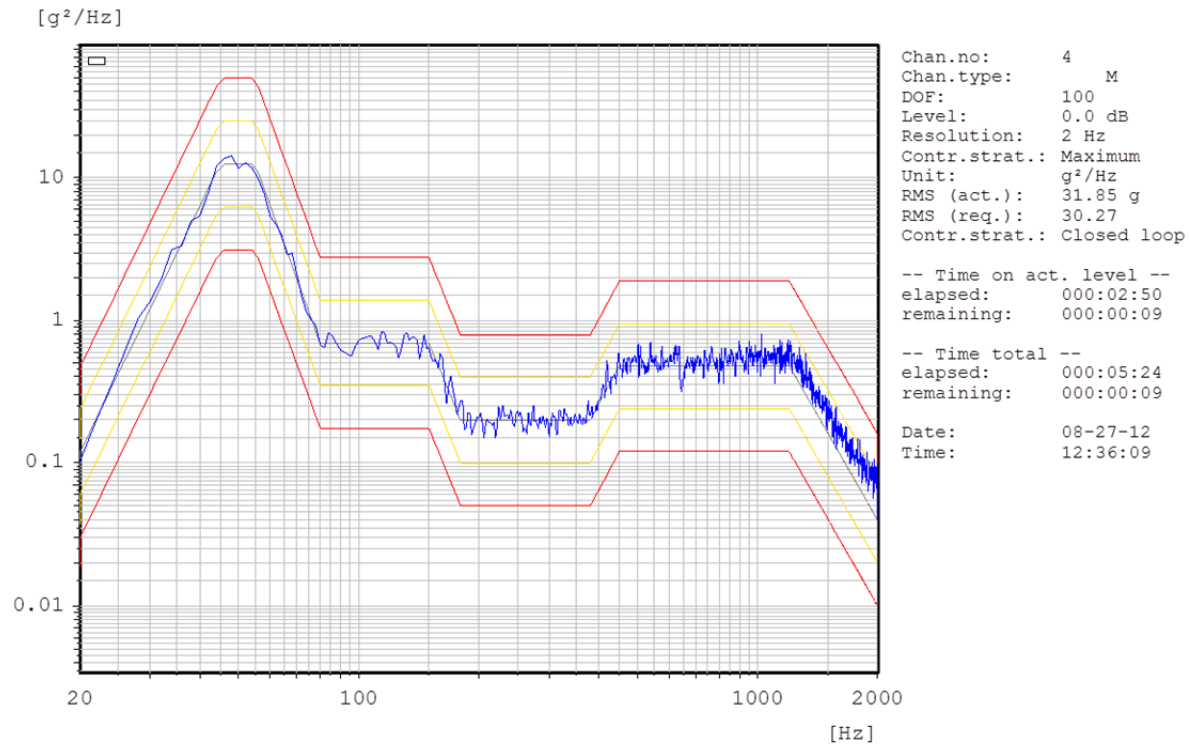
Sample 4 Z-Axis random vibration testing to -3 dB

118
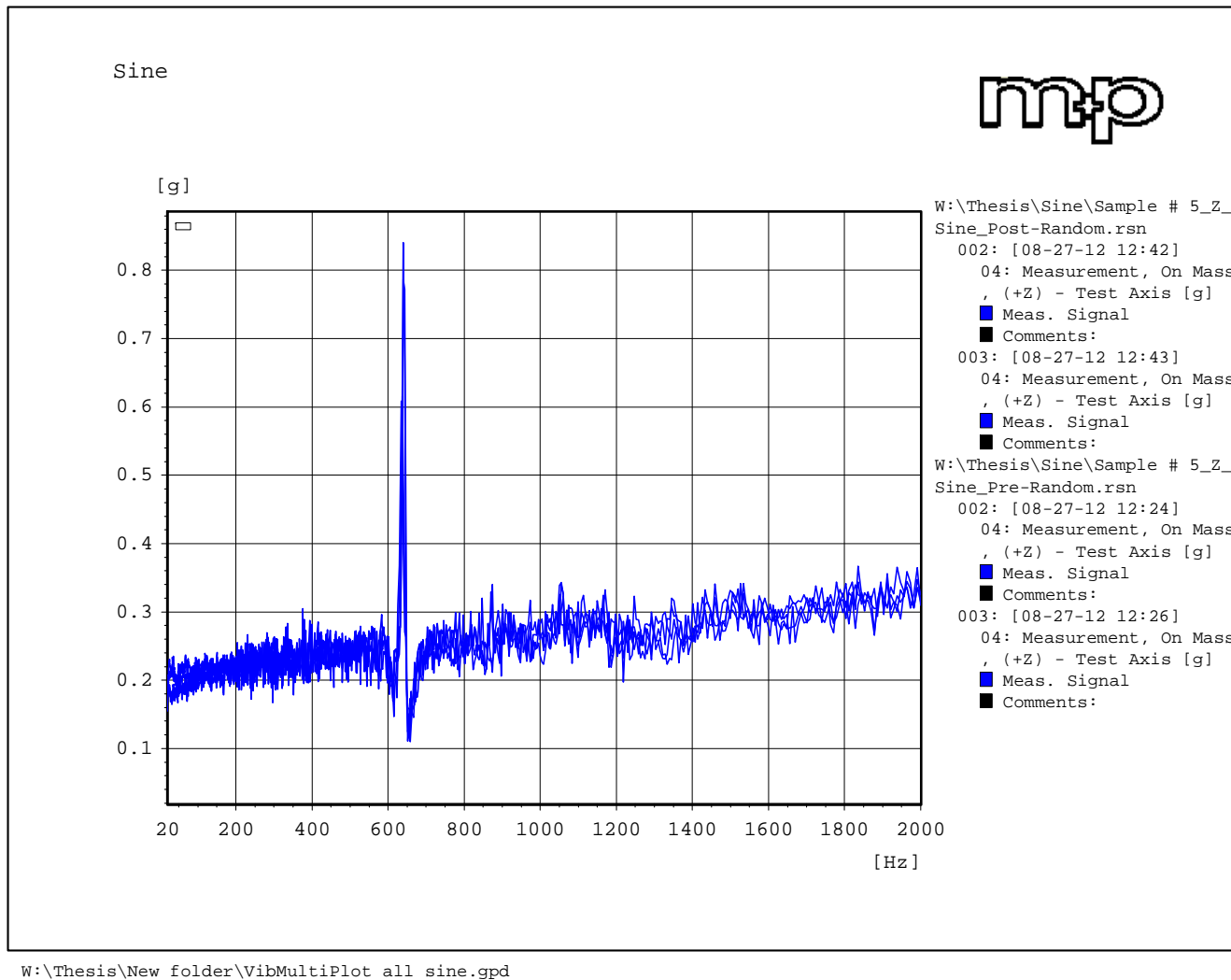
Sample 5 Pre and Post sine plot in the Z-Axis

Random   Measurement, On Mass, (+Z) - Test Axis

[g²/Hz]

Chan.no:	4
Chan.type:	M
DOF:	100
Level:	0.0 dB
Resolution:	2 Hz
Contr.strat.:	Maximum
Unit:	g²/Hz
RMS (act.):	31.85 g
RMS (req.):	30.27
Contr.strat.:	Closed loop

-- Time on act. level --
elapsed: 000:02:50
remaining: 000:00:09

-- Time total --
elapsed: 000:05:24
remaining: 000:00:09

Date: 08-27-12
Time: 12:36:09

W:\Thesis\Random\Sample # 5_Z_Random.rrn

Sample 5 Z-Axis random vibration testing to 0 dB
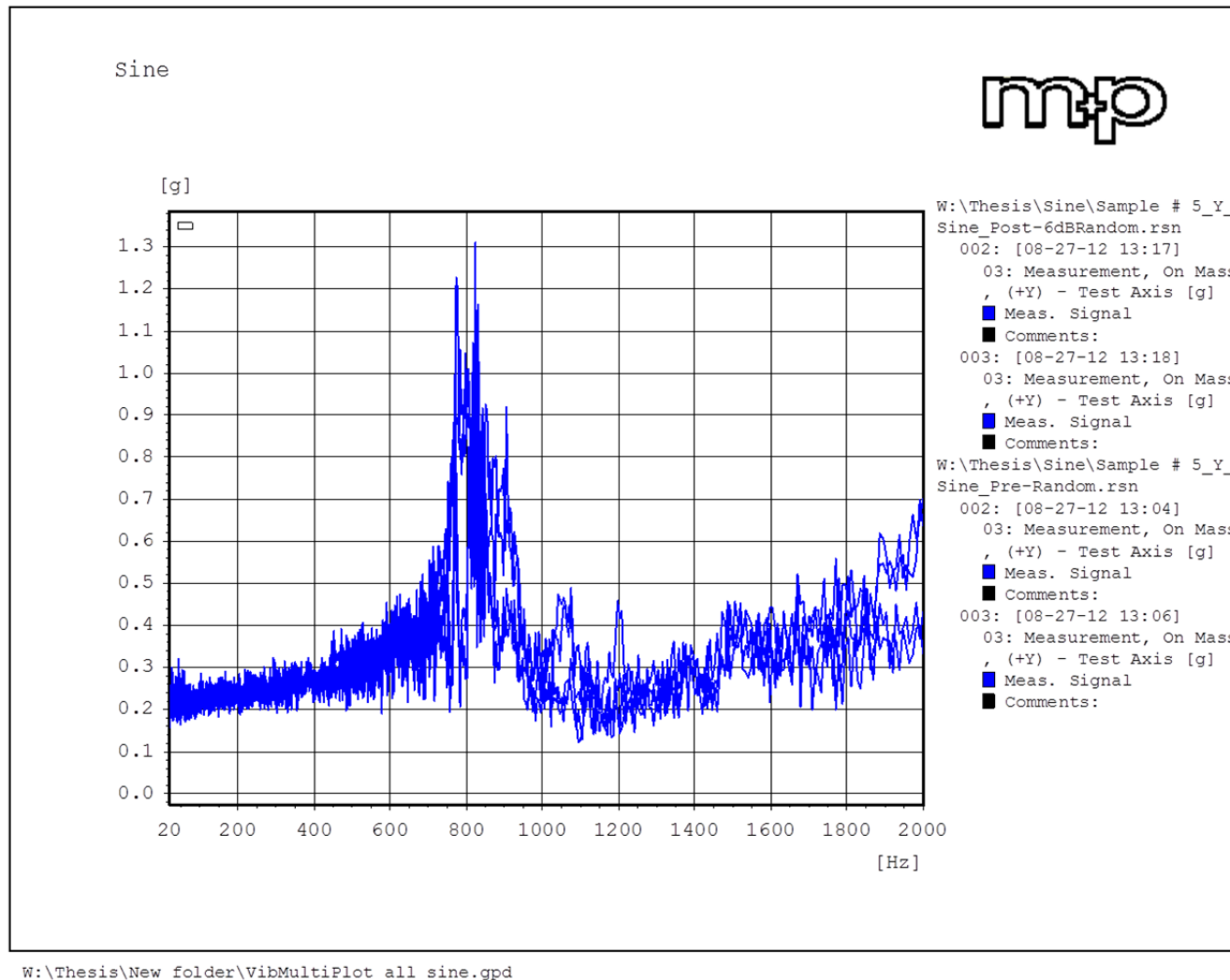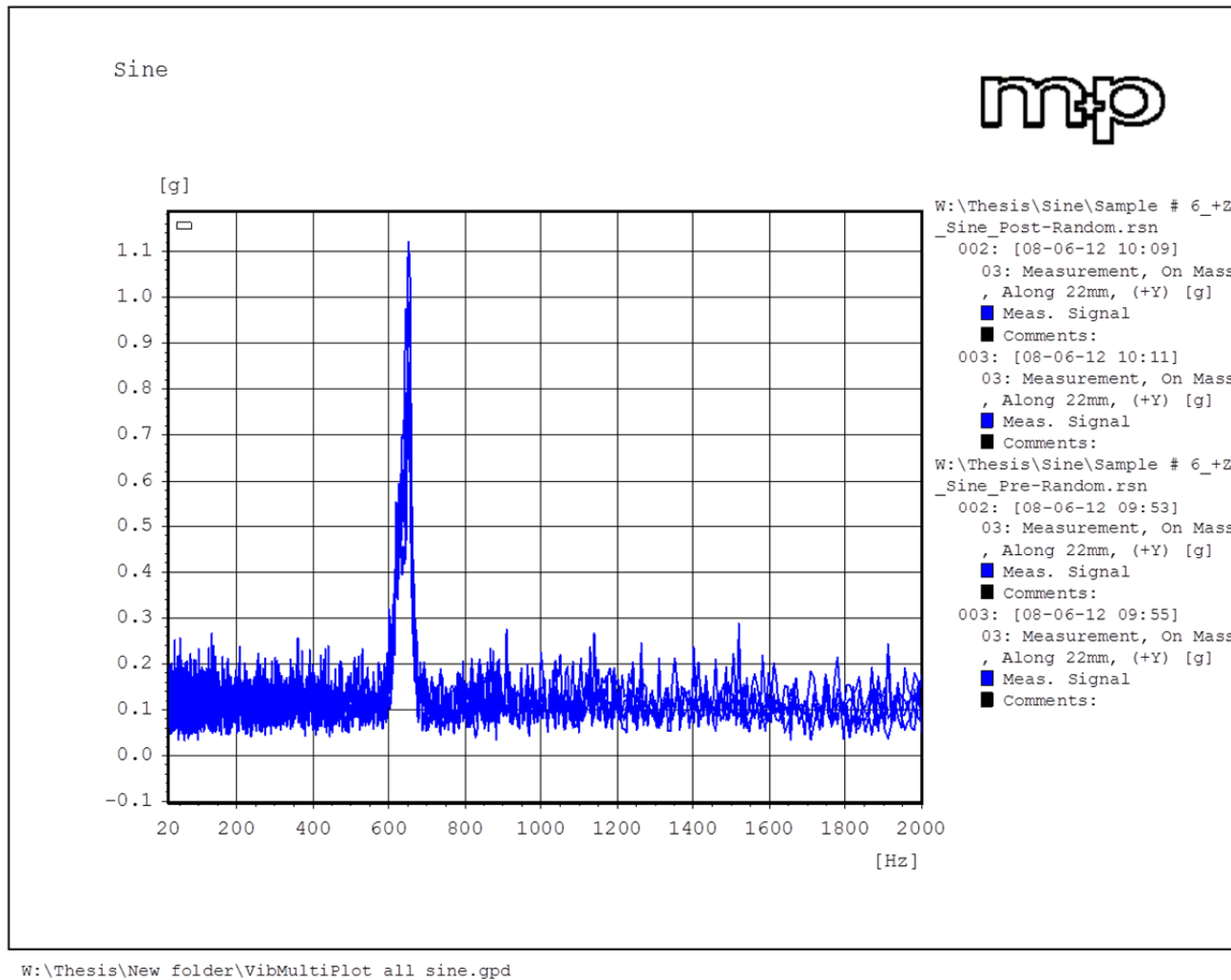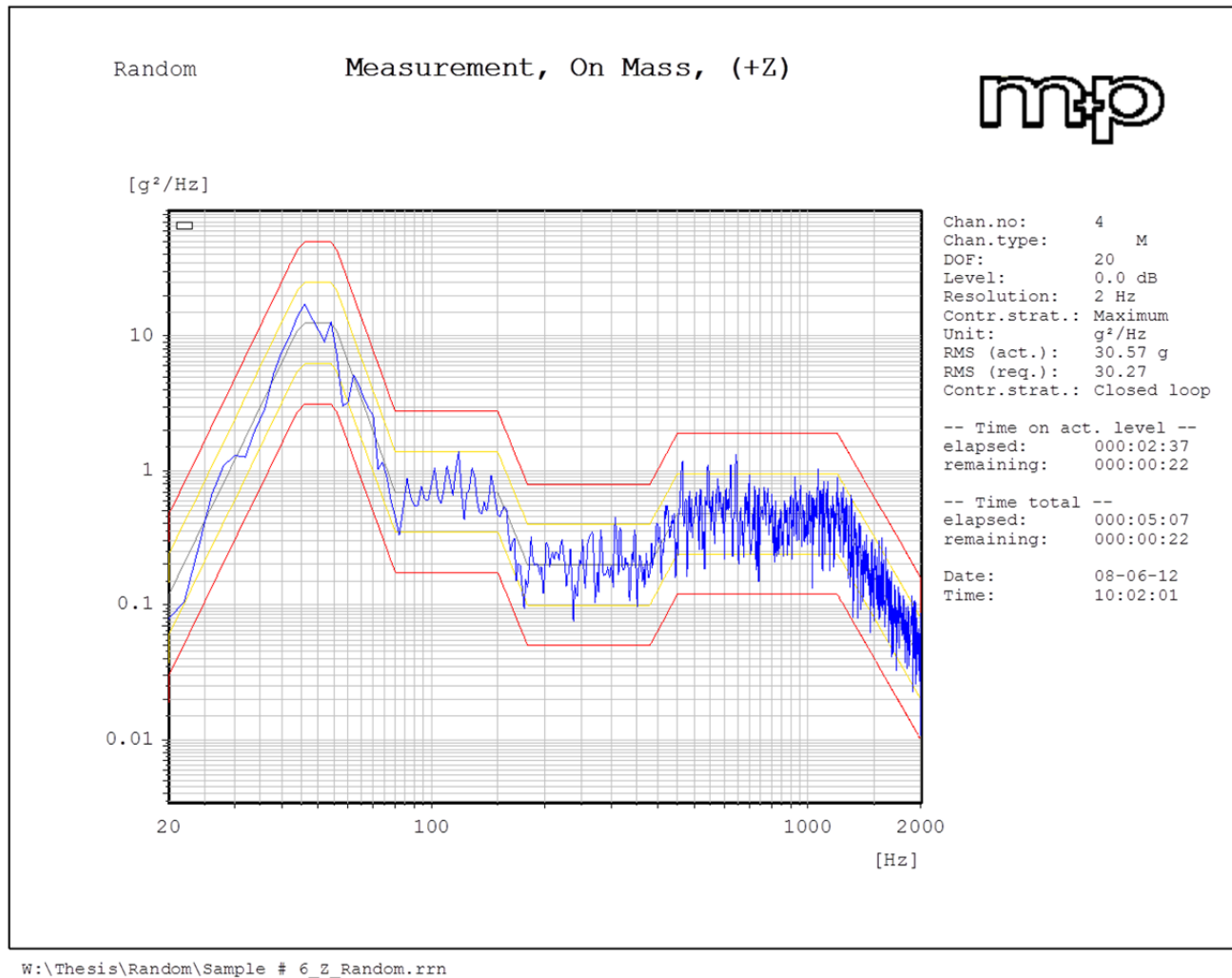
120

Sample 5 Pre and Post sine plot in the Y-Axis

Sample 5 Y-Axis random vibration testing to -6 dB

Sample 6 Pre and Post sine plot in the Z-Axis

Sample 6 Z-Axis random vibration testing to 0 dB
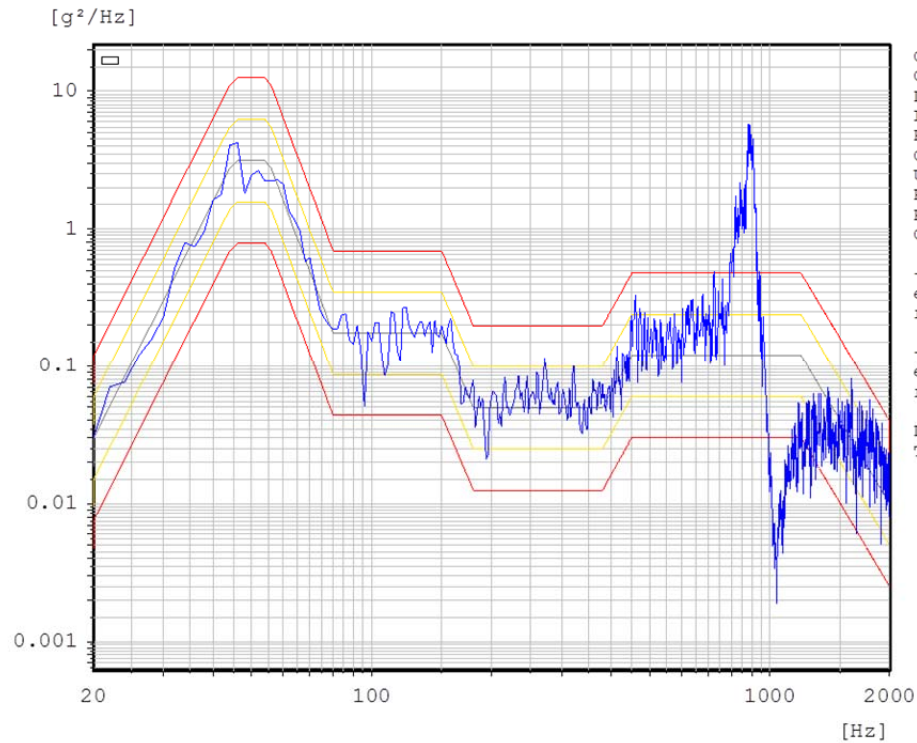
Sample 6 Y-Axis random vibration testing to -6 dB

VII. LIST OF REFERENCES

[1]   D. C. Lagoudas, Ed., *Shape Memory Alloys Modeling and Engineering Applications*. New Your, NY: Springer Science + Business Media, LLC 2008.

[2]   T. W. Duerig*, Engineering Aspects of Shape Memory Alloys.* Oxford, United Kingdom:Butterworth-Heinemann, 1990.

[3]   H. P. Bloch*, Improving Machinery Reliability*, Houston: TX: Gulf Publishing Company, 1998.

[4]   W. M. Crane, "Development of a nano-satellite micro-coupling mechanism with characteristics of a shape memory alloy interference joint," M.S. thesis, Dept. Mechanical and Aersopace Engineering.,Naval Postgraduate School, Monterey, CA, 2010.

[5]   K. Bramble. (2012, August 12). *Press fit engineering design equations and calculator* [Online]. Available: http://www.engineersedge.com/calculators/machine-design/press-fit/press-fit-equations.htm.

[6]   Intrinsic Devices Inc. (2012 February 7). *Material Properties Product Document* [Online]. Available: http://www.intrinsicdevices.com.

[7]   S. Chatterjee and G. P. Carman, "High friction interface with pseudoelastic NiTi," *Journal of Applied Physics Letters*, no. 91, 024104, 2007.

[8]   A. Thurn, S. Huyen, S. Koss, P. Oppenheimer, S. Butcher, J. Schlater, and P. Hagan, "A Nichrome burn wire release mechanism for CubeSats," *41st Aerospace Mechanisms Symp.*, Pasadena., CA, 2012, pp. 479.

[9]   TiNi Aerospace. (2012). *Frequently Asked Questions* [Online]. Available FTP: http://www.tiniaerospace.com/faqpp.html.

[10]   TiNi Aerospace. (2012). *Pinpuller P5* [Online]. Available FTP: http://www.tiniaerospace.com/pp5.html.

[11]   New Scale Technologies. (2012). *Squiggle SQ-100 Series Motors* [Online]. Available FTP: http://www.newscaletech.com/doc_downloads/SQ-100-V.pdf.

[12]   A. Reif. (2012, August 22). *Mass for 3U solar panel* [Online].
        Available e-mail: ADAM@PUMPKININC.COM Message: Get mass
        for 3U solar panel.

[13]   ASM Aerospace Specification Metals, Inc. (2012, February 20).
        Metal Distributor [Online]. Available:
        http://www.aerospacemetals.com/contact-aerospace-metals.html.

[14]   Tayco Engineering (2012). *Flexible Heaters* [Online]. Available
        FTP: http://www.taycoeng.com/proa.htm.

[15]   Pelican Wire Company Inc. (2012). *Wire Catalog* [Online]. Avaliable
        FTP: http://www.pelicanwire.com/resistance-wire-alloys/Nichrome-
        80/.

[16]   Hotwire Foam Cutter. (2012). *Nichrome technical data* [Online].
        Available FTP:
        http://hotwirefoamcutterinfo.com/Hot_Wire_Foam_Cutter_Info/_Nic
        hromeData.html.

[17]   Fortus 3D Production System. (2012). *PC (polycarbonate)* [Online].
        Available FTP:
        http://www.fortus.com/products/~/media/Fortus/Files/PDFs/MS-PC-
        FORTUS.ashx.

[18]   V. Kaushish. (2012) *NPSCuL photos* [Online]. Available e-mail:
        VKAUSHIS@NPS.EDU Message: Get NPSCuL photos.

[19]   V. Kaushish. (2012) *L39 Environments CubeSats* Kickoff [Online].
        Available e-mail: VKAUSHIS@NPS.EDU Message: Get NPSCuL
        vibration test parameters.

[20]   *Test Requirements for Launch, Upper-Stage, and Space Vehicles*,
        vol. I. Department of Defense., 1999.

[21]   PUMPKIN, Inc. (2012). *CAD models* [Online]. Available e-mail:
        ADAM@PUMPKIN.COM Message: Get CAD model.

INITIAL DISTRIBUTION LIST

1. Defense Technical Information Center
   Ft. Belvoir, Virginia

2. Dudley Knox Library
   Naval Postgraduate School
   Monterey, California

3. Professor Marcello Romano
   Naval Postgraduate School
   Monterey, California

4. Professor James Newman
   Naval Postgraduate School
   Monterey, California